Characterization of the Low- and High-Velocity Impact Performances of Fiber Reinforced Composites with Epoxy and Elium© Based Matrices

By

Jesse R. J. G. Llanos

Submitted in partial fulfillment of the requirements
For the degree of Master of Applied Science

At
Dalhousie University
Halifax, Nova Scotia
August 2023

Dalhousie University is located in Mi'kma'ki, the
ancestral and unceded territory of the Mi'kmaq.
We are all Treaty people.

TABLE OF CONTENTS

LIST OF TABLES

LIST OF FIGURES

ABSTRACT

In recent years, there has been a gradual surge in the demand for fiber-reinforced plastics (FRPs). The implementation of FRPs can be observed across nearly every industry, ranging from advanced applications in aviation to the simplest components of a bicycle. Besides the non-corrosive and lightweight nature of FRPs, the recent driving forces behind this demand are the continuous reduction in composite costs, eco-friendliness and recyclability, and the ease of integration from a manufacturing perspective. Additionally, aside from the critical and desirable attribute of non-corrosivity, FRPs offer the advantage of high specific strength and stiffness, often surpassing that of commonly used engineering materials such as metals. However, like most materials, there are drawbacks.

Commonly used FRPs consist of materials like carbon, aromatic polyamide, and glass, which come in the form of fibers thinner than human hair. In structural applications, these fibers are commonly embedded in thermoset matrices such as epoxy or vinyl ester resins, and to a significantly lesser extent in thermoplastic resins. The fibers primarily bear the load, while load sharing among the fibers, and the structure and form of the FRP are maintained by the matrix. One of the significant drawbacks is that reusing or recycling thermosetting polymer is virtually impossible, thus contributing significantly to plastic waste in industries that employ FRPs. Another notable drawback is that thermoset FRPs, as mentioned earlier, are susceptible to damage under impact events, partially due to the brittle nature of the matrix materials. This can potentially compromise the structural integrity of vital components during impact events.

Elium©, the world's first thermoplastic resin, with its relatively higher ductility and toughness, has the potential to enhance composites and address the aforementioned issues. Elium© is fully recyclable, potentially reducing plastic waste associated with thermosetting plastics.

Moreover, the increase in ductility offered by Elium© has the potential to enhance the impact resistance of composites, leading to longer service life and increased part durability. The limited research on Elium composites, especially on FRPs made of different fibers, especially eco-friendly fibers, has motivated this study. There is a clear need for a systematic experimental investigation to establish the basic mechanical properties of Elium-based FRPs made with different reinforcing fibers, particularly to establish their low and high-velocity performances. This thesis outlines the experimental methods used to characterize the basic mechanical properties and both the low-velocity impact (LVI) and high-velocity impact (HVI) responses of various composites fabricated using the novel Elium 150. The results from these experiments will be compared to those of composites containing a commonly used room-cured epoxy resin. Moreover, the viability of Elium-basalt composite as a fully recyclable and sustainable composite will also be systematically evaluated. This thesis also aims to provide a comprehensive overview of the principles and methods involved in both low and HVI testing. Furthermore, it outlines the methods, materials, and equipment employed in carrying out this experimental investigation.

LIST OF ABBREVIATIONS USED

LVI	Low-Velocity Impact
HVI	High-Velocity Impact
FRP	Fiber-Reinforced Plastic
PMMA	Poly Methyl Methacrylate
MMA	Methyl Methacrylate
VARTM	Vacuum-Assisted Resin Infusion Molding
CSM	Chop Strand Mat
WATG	Wedge Action Tensile Grip
CLC	Combined Loading Compression
DLVDT	Dynamic Linear Variable Differential Transformer
SEM	Scanning Electron Microscope

ACKNOWLEDGEMENTS

I would like to extend my most heartfelt thanks to everyone who helped me not only in the writing of this thesis but in the entirety of my academic career.

Firstly, and most importantly I would like to extend my most grateful thanks to my academic supervisor Dr. Farid Taheri for his support, encouragement, and commitment to my success throughout my academic endeavour at Dalhousie University. His commitment to the success of his students shines through as an example of what educators should strive to be.

Secondly, I would like to extend my thanks to the members of my thesis committee, Dr. Robert Bauer, and Dr. David Chen. Their constructive recommendations, time, and effort are invaluable in the writing of this thesis and the work performed within it.

Next, I want to thank my father for all of the help he has afforded me throughout my life. He has always been there for me, encouraging my curiosity, and pushing me to be the best version of myself. I am the person I am today because of him.

I want to thank all the members of my family for being there for me and encouraging me to reach for the stars.

Next, I would like to thank my partner Annabe, her unfailing love and devotion has been instrumental in my success.

Last but definitely not least, I want to thank my colleagues and friends for supporting and helping me with my thesis.

“If I have seen any further, it is by standing on the shoulders of giants”.

-Issac Newton

Chapter 1: Introduction

1.1. Overview

In this chapter, the motivation for this thesis along with the specific objectives and goals of this research and thesis will be outlined. Moreover, the relevance and importance of impact analysis as it pertains to fiber-reinforced plastics will be briefly introduced. Lastly, the outline of this thesis, including a summary of the contents will be presented.

1.2. Motivations

Although in recent decades the utilization of composites has been increasing in industrial applications, there still exist manufacturing limitations that lead to increased cost and inefficient applications due in part to the implementation of protective measures [1, 2]. In the aviation industry, the increase in the use of composites has been extensive. Boeing recently introduced the first passenger aircraft, Boeing 787, with 50% of its total materials made of FRPs. This led to significant innovations, but the limitations of the FRPs became increasingly apparent [2]. For example, the leading-edge surfaces of the aircraft all had to have extra layers of protective material, usually in the form of metal cladding or excluding composites completely from these impact-prone areas [1,2]. Furthermore, the maintenance personnel were instructed to perform duties with extra care to avoid dropping any object onto the surface of the aircraft, especially on load-bearing surfaces [3]. Given that a Boeing 787 is a multimillion-dollar aircraft, the cost of an impact from something as small as a handheld tool becomes apparent. This cost from both a financial and safety perspective is not limited to aviation. FRPs, because of their properties, are finding applications in the

marine, automotive, sporting goods, and construction industries to name a few. All these fields have significant safety implications from premature failure of components. It is worth noting that this issue of poor impact resistance is a well-researched phenomenon. The use of other matrix materials and reinforcing fibers have been widely investigated [4]. Thermoplastics like high-density polypropylene, polyvinyl chloride, and nylon have been investigated as alternatives for large-scale engineering applications [4,5]. Persistently, the issue of ease of application still exists. During their manufacturing process, these plastics must be heated to their melting temperature, which in some cases can be as high as 270 ºC. They are then injected under high pressure into a mold. The molds cannot be too large as the plastic can solidify before full impregnation is achieved. The risk of this increases if the mold is not pre or continuously heated. There is also the issue of fiber wetting. This becomes more problematic with conventional thermoplastics as high viscosity and fiber-polymer incompatibility become more pronounced [6]. From a manufacturing perspective, these issues increase the overall cost and require extra processes that can be partially avoided with the use of two-part thermoset resins like epoxy or vinyl ester. Elium©, a liquid Methyl Methacrylate thermoplastic resin, offers a potential solution to the drawbacks of the other thermosets and thermoplastics. The literature review on the comparison of the mechanical properties of Elium with epoxy shows promise by ranking Elium that has a similar ultimate tensile strength to epoxy but a significantly greater compressive strength [7,8,9], and greater ductility and fracture toughness. Ease of implementation in manufacturing has also been a limiting factor for materials that show promise from the perspective of their mechanical properties. Elium's chemical cross-linking process is

initiated by the implementation of a catalyst or by UV radiation [9]. This process must be performed in an oxygen-free environment as oxygen inhibits the cross-linking process [9]. For this reason, to date, parts manufactured with Elium are limited to vacuum molding techniques [9]. These techniques involve either the hand layup of Elium composites that are then encapsulated in a vacuum bag, followed by the application of vacuum, or vacuum-assisted resin infusion. Upon further investigation, vacuum-assisted resin infusion can lead to the realization of another potential benefit for Elium composites. This process involves applying a vacuum once the fibers have been orientated as per the design, and then using the pressure differential to infuse the resin into the fibers. Elium shows promise in this regard with its low viscosity relative to epoxy [8,9]. The cross-linking period of thermoplastics and thermoset resins limits the rate of resin infusion, in turn necessitating the use of slow or ultra-slow hardeners, which in turn decreases efficient part turnout. Luckily in most performance-demanding industries like aerospace and automotive, the vacuum molding processes are standard processing protocols with epoxy resins as the curing usually is assisted in an autoclave to further increase the part quality. The extensive use of this molding process would indicate that most existing manufacturing equipment would not have to be replaced or updated to incorporate Elium. The potential of this material and the benefits offered warrant further investigation to validate these hypotheses.

1.3. Research Objectives

The primary objective of this research is to assess the viability of Elium resin as a suitable alternative to the commonly used resins (e.g., epoxy, polyester and vinyl ester resins), especially in applications where impact events are highly probable and of concern.

This assessment is to be achieved by experimentally evaluating the basic mechanical response of various Elium composites made of different reinforcing fibers and characterization of their basic mechanical properties and low- and HVI performance. The results of these impact analyses are then to be compared to those of composites of similar composition, where the matrix resin is replaced with a room-cured epoxy resin. Another important objective of this research is to establish the viability of Elium-basalt composite as a fully recyclable and sustainable composite. To realize the goals of this research are outlined as follows.

i) To establish the fundamental mechanical properties (i.e., tensile, compressive, and shear responses) of Elium and epoxy-based composites consisting of E-glass, aramid, and basal fibers according to the pertinent ASTM standards. These properties will be analyzed and compared showing the various behaviors of the materials.
ii) To establish the ballistic limit of the composites using the bisection method outlined by the US Army Research Laboratory [10]. The obtained ballistic limits will then be compared and analyzed. A high-velocity gas gun is used to facilitate high-velocity impacts.
iii) Thirdly, once the ballistic limits have been established, the failure modes of the composites will be documented and compared. This comparison will note the type of failure mode and whether partial or complete penetration has happened.
iv) Then, using a modified Charpy impactor, the LVI performances of the composites will also be evaluated. This evaluation will entail establishing the impact force-

displacement characteristics of each composite. This data will then be analyzed to show the material response to the impact event.

v) Once that low-velocity response has been outlined the low-velocity failure modes will be documented and compared. failure modes of penetration, fiber tear-out, delamination, and so on will be compared marking whether the failures constitute a more ductile or brittle failure.

vi) Finally, the viability of Elium-basalt as a fully recyclable and sustainable composite will be assessed and discussed.

1.4. Thesis Overview

As briefly stated earlier, this thesis covers the assembly, testing, and characterization of a series of fiber-reinforced composites consisting of three different fibers (i.e., E-glass, aramid, and basalt) and two resins (i.e., a thermoset epoxy and a thermoplastic liquid resin, Elium). This thesis contains seven chapters; chapter 1 is an introduction to the thesis, covering the motivations, research objectives, and thesis overview. Chapter 2 contains the literature review. The literature review is a summary of the relevant scientific research as it relates to composites, low-velocity, and HVI analysis. Chapters 3, 4, and 5 introduce the material selection and the methods utilized in the synthesis process. This introduction includes a detailed overview of the selected fibers and the matrix materials. The properties of these materials are experimentally investigated, and their fabrication methods are highlighted. The results of the mechanical property tests, low-velocity and high-velocity tests are introduced in chapter 6, including the discussion of the results. Lastly, the

conclusions of this research and the recommendations for future research are provided in chapter 7.

Chapter 2: Literature Review

2.1. Overview

In this chapter, the scientific foundation for the investigation of the low and HVI characterization of Elium-based composites is introduced. In the first section, the low and HVI behaviours of FRPs are presented. Including the relevant scientific research and literature on impact testing and analysis and the material responses. Lastly, Elium's application and behaviour as it pertains to high and LVI is then presented.

2.2. Low-Velocity Impact

When designing a material that interacts with the natural environment, the consideration of how the material responds in the event of a collision or impact of some sort is important. Concerning FRPs, the topic of impact mechanics has a higher degree of importance. Consider a material like aluminum under an impact loading condition. A large deformation (indentation or penetration) will result if the impact event involves high localized energy. This deformation, as it pertains to LVI will be non-detrimental to the overall structural integrity of the piece because most metals are relatively ductile and therefore can absorb a significant amount of energy. At times, when the metal experiences strain-hardening effect, it will offer some additional degree of protection to future events; the same do not hold for FRP composites.

Loads applied in the through-thickness directions, whether statically or dynamically applied, expose the weakness of FRPs since they usually lack any through-thickness

reinforcement. Such loadings develop localized interlaminar shear and tensile stresses, in turn causing damage to the composite. These stresses are usually the initial causes of structural failure on the microscopic level. For this reason, design failure strains are usually as low as 0.5% [11, 12]. This low design failure strain has the undesirable effect of significant material strength under-utilization. As the velocity range of an impact varies, so does the effect on the material. For this reason, the impact velocities are classified into ranges of low velocity, high velocity, and hyper velocity. At low velocities, the interaction between the material and the impactor is long enough for the effect of the event to extend beyond the zone of impact. Cantwell and Morton classified LVI as an impact event that takes place below 10 m/s [11]. This value gives a good approximation for most materials, but Davies and Robinson [13] outlined a more accurate method by considering the through-thickness stress wave and its effects using Equation 2-1.

$$\varepsilon = \frac{V_o}{C} \qquad \textit{Equation 2-1}$$

where ε is the strain in the material, V_o is the impact velocity, and C is the speed of sound in the material, indicating that the stress wave dominant effects start taking place between 10-20 m/s [13].

The failure modes that are observed during an impact event can be classified as follows:

- Delamination is a crack that is located in the resin portion of the composite between the fiber layers or plies. Liu found that delamination was found to occur when there existed a strong difference gradient in the bending stiffness between fiber layups [14]. He also observed that delamination would have an oblong appearance with the longer axis being parallel to the fiber direction below. This delamination is

observable in the high-intensity light image seen in Figure 2-1 below. It was also found by Dorey, that delamination would become more likely for composites with a shorter length and greater thickness [15]. This increased delamination based on geometry observation agrees with the finding of Liu [14], since he theorized that induced bending stresses are major causes of delamination.

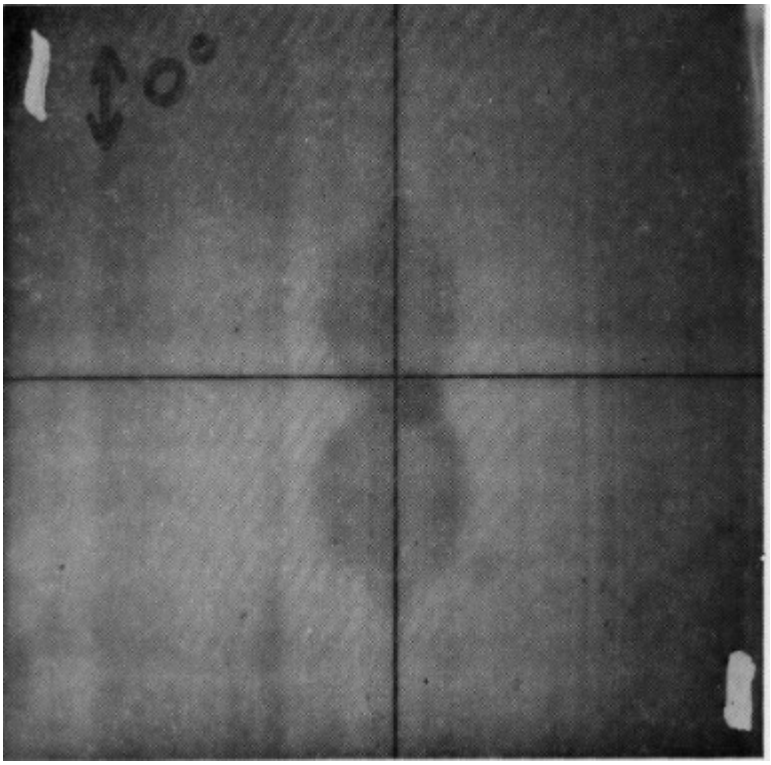

Figure 2-1: High-Intensity light image [14]

- Matrix Cracking is the event where energy is absorbed leading to the formation of micro and macro cracks. Unlike in delamination, matrix cracking occurs across fibers. This effect usually occurs when the impact energy is usually within a smaller range of values, usually below 5J. Damage to the matrix is usually the first form of damage during and impact event. Joshi and Sun found that matrix cracks are usually located in parallel planes to the fiber direction [16]. They found that these cracks formed due to the existence of a differential gradient between the properties of the fiber and matric material [16]. These cracks can be categorized into two categories

bending cracks and shear cracks [17]. The shear cracks are formed when there exists an environment of high traverse shear stress as can be found during an impact event [17]. These shear cracks are usually orientated at a 45° angle to the fibers. The bending cracks are usually perpendicular to the fibers and originate between fiber layers at the boundary of the fiber-matrix interface. A diagram of these crack features can be seen below in Figure 2-2.

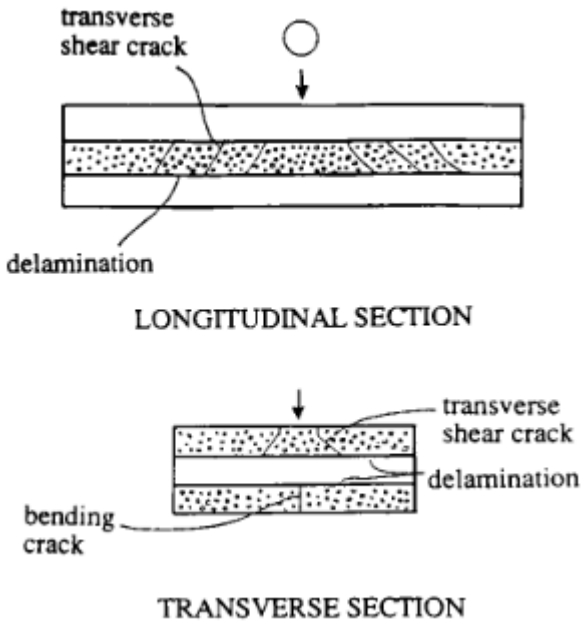

Figure 2-2: Matrix Crack Diagram [17]

- Penetration occurs at higher impact energy levels where significant damage is sustained to both the matrix and the fibers. Once significant damage has been sustained by the matrix, the fibers become principal load-bearing members. Cantwell and Morton found that the mode of penetration that has the highest energy absorption is the shear-out failure [18]. This failure mode is where a plug of material is sheared out of the composite panel with this mode absorbing between 50-60 % of the impact energy varying based on the thickness of the composite [12,18].

As stated previously, in FRPs, fibers are the main load-bearing constituent, while the matrix facilitates the effective transfer of load, fiber alignment, and fiber protection. The true potential of the FRP cannot be realized since the most commonly used matrix material, epoxy has low fracture toughness. As mentioned previously low design failure strain leads to underutilisation of the full fibre strength, reducing the application feasibility of composites in many regards. Sela and Ishai found that an improvement in fracture toughness can lead to the application of failure strain values 50% higher than currently utilized [19]. They found that the use of thermoplastic resins like poly ether ether ketone gave an order of magnitude higher fracture toughness but had the drawback of poor fibre-resin interface bonding [19].

2.3. High-Velocity Impact

The importance of considering the effects of impacts at higher velocities becomes apparent once one considers the type of engineering structures that will be subjected to such events. Aviation, automotive, space, and marine industries are a few sectors where the design and development must account for aspects of impact dynamics. The extent of the use of composites in an aircraft can be seen in the example shown in Figure 2-3. Consider a jet engine's fan blade, a vital component to the safe operation of an aircraft. If and impact event is to take place and the effects were not considered in the design the consequences could be devastating. Now FRP composites are finding more and more use

within these sectors. The impact properties of these materials are also growing in importance.

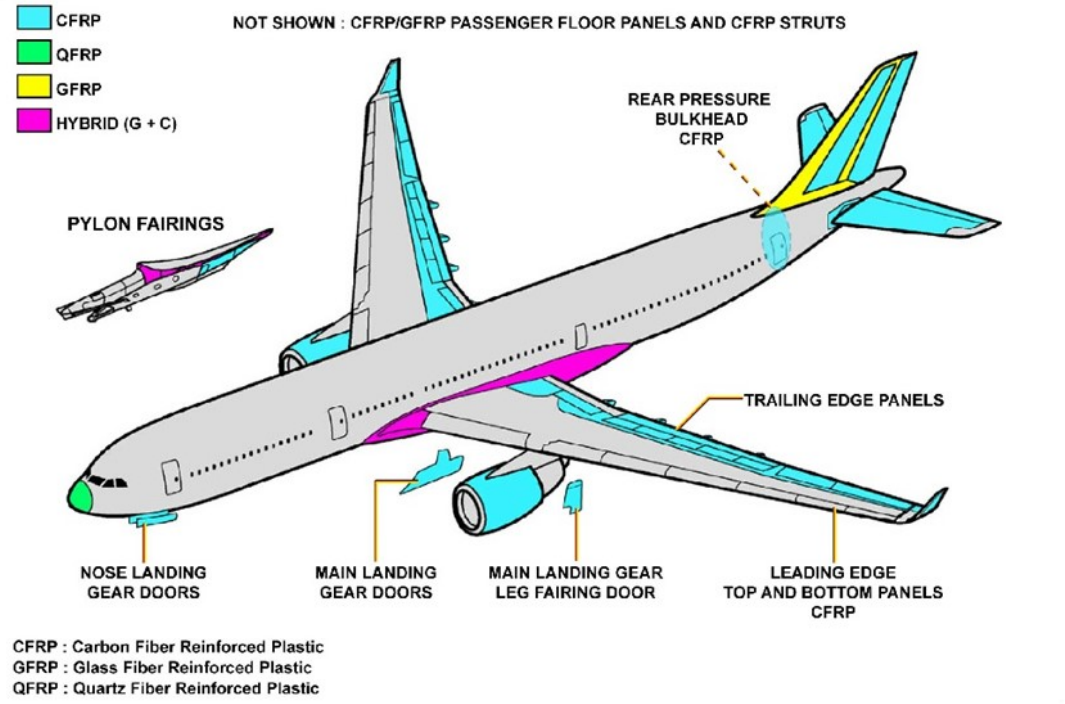

Figure 2-3: Airbus A330 FRP Composite Parts [20]

A HVI can be classified as an impact where stress wave effects dominate the event. The velocity domain where stress wave effects dominate can be found using Equation 2-1. considering the increased strain rates achieved for the higher velocities [21]. Olsson found that during an impact event, there exists a continuum of three wave types [22]. For impacts where the time of the event approaches the through-thickness wave propagation times, the wave is dominated by 3-dimensional dilatational waves [21,22]. As the time of the impact event increases the waves transition to flexural waves until a quasi-static state is achieved [21,22]. A diagram of the three waves can be seen in Figure 2-4.

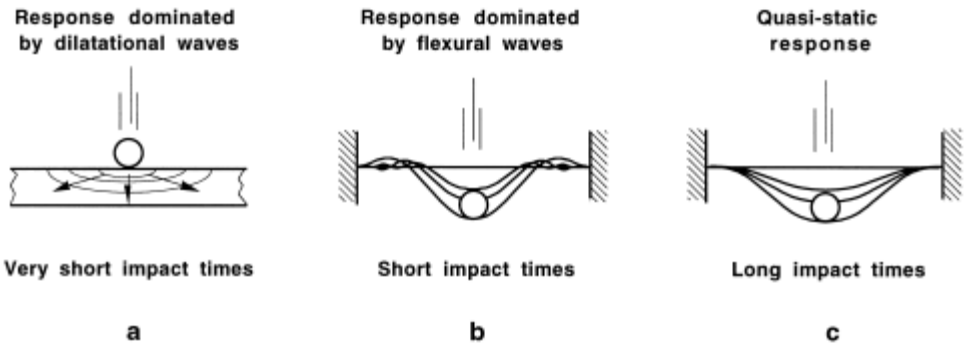

Figure 2-4: Impact wave types [22]

Olson also found that the size of the target and the boundary conditions affected the quasi-static waves but had no effect on the dilatational, flexural, and shear waves [23]. The failure modes seen in the LVI of delamination, matrix cracking, and penetration all take place during an HVI event. The difference between the two is that at lower velocities one mode can be experienced depending on the energy of the event. While at higher velocities it is almost always a mixed-mode failure.

Another parameter of consideration is the angle of impact. The angle at which the impactor strikes the target can have a tremendous effect on the ability of the composite to absorb energy at large angles of incidence [24]. It was concluded by Siva Kumar and Bhat that small increases in the angle of impact had minimal effect on the energy absorbed, but once the angle of incident surpassed 30^{o} an increase in the energy absorbed can be observed [24]. At higher velocities, the probability of a penetration event increases. The modes of penetration have a further delineation depending on the material and its properties. During an impact event, a compression wave is generated. If this wave exceeds the compression strength of the material radial fracturing will occur this is common for material where the

compression strength is greater than the tensile [20,25]. Petaling occurs when a high amount of tensile stress is developed at the back side of a panel during an event and released once the damage has occurred. Fragmentation is caused by localized pulverization of the material upon impact and is seen more prominent in brittle material [20,25]. Plugging is where a cylindrical mass of the target material is ejected during an impact event. Plugging is caused by a high amount of through-thickness shear stress development around the boarders of a blunt projectile [20,25]. The diagram seen in Figure 2-5 outlines the penetration events mentioned.

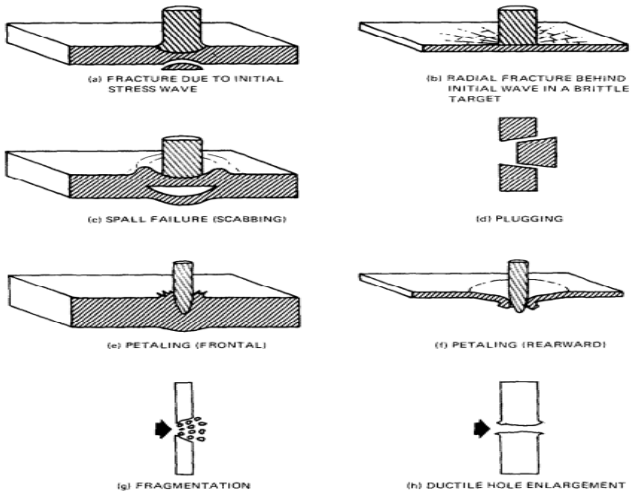

Figure 2-5: Perforation mechanics [25]

The ability of a material to resist penetration in most cases would be beneficial. For composites under loading conditions, a non-penetration event would mean that the material retains some amount of its load-carrying capacity [26]. The velocity at which a material is penetrated is classified as the ballistic limit. This value varies for each material and configuration. Extensive work has been done in determining predictive models for both

composites and common engineering materials [25,27]. These models have shown to be good at approximating values but the error in the predictions is too large for engineering applications [10, 27]. Ferriter *et al.* investigated which method of obtaining the ballistic limit would give the best results [10]. They investigated the Bisection method, the Jonas - Lambert, V_s and V_r relationship method, the Golden Ratio method, Residual Energy vs the angle of the projectile relationship method, and the residual energy vs V_r relationship method [10]. They concluded that the bisection method gave the lowest error values of 1 m/s with a sample size of 5.5 specimens [10].

The projectile geometry is a factor that determines how the material will fail during penetration [28]. Mines *et al.* Investigated how the shape of the projectile head would affect the ballistic limit of the material [28]. They found that the impactor with a hemispherical geometry had the highest target energy absorption for stitched fabric while the flat impactor had the highest energy absorption for the woven fabric [28]. The flat impactor would cause material failure mainly due to shear while the round impactor would cause a mixed failure mode involving tensile, shear, and bending [28]. The conical impactor was also found to have a mixed failure mode of tensile and shear failure modes [28]. The geometry of the projectiles used by Mines *et al.* can be seen in Figure 2-6.

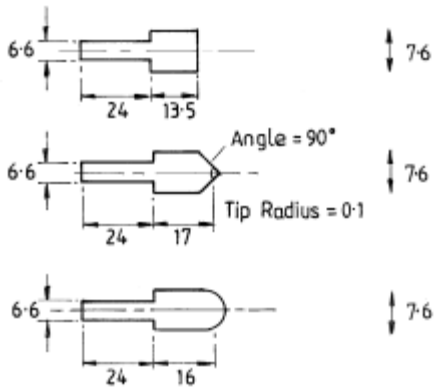

Figure 2-6: Projectile Geometry [28]

2.4. Elium Resin

Elium resin is a low viscosity liquid thermoplastic resin with the chemical name, poly methyl methacrylate (PMMA). It was developed by Arkema S.A. in France as a potential replacement for epoxy resin which sees extensive use in the FRP industry. Elium resin undergoes the chemical crosslinking process by radical polymerization where its monomer methyl methacrylate (MMA) transitions to its polymer form PMMA through the use of a peroxide catalyst [29, 30]. This polymerization process can be seen in Figure 2-7 below.

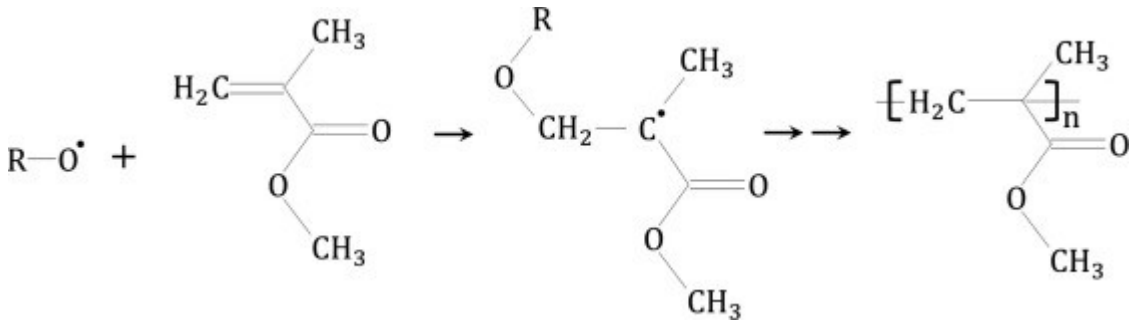

Figure 2-7: MMA Radical Polymerisation [29]

When a composite incorporates a thermoplastic as the matrix material, a significant

improvement in the through-thickness performance would be observed [31]. The reason for this improvement is due to the chemical structures that exist with a thermoplastic [31]. Thermoplastics intermolecular bonds are formed by a Van Der Waals interaction while thermoset plastics intermolecular bonds are formed by stronger cross-linking bonds [31].

As mentioned above the fracture toughness of a material dictates how susceptible the material will be to fracturing and crack propagation. In composites, the formation of fractures can reduce the strength of the overall structure through the precipitation of further failure modes such as delamination. Bhudolia *et al.* investigated how the implementation of Elium in the construction of composites with three different fiber types would affect the fracture toughness when compared to composites of the same fiber type with epoxy [31]. They found that with the addition of Elium, a 33% in mode II fracture energy could be gained in composites constructed with Ultra-high molecular weight polyethylene fibers [31]. Barbosa *et al.* conducted similar research into the fracture toughness of composites made with Elium while utilizing carbon fiber [32]. They found that Elium afforded a 40% increase in interlaminar fracture resistance [32].

While fracture toughness is important for resistance to matrix fracture, the use of thermoplastic resins usually comes with the drawback of poor matrix fiber adhesion. The effects of this are observable in the material properties of the composites. When the composite material properties of an Elium-based composite are analyzed, Elium shows similar properties to that of common thermoset resin composites [29,33,34]. Yaghoobi and Taheri investigated how fibers made of naturally occurring basalt would perform when

coupled with Elium [33]. They found a basalt Elium-based composite had a lower modulus of 5% and 23.5% higher tensile strength when compared to an epoxy basalt composite of similar configuration [33]. Once these values were normalized the 5% difference in modulus was mostly removed while the tensile strength increase was realized at 28.4% [33]. When analyzing the flexural properties of Elium, Bhudolia *et al*. found that the viscoelastic properties of Elium afforded a higher ductility under a longer sustained load [34].

When heated, thermoplastics, because of the Van Der Waals interaction, have the ability to easily break and form new bonds and crystal structures upon cooling. This capability of heating and cooling for reforming gives thermoplastic great recyclable properties. Although recycling comes with a few potential drawbacks like void formation, Impurity inclusion, and weakening properties in the crystal structure with proper quality control these drawbacks can be reduced. Allagui *et al.* investigated the recyclability of flax-Elium composites and found that there existed a decrease in the tensile properties of the composite [35] as a result of recycling. Upon further analysis, they discovered the change in the elastic properties was mainly due to the reduction in the fiber size due to the recycling method they utilized [35]. This phenomenon also explains the reduction in the strain to failure that they also observed [35]. Once these factors were controlled, they noticed a decline in resin failure properties that was attributed to changes in the crystal structure from the recycling process, mostly in an increase in the dynamic stiffness and the polymer density [35].

The work done by Allagui *et al.* focused mainly on the recycling of Elium flax composites by thermomechanical methods [35]. Sahki expanded on the work of Allagui, *et al.* by investigating how different recycling methods affected the thermoplastic, also how reinforced Elium with glass, and basalt fiber would compare in their performance. They found that minimal differences in the properties between glass and basalt composite were observed to exist [36]. They also found that by utilizing Solvolysis/dissolution in the recycling process the fibers and resin can be effectively completely recycled with minimal loss in the properties of the recycled composite when compared to unrecycled composites [36]. For the same reasons mentioned above, mainly the weak Van Der Waals interactions, thermoplastics afford the ability to be welded to itself utilizing its melting and remolding capabilities. When the welded joints of Elium composites are compared to that of an adhesively bonded joint, an increase in the fatigue strength of vales ranging from 7%-12% was observed [37].

When analyzing the effects of the damping Elium-based composite offers when compared to an epoxy-based composite a 12% increase in the damping ratio can be observed [38]. While a 27% increase in structural damping of Elium-based composites was observed when compared to epoxy-based composites [38].

Composites are finding greater use in applications that involve higher probabilities of impact events. Since the most commonly used plastic matrix epoxy has a brittle nature, which leads composites to a degree of damage susceptibility not seen in most other structural materials. The use of thermoplastics has been investigated before with poor

outcomes in the mechanical properties caused by improper adhesion between the fibers and the matrix. Novel Elium being a low-viscosity liquid thermoplastic resin offers potential as a solution. There is minimal research in the area of impact analysis for Elium, more so in a HVI context but the existing work in the LVI analysis shows promise. When a composite composed of an Elium matrix with non-crimping carbon fiber was compared to its counterpart composite made with epoxy matrix, it was observed that the Elium-based composite underwent a higher elastic deformation of 53% more until its failure [39]. It was also observed that the Elium-based composite absorbed 58% more energy before the onset of a major failure [39]. This energy was absorbed mainly in the elastic-plastic deformation of the test specimen [39].

Kazemi *et al.* also found in their research that Elium-based composites had a remarkable 240% increase in structural integrity post-impact when compared to epoxy-based composites [40]. The results of Elium-based composites absorbing more energy and retaining higher structural integrity from LVI testing have been replicated in a multitude of research works [39,40,41,42,43,44,45]. As mentioned previously there exists very limited research on how Elium-based composites perform under HVI and how their HVI behaviour compares to commonly used epoxy-based composites. Libura *et al.* investigated how the ballistic limit of Elium-based composites was effect by fatigue and aging [46]. They found that fatigue and aging deteriorate the interface between the fiber and matrix leading to a reduction in the stiffness and ballistic performance of the composite [46].

Chapter 3: Materials

3.1. Overview

In this chapter, a detailed introduction of the materials used for the high velocity, low velocity, and material properties tests are covered. This introduction includes the reinforcing fibers and the matrix materials.

3.2. Matrix Materials

The matrix material is the binder that gives the composite its form. It maintains the separation and spacing of fibers while transferring any externally applied load to the reinforcing fibers. This load transfer property is achieved through shear stress transfer, where good fiber wetting and adhesion are important factors that aid in the avoidance of events like fiber pull-out. The matrix also protects the fibers from environmental and physical contact that would otherwise degrade the load-carrying capacity of the fibers. This degradation comes in the form of fiber premature failure from surface crack propagation from abrasive physical or chemical exposures. The matrix material carries a very small fraction of the total load and for the proper function of the composite should have good fiber whetting properties. The elastic-plastic nature offers protection so that brittle fractures are not propagated between fibers. Depending on the application of the composite, the matrix material may vary. It can be composed of polymers, ceramics, and metals. Composites that are subjected to harsh environments that include temperatures as higher than 700 ˚C are usually constructed with matrix materials composed of Ceramics or metals

[47,48]. Examples of such an environment include the combustion section of a gas turbine [47,48]. Polymer-based matrix materials usually find use in structural applications like the chassis of an automobile or the load-bearing portion of an aircraft.

3.2.1. Elium© 150

The Elium 150 resin used in this research was supplied by Arkema Inc, Arkema, Inc., PA, USA. As briefly mentioned earlier, Elium is the first low-viscosity liquid thermoplastic resin. Elium, because of its chemical nature, is limited to manufacturing techniques that employ the use of low-pressure processes like vacuum-assisted resin infusion molding (VARTM) or resin transfer molding. Elium is a two-part system with part A, the Elium resin and part B, the curative agent, Arkema's Luperox organic peroxide. The recommended ratio of hardener to resin by weight is between 1.5% - 3% [9], while in this research 2% was utilized as this yielded the best performance through trial and error.

During the assembly process, the resin has a maximum pot-life of 30 minutes [9]. The pot-life is the time the resin can be exposed to the external environment and perform nominally. Full curing of the resin can be expected within 24 hours or accelerated to as low as 3 hours by increasing the temperature during curing. As with most liquid resins, the polymerization process is exothermic with a considerable amount of heat released. In fact, it is sometimes necessary to provide a form of heatsinking during the curing process to avoid the temperature of the resin increasing beyond the boiling point of the resin leading to the formation of voids. Once the curing process has begun the resin will begin to turn a pink hue before transitioning to a transparent finish. The manufacturer materials properties

of Elium resin provided by the producer are listed in Table 3-1 below.

Table 3-1: Manufactures Supplied Material Properties of a 4 mm unfilled Cured Elium 150 resin casting [9]

Shore D Hardness	85-90
Tensile Strength	76 MPa
Tensile Modulus	3,300 MPa
Tensile Deformation	6 %
Flexural Strength	130 MPa
Flexural Modulus	3,250 MPa
Compression Strength	130 MPa
Cured Specific Gravity	1.19
Liquid Viscosity	100 mPa·s

3.2.2. West System epoxy

The epoxy resin and hardener used in this research was manufactured by West Systems®. The 105 resin and 206 hardener epoxy system is a room-temperature-cured system and has very low chemical volatility which reduces the required personal protective equipment (PPE) used. This resin system is a two-part system, part A is the 105-epoxy resin and part B is the 206-hardener. The recommended ratio of resin to hardener is 5:1 [8], which is the ratio that was utilized in this research. When implementing this resin, the processes that can be utilized are not limited to vacuum-assisted processes as the crosslinking process will take place in an open environment. However, vacuum-assisted processes are preferred since they would lead to a higher part quantity and a reduction in void formation. This system has a pot life of 20-25 minutes, with a working time of 90-110 minutes, a hardening time of 10-15 hours, and time till full material strength of 1-4 days [8]. During the chemical cross-linking process an increase in temperature and a transition from liquid to a gel-like state can be observed. The increase in temperature is due to this

reaction's exothermic nature and the gel formation is the polymerization process transitioning to a solid. The manufacture's material properties are listed in Table 3-2.

Table 3-2: Manufacture Supplied Material Properties of Cured 105 epoxy Resin [8]

Shore D Hardness	83
Tensile strength	50 MPa
Tensile modulus	3,172 MPa
Tensile elongation	4.5%
Flexural strength	81 MPa
Flexural modulus	3103 MPa
Compression yield	79 MPa
Specific gravity	1.18
Liquid Viscosity	725 mPa·s

3.3. Reinforcing Fibers

In composites, the fibers are the primary load-bearing component. Fibers come in different materials ranging from natural plant-based to synthetically made fibers, as well as hybrid fibers. The most commonly used fiber materials are glass, carbon, and aromatic polyamide fibers. Reinforcing fibers can be smaller than a single strand of human hair in diameter and are usually bundled together into groups of fibers called tows. Given the small diameter of reinforcing fibers, the properties of the fibers are usually found in aggregate by measuring the response of a tow of continuous fibers under loading conditions. Since fibers are the major load-bearing component of an FRP, any variances in the orientation of the fibers will affect the material properties of the composite. This orthotropic nature is dependent on fiber layout and direction, for this reason, cloth of continuous fibers come in different fiber orientation options that can facilitate stacking sequences to produce desired mechanical properties in the varying direction of a composite. A chop strand mat (CSM)

is usually selected to generate an FRP with isotropic-like properties. CSM contains short fibers orientated in a random direction. This random nature is responsible for the isotropic nature of the composite at the expense of the strength since the shorter fibers carry a smaller load due to stress concentration and smaller fiber matrix surface area.

3.3.1. Kevlar© 29 Aramid

The Kevlar fabric used in this research was manufactured by the Dupont™ company. Kevlar is an organic fiber classified within the family of aromatic polyamides [49]. It was first synthesised in the 1960's by the Dupont company which at the time was investigating ways to increase the break strength of man-made fibers. This goal was realized by the discovery of a material with an almost perfect polymer chain extension. This polymer known as poly-p-benzamide formed a liquid crystalline solution due to the simple and repetitive nature of its molecular backbone [49]. The form of this backbone was the structural orientation of the benzene ring [49]. This chemical breakthrough led to the creation of Kevlar. Since its discovery, Kevlar has found use in many industries ranging from aviation to defence. Kevlar, because of its molecular orientation, gives it resistance to concentrated impact events that exceed that of its counterparts. This increased impact strength comes at the expense of its manufacturability since specialized tools are required for processing. The Kevlar used in this research is a fabric mat with unidirectional fiber orientation and a fabric weight of $320\,g/m^2$. The manufacturer material properties are listed in Table 3-3 below.

Table 3-3: Manufacturer Supplied Material Properties of Kevlar® 29 [49]

Tensile Strength	3,600 MPa
Tensile Modulus	83,000 MPa
Density	1.44 g/cm^3
Elongation at Break	3.6%

There are also other types of aramid fibers such as Spectra (Honeywell Performance Materials and Technologies, US), and Tawron (Teijin Limited, Japan)

3.3.2. E-glass

E-glass fibers are inorganic fibers composed of silica and boron trioxide. E-glass has many applications ranging from aviation to the marine industries. It is the most common glass fiber with lower thermal expansion and heat conduction properties. This glass fiber is manufactured by bringing the mixture of its constituents to its melting point then extruded into fine fibers. The glass fiber fabric used in this research is a biaxial 0/90 stitch mat fabric with a weight of $427 g/m^2$, supplied by Burnside Fiberglass (Dartmouth, NS). The manufacturer material properties are listed in Table 3-4 below.

Table 3-4:Manufacturer Supplied Material Properties of E-glass Fiber [50]

Tensile Strength	3,400 MPa
Tensile Modulus	72,000 MPa
Density	2.54 g/cm^3
Elongation at Break	4.7%

3.3.3. Basalt

Basalt is a naturally occurring substance, it is formed when lava from a volcanic flow solidifies. For this reason, basalt is classified as a type of igneous rock. It has a composition

that is approximately 50% silica, 18% aluminum oxide, and 10% iron oxide, along with other trace minerals [51]. Since basalt is a naturally occurring substance, the processing required to produce basalt fibers is significantly smaller when compared to other available fibers. Also, given its natural origins, its waste would have a small impact on the environment, especially if the fibers are paired with a recyclable matrix. The smaller environmental footprint gives rise to the potential for basalt to be implemented as an environmentally friendly replacement to existing fiber reinforcement materials. Basalt is manufactured by first raising the substance to its melting point and then extruding the melt products to produce the fiber. Basalt fiber has found use as an insulating material because of its thermal properties, and as a structural material since its mechanical properties are comparable to other available reinforcing fibers. The basalt used in this research is a continuous fiber stitched mat biaxial 0/90 fabric with a fiber weight of 516 g/m^2. The manufacturer material properties are listed in Table 3-5 below.

Table 3-5:Manufacture Supplied Mechanical Properties of Basalt Fibers [51]

Tensile Strength	4,840MPa
Tensile Modulus	89,000 MPa
Density	2.70 g/cm^3
Elongation at Break	3.15 %

Chapter 4: Fabrication of Various Composites

This chapter provides a detailed description of the manufacturing method employed for the creation of the various composite laminate panels and the test specimens used in various testings.

4.1. Fabrication Procedure of Composite Panels

The composite fabrication method utilized in this research is vacuum-assisted resin infusion molding (VARTM). This method is utilized for the following reasons:

- it creates consistent part quality.
- Elium® requires a low-oxygen environment.
- the fiber/resin ratio is more controllable.

The materials required for this method are the impregnation resin, the fibers (or fabrics), vacuum bagging, peel ply, breather cloth, sealant tape, spiral tube, infusion tube, and infusion mesh. The peel ply is a non-stick material that facilitates the ease of removal of the finished part. Different grades can be used to get varying surface finishes. The infusion mesh aids in the proper infusion of resin since during the vacuuming process the entire assembly will be under vacuum and the resin flow will be somewhat impeded without the mesh.

The first step in this method is the measurement and cutting of the fabric, peel ply, infusion mesh, vacuum bag, breather ply to the desired sizes, and sealant tape, to the desired length. Then the first layer of the vacuum bag is placed on a level rigid aluminum plate.

The next step would be to place the first layer of the peel ply followed by placing fabric layers in the specified orientations with the second layer of peel ply placed on top of the laid laminate. The spiral tube that facilitates resin distribution is wrapped in peel ply and placed across the inflow edge of the layup. A similar spiral tube (though without a peel ply) is placed on the opposite outflow edge of the layup. Next, sealant tape is used to seal the ends of the inflow and outflow tubes. The resin inflow and outflow hoses are placed in the middle of the inflow and outflow spiral tubes. Lastly, sealant tape is applied around the perimeter of the layup and then the final piece of vacuum bagging is placed onto the entire assembly. Great care is taken to ensure a proper seal is made between the two vacuum bag layers before the resin inflow is initiated.

In the next step, the resin is prepared with a resin-to-fibre weight ratio of 1.10:1 (the uneven resin ratio is to facilitate the resin losses). The resin and hardener are mixed thoroughly and then placed in a vacuum chamber to remove the entrapped air. The mixture is then transferred through the tubing and through the peel ply with the aim of obtaining a final resin to fiber weight ratio of 1:1. Once a proper seal is secured, a vacuum is applied to the outlet and the resin is permitted to flow into the inlet, wetting the laid fabric assembly. Once the resin has flowed through the layup and reached the outlet, a clamp is placed on both the in and outflow tubes and the vacuum pump is turned off. The assembly is left to cure under vacuum for 24 hrs. Then the cured laminate is uncovered by removing the various covering layers of materials. The various reinforcing fabrics and the vacuum bagged systems are shown in Figure 4-1.

Table 4-1 outlines the various composite laminates fabricated in this study.

Table 4-1: E-glass, Basalt, and Kevlar 29 composites and their Layup Sequences

Property	Resin Type	Layup sequence
Tensile	Epoxy 105, Elium 150	$[0,90]_s$
Shear	Epoxy 105, Elium 150	$[0,90]_s$
Compression	Epoxy 105, Elium 150	$[0,90]_s$
Impact	Epoxy 105, Elium 150	$[0,90]_s$

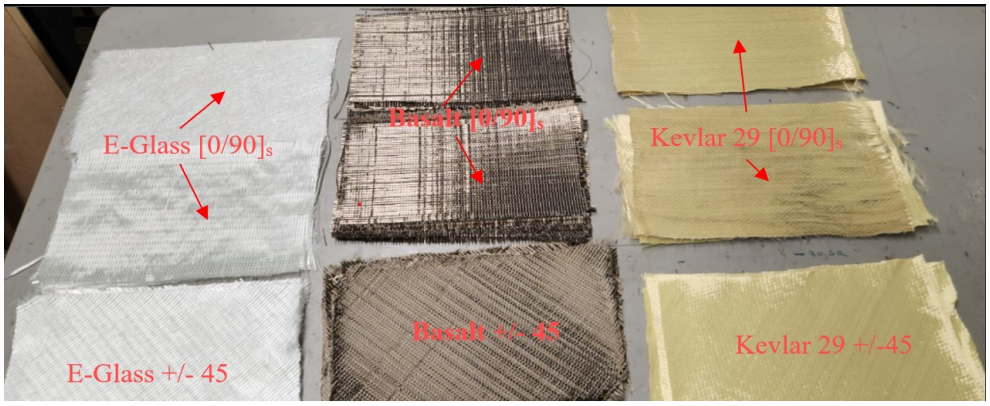

(a)

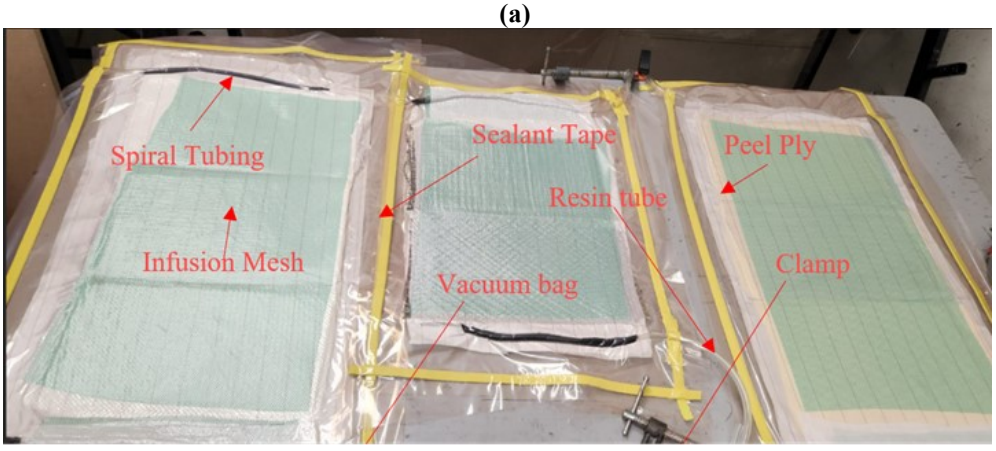

(b)

Figure 4-1: (a) Composite fiber reinforcement Layout, (b) vacuum Resin Infusion Setup

4.2. Description of Test Specimens for Mechanical Properties Evaluation

The specimens for the tensile, shear, and compression tests were prepared in accordance with the ASTM D3039, D3518, and D3410 standards [52,53,54]. The geometries and dimensions of the specimens are illustrated in Figure 4-2 and Figure 4-3. The fiber layup of [0/90]s, [+45/-45]s, and [0/90]s were adopted for the tensile, shear, and compression test specimens, respectively. As can be noted, the fiber orientation in the tensile and compression test specimens is different from the specimens for shear tests. and shear specimens as per the standards.

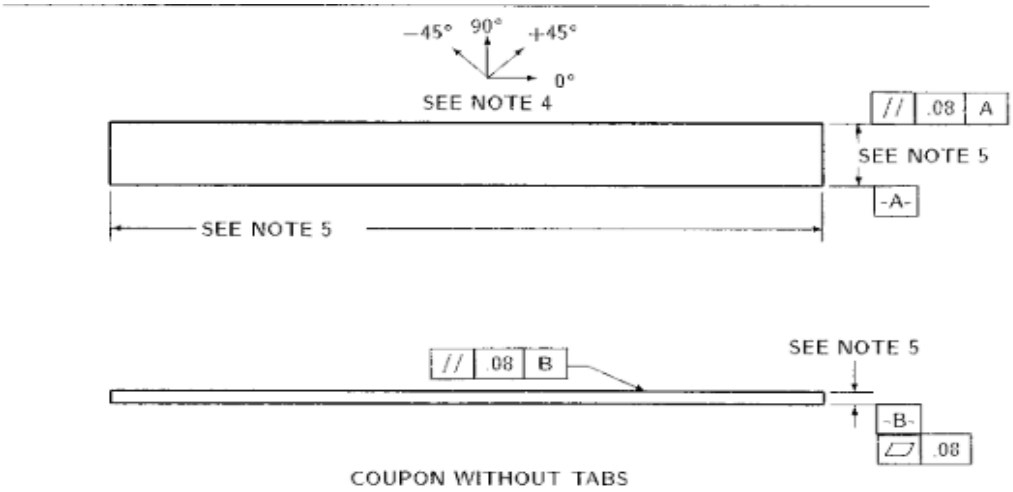

Figure 4-2:ASTM Tensile Test Specimen Configuration [52]

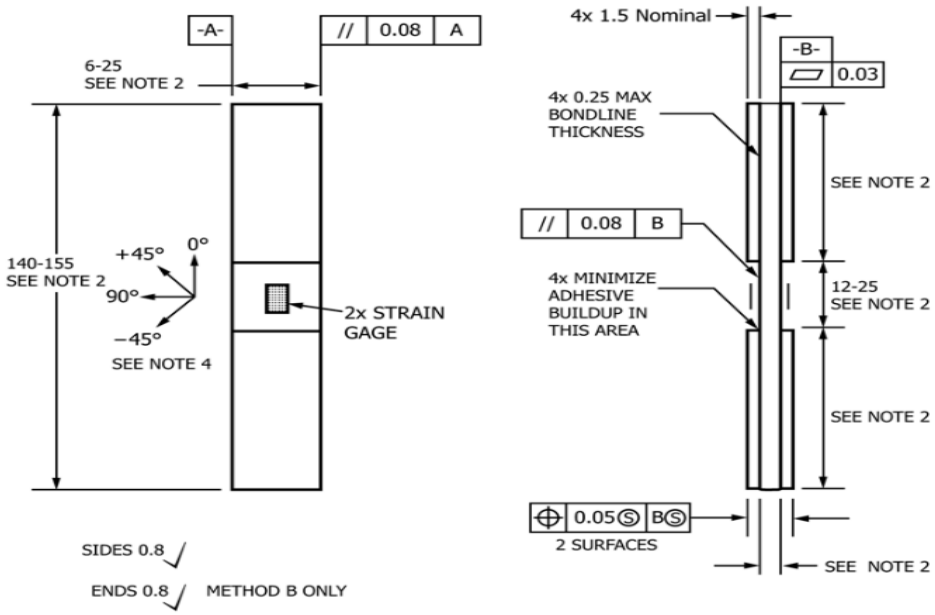

Figure 4-3:ASTM Compression Test Specimen Configuration [53]

Test specimens were extracted from the panels produced and listed in Table 4-1. A diamond-coated rotary saw was used to extract the test specimens from the composite panels made with E-glass and basalt fabrics. The Kevlar composite specimens were extracted using a water jet cutting machine since aramid composite cannot be cut by the rotary saw. The ASTM recommended dimensions of the tensile and shear specimens are 25×250×2.5 mm [52,54]. One requires a few assumptions to establish the gauge length or conversely the thickness of the compression test specimens to preclude buckling of the specimens. Equation 4-1 is used to calculate the minimum required thickness in accordance with the standard using the values in Table 4-2 below [53]. Where l_g is the gauge length, F^{cu} is the ultimate compressive stress, G_{xz} is the through-thickness modulus, and E^c is the Longitudinal modulus of elasticity.

Table 4-2: Compression Specimen Thickness Calculation Parameters

Parameter	E-glass	Basalt	Kevlar-29
l_g	$15\ mm$	$15\ mm$	$15\ mm$
F^{cu}	$45\ MPa$	$45\ MPa$	$40\ MPa$
G_{xz}	$1000\ MPa$	$1000\ MPa$	$1000\ MPa$
E^c	$6000MPa$	$6000MPa$	$6000MPa$

With these values, a minimum thickness of approximately 1.55 mm is obtained for all the test specimens. Therefore, the dimensions of the compression specimen are as follows, 25×145×2mm. The final constructed Tensile, shear, and compression samples are illustrated in Figure 4-4.

$$h \geq \frac{l_g}{0.9069\sqrt{(1-\frac{1.2F^{cu}}{G_{xz}})(\frac{E^c}{F^{cu}})}} \qquad \textit{Equation 4-1}$$

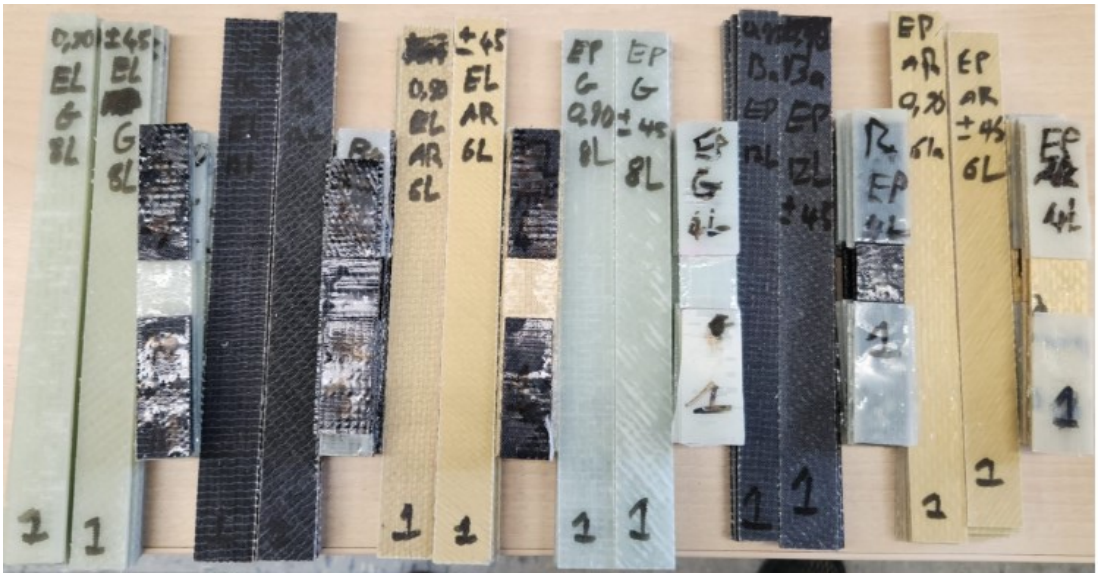

Figure 4-4: Various specimens prepared for mechanical properties evaluation

4.3. Low and High-Velocity Impact Specimens

The low and high-velocity impact specimens are manufactured using the same techniques utilized in section 4.1 with the selected fiber orientation of $[0/90]_s$. The specimens were constructed as per ASTM 7136 [55] guidelines with the dimensions of 150×100mm as illustrated in Figure 4-5 (a) [55].

The specimen thickness for the high-velocity test was established using Equation 4-2 outlined by Reid and Zhou [27]:

$$v_b = \frac{\pi \Gamma \sqrt{\rho_c \sigma_e} D^2 t}{2m} \left[1 + \sqrt{1 + \frac{8m}{\pi \Gamma^2 \rho_c D^2 t}} \right] \qquad \textit{Equation 4-2}$$

where v_b is the ballistic limit, t is the panel thickness, σ_e is the static linear elastic compression limit, ρ is the density of the composite panel, Γ is the projectile constant, D is the projectile diameter, and m the mass of the projectile. The calculated thickness ensures that specimen penetration will take place within the velocity range capabilities of the gas gun. The gas gun has a velocity range of 85-190 m/s. For an estimation of the necessary panel thickness, values of the terms related to mechanical properties were taken from the experimental results and can be seen in Table 4-3 below.

Table 4-3: Theoretical Ballistic Limit Variable Values

Parameter	E-glass	Basalt	Kevlar-29
t	2 mm	2 mm	2 mm
σ_e	158 MPa	164 MPa	82 MPa
ρ	1490 kg/m^3	1590 kg/m^3	1240 kg/m^3
Γ	1.5	1.5	1.5
D	0.00953 m	0.00953 m	0.00953 m
m	0.0035 kg	0.0035 kg	0.0035 kg

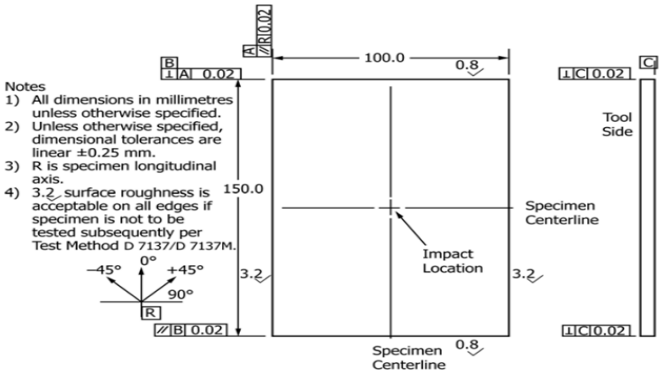

(a)

(b)

Figure 4-5: (a)ASTM Impact Test Specimen configuration [20], (b) the actual low- and HVI test specimens

Using Equation 4-2 shows that 2 mm panel thickness allows for the theoretical ballistic limit to fall within the capability of the gas gun; therefore, the specimen panels will have a thickness of approximately 2 mm. To maintain consistency between the low and HVI analysis, the thickness of the LVI testing specimens will be approximately 2 mm as well. The final constructed test specimens are shown in Figure 4-5 (b).

Chapter 5: Experimental Methods and Setup

5.1. Overview

In this chapter, the equipment utilized for conducting the various tests is described. Moreover, the test methods used to investigate the basic mechanical properties of the composites, as well as the low-velocity, and high-velocity test procedures are also explained in detail.

5.2. Void Content and Fiber Volume Evaluation

The void content of the various composites was evaluated following ASTM D2734-16 [56]. This procedure starts with obtaining the densities of the composites and their constituents. For the composites, this is accomplished by first cutting approximately 20×80 mm rectangular specimens from each composite laminate panel. Next, these specimens are dried in the drying oven for 1 hour to remove any absorbed moisture (see Figure 5-1 (a)). Once the drying phase is completed, the specimens are weighted. Next, a precise graduated cylinder is filled with distilled water to a point so that total submersion of the specimen is accomplished. Subsequently, the volume of water before the specimen's immersion is recorded. The specimen is then immersed in the graduated cylinder and placed into the vacuum chamber as seen in Figure 5-1 (b) until a vacuum of 3 mm-Hg is achieved. The cylinder is then removed, and the volume change is recorded. The process is repeated for all specimens.

The density of the composite, ρ_{comp}, is calculated using Equation 5-1.

$$\rho_{comp} = \frac{m}{\Delta V} \qquad \textit{Equation 5-1}$$

where $m =$ weight in grams and ΔV is the difference in volume in ml.

(a) (b)

Figure 5-1: (a) Drying oven, (b) vacuum chamber

The process is also repeated for samples of raw fibres. The densities of the resins used are obtained from the manufacturer's material data sheets.

After establishing the densities, the resin burn-off test is conducted to obtain the mass percent of the resin and fibres within the composite. The same composite test specimens used in the density tests can be used in the burn-off test. The specimens are first dried in the drying oven for 1 hour in a ceramic crucible to remove any absorbed moisture. The crucible holding the specimen is weighed, and once again, without the specimen the specimen's weight is then calculated. Next, the furnace shown in Figure 5-2 is heated to

500 ºC for basalt and E-glass composites and 400 ºC for Kevlar-29 composites. Once the furnace has reached the desired temperature, the crucible containing the sample is then placed into the furnace for 1-2 hours or until the resin has carbonized and removed from the composite, leaving pure fibres. Once that is accomplished, the crucible and its contents are then removed and left to cool for 30 minutes. Once cooled the crucible and its contents are then weighted. The process is repeated until all samples are tested.

Equation 5-2 is used to calculate the theoretical density ρ_{Theo} [56]

$$\rho_{Theo} = \frac{100}{(\frac{R}{\rho_r} + \frac{r}{\rho_f})} \qquad \textit{Equation 5-2}$$

where R is the resin's weight %, ρ_r is the density of the resin, r is the reinforcing fibers weight %, and ρ_f is the density of the fibers.

Subsequently, the void content, V, is calculated using Equation 5-3 in which ρ_{comp} is the measured composite density [56]

$$V = 100(\rho_{Theo} - \rho_{comp})/\ \rho_{Theo} \qquad \textit{Equation 5-3}$$

Figure 5-2: Furnace used in resin burn-off test

5.3. Basic Mechanical Properties

5.3.1. Equipment and Setup

A digitally controlled MTS servo-hydraulic universal test system was utilized for the evaluation of the basic mechanical properties of the different composites. This system consists of a hydraulically actuated testing system that is controlled via a LabVIEW user interface. The user interface is where the testing rate, sampling rate, and so on are programmed before the test is initiated. For the compression test, the combined loading compression fixture is utilized. This fixture facilitates the pure compression loading of the test specimen through the restriction of all degrees of freedom except within the axial testing plane. The tensile testing setup utilizes the Wedge Action Tensile Grips fixture (WATG). Using a wedge system, this fixture compresses the grip section of the tensile coupon progressively under an applied load. This self-tightening action affords great stability to the test specimen during a testing event.

The strain measuring device used is a Model LE-05 Laser Extensometer manufactured by Electronic Instrument Research (Irwin, PA). This extensometer utilizes two retro-reflective pieces of tape to reference the distance during a testing event.

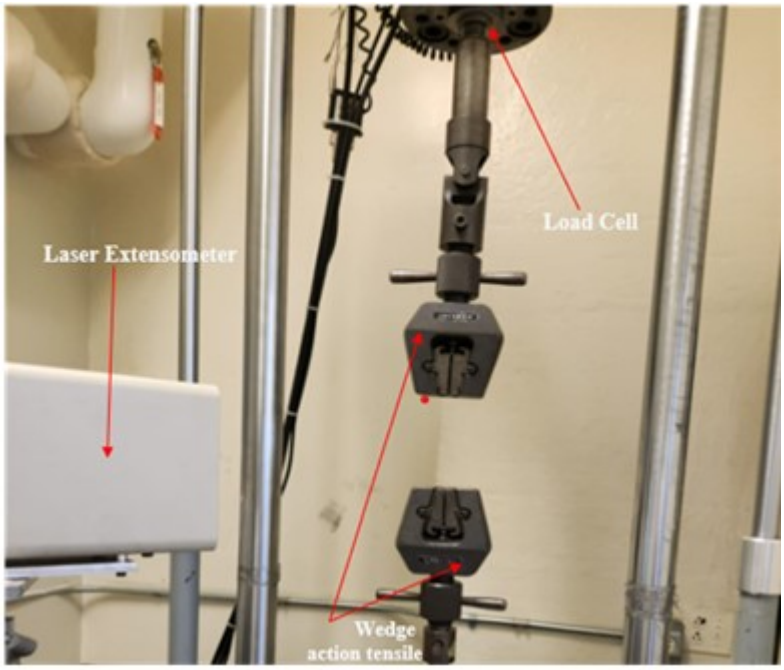

(a)

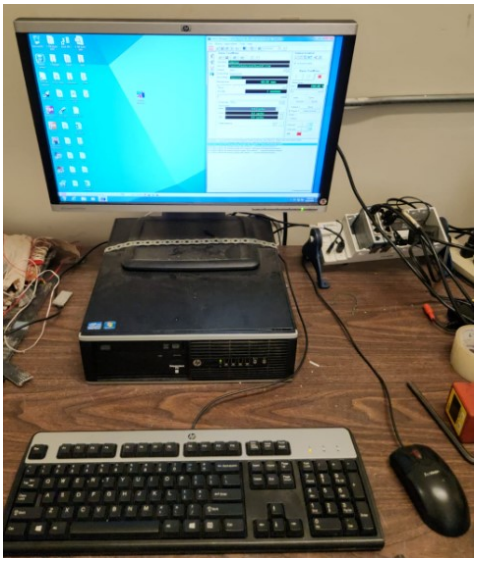

(b)

Figure 5-3 The MTS system with (a) its tensile test setup, (b) its digital user interface system

The compression specimens are restrained by a special fixture as per ASTM D3410 [53]. The test fixture (referred to as Combined Loading Compression fixture (CLC)), and the test setup is illustrated in Figure 5-4.

(a)

(b)

Figure 5-4: (a) Compression Test Setup, (b) Combined Loading Compression (CLC) Fixture

5.3.2. Test procedures

The testing procedures for the tensile and shear tests utilize the same procedures with very little variation. These procedures were carried out following the ASTM D3039 and D3518 [52,54]. The process starts with the initiation and startup of the required systems. The procedure uses the MTS user interface as seen in Figure 5-3 (b) where the various experimental parameters are inputted. Once that process is completed the hydraulic pumps are started and the emergency cutoff valve is opened. The WATG fixture is then attached to the hydraulic arms and the jig is positioned in the MTS machine as seen in Figure 5-3 (a). The laser extensometer is placed into the position and levelled. Next, the specimen is prepared by placing the retroreflective tape in the required configuration. The specimen is then placed into the tensile grips and the grips are tightened. Once these steps are completed the test is initiated and proceeds until specimen failure is accomplished. At this stage, the machine is stopped, and the file is saved. The specimen is then removed and replaced, and the process is repeated.

Once the data is processed, Equation 5-4 to Equation 5-7 found in ASTM D3039, D3410, and D3518 are used to calculate the tensile stress, tensile chord modulus of elasticity, shear stress and shear chord modulus of elasticity, respectively [52,53,54].

$$\sigma_i = \frac{P_i}{A} \qquad \textit{Equation 5-4}$$

$$E^{chord} = \frac{\Delta\sigma}{\Delta\varepsilon} \qquad \textit{Equation 5-5}$$

$$\tau_{12i} = \frac{P_i}{2A} \qquad \textit{Equation 5-6}$$

$$G_{12}{}^{chord} = \frac{\Delta\tau_{12}}{\Delta\gamma_{12}} \qquad \textit{Equation 5-7}$$

In the above equations σ_i is the tensile or compressive stress at the i^{th} data point, P_i is the applied load at the i^{th} data point, A is the cross-section area of the specimen, E^{chord} is the tensile or compressive chord modulus of elasticity, $\Delta\sigma$ and $\Delta\varepsilon$ are the differences in stress and strain values over the elastic region, respectively. Moreover, τ_{12i} is the in-plane shear stress at the i data point, P_i is the load at the i^{th} data point, $G_{12}{}^{chord}$ is the shear chord modulus of elasticity, $\Delta\tau_{12}$ is the difference in shear stress values over the elastic region, and $\Delta\gamma_{12}$ is the difference in shear strain values over the elastic region.

The compression test is conducted following ASTM D3410 [53]. A reflective tape-equipped specimen in the required configuration is sandwiched in the compression fixture, with the bolts of the fixture tightened with the torque magnitude as specified by ASTM D3410 [53]. The compression fixture is then loaded onto the testing machine and the system is configured. Next, the test is started, and the specimen is subjected to axial load until failure (i.e., when the recorded load on the MTS screen is dropped). At this stage, the test is stopped, and the data file is saved. The specimen is removed and replaced, and the process is repeated. Once the test is finished, the compressive stress and the compressive chord modulus of elasticity are calculated using Equation 5-4 and Equation 5-5, respectively.

5.4. Low-Velocity Impact

5.4.1. Equipment and Setup

The experimental setup for the LVI test implements a modified Charpy impactor. The impactor arm is manually raised to the desired angle that is pre-calibrated to the required energy level. Once the arm is at the desired angle, the brake lever at the pivot is engaged holding the arm in place. Once the brake is released the arm swings forward impacting the impactor contact point on the linear impactor propulsion guide. The linear impactor propulsion guide is a jig consisting of a series of roller bearings that restricts the impactor travel in all degrees of freedom except for translation in the direction of impact. It is positioned so that the linear direction extending from the arc of the impactor at the point of contact forms a tangent line.

The impactor tip used in this experiment is a hemispherical impactor with the whole impactor assembly having a mass of 5.822 Kg. The deformation measuring device implemented for the low-velocity setup is a dynamic linear variable differential transformer (DLVDT). The obtained values of deformation or displacement versus load are collected and analyzed showing the indentation depth in the specimen. The force response of the impact event is measured using a Dytran 1060 dynamic load cell this load cell is placed before the impactor so that during an event the compression force of the impact is measured. The Signal from the DLVDT and the load cell is processed using LabVIEW and the final data is saved into a text file. The specimen holder is constructed of two steel plates that clamp the specimen with a circular opening to restrain the specimen during the impact,

which is bolted rigidly to the main rigid platform. The setup detail can be seen in Figure 5-5.

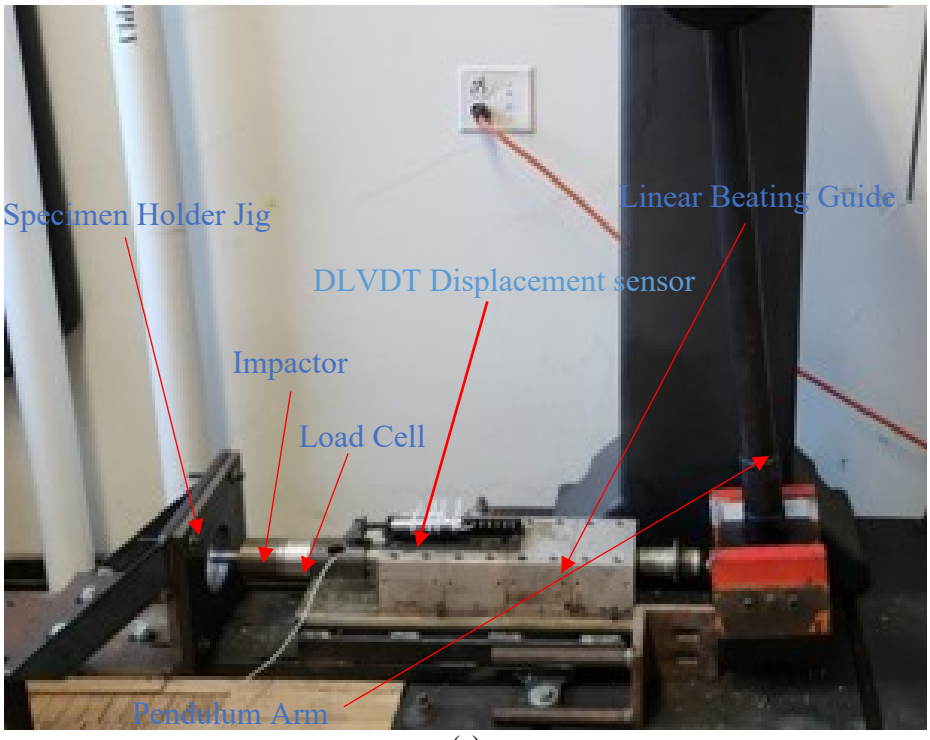

(a)

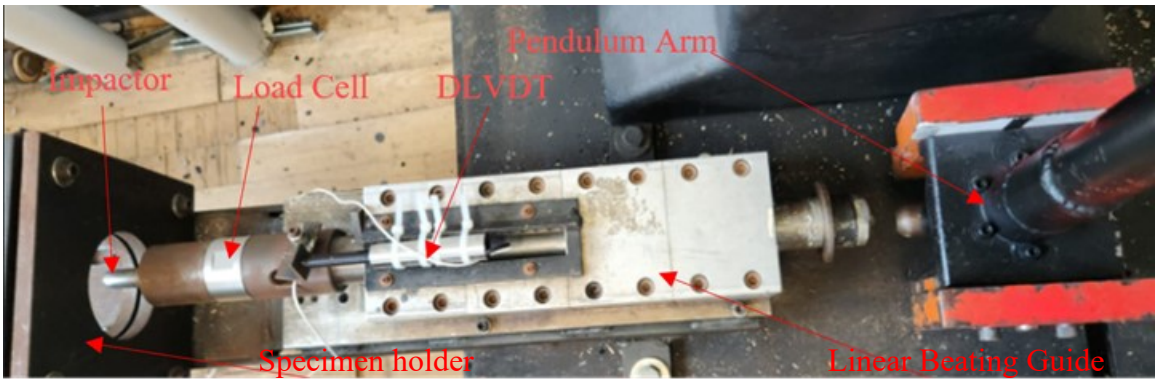

(b)

Figure 5-5 Low-Velocity Impact Test Setup (a) front view; (b) top view

To ensure that each specimen is restrained in a uniform axisymmetric fashion, the specimen holding jig was made to have a circular opening with a diameter of 80 mm instead

of a square opening. A circular opening facilitates even to restrain, thus, even stress distribution at the boundaries by the holder.

5.4.2. Calibration of the equipment

The calibration procedure for the LVI testing equipment was carried out by Wang and Taheri [57]. This process involves measuring the velocity before impact for a set of tests and then determining the constants of the following equation using a linear least-square fit plot [57]. Where E is the kinetic energy, m is the mass of the impactor, v is the velocity at the point of impact, θ is the angle of the impactor at its max elevation, and c_1 and c_2 are the constants of proportionality.

$$E = \frac{1}{2}mv^2 = c_1(1 - cos(\theta)) + c_2 \qquad \textit{Equation 5-8}$$

The process of calibrating the HVI involved first the optimization of the sabot and the selection of a projectile size, shape, and mass. This configuration is then propelled from the gas gun using a range and incremental increasing pressure. A pressure incrementation of 103 kPa was used within a range of 103-824 kPa gauge pressure and 5 trials were done per increment of pressure increase. The results were then averaged and checked for statistical significance by considering the standard deviation. The averages were then plotted, and a linear least-square fit plot was used to determine the characteristic equation of the configuration. As mentioned previously, the calibration results of the gas gun along with the sabot optimization results are presented in the following chapters. The MTS Testing system was calibrated and certified by the manufacturer.

5.4.3. Test procedure

To start the experiment, first, the data acquisition software should be started, and all files named, and the required scopes opened. Next, the specimen is loaded and centred into the holding jig. Once that is done, the linear impactor is reset into the aft position to facilitate contact with the pendulum. The pendulum arm is then raised and locked to the required angle as outlined in the characteristic equation for the selected energy level. At this stage, the data accusation recording is started. After a few seconds, the software confirms the recording, after which the pendulum arm is unlocked, and the impact event is initiated. The software is then stopped, the data file saved, the specimen's visual damage response recorded, and then the specimen is replaced for the next test. The steps are then repeated until all tests are completed.

5.5. High-Velocity Impact

5.5.1. Equipment and Setup

The experimental setup for the HVI test utilizes a compressed air gas gun, designed and developed in-house. The gas gun is loaded with the test projectile through the breach located at the rear of the barrel of the gun, which has a diameter of approximately 25 mm. The operation of the propelling mechanism is automated through the use of an Arduino digital microcontroller. There are two buttons on the user interface the first button arms the system while the second engages the propelling mechanism. The projectiles are propelled using an electro-mechanical solenoid valve that is closed when uncharged but opens once charged. The propellant used in this experiment was compressed air as the maximum

values of energy required could be obtained with that propellant selection.

The projectile used in this experiment is a 9.53 mm diameter solid stainless-steel ball and was selected based on its use outlined by Reid and Zhou [27]. The projectile was attached to a sabot to facilitate the efficient use of the propellant by maintaining a proper seal with the barrel's internal wall. The sabot is then ejected from the projectile through the use of a sabot arresting system. The shattered sabot arresting system consisted of a muzzle deflector that would engage the projectile release mechanism that was designed into the sabot allowing the projectile to continue forward while the sabot redirected into a catching system. The pressurizing system consists of a pressure tank with a manufacturer-rated maximum pressure of 1.379 MPa (200 psi) and an external pressure reservoir with an electrically powered air pump. Even though the pressure tank has a manufacturer-rated maximum pressure of 200 psi, it is fitted with a safety release valve programmed to actuate at 1.0342 MPa (150 psi).

Given the high velocities the system is capable of, the testing area is encapsulated within a protective shielding system. This system consists of 12 mm thick plexiglass side walls with 5mm thick plexiglass angled top covers. The sacrificial backing panel is composed of plywood panels with a total thickness of 60 mm, as this material gives good stopping capabilities while reducing the chance of a ricochet.

The velocity systems used in this experimental setup are two ballistic chronographs and a digital and analogue pressure gauge. The two chronographs are located before and

after the test specimen. This placement allows for the measurement of the velocities and energies of the projectile before and after an impact event. The precision ballistic chronographs are manufactured by Caldwell and Competition Electronics. They are capable of measuring velocities between 1-3000 m/s with a manufacturer-rated accuracy of ± 0.25% and ± 0.5%, respectively [58,59]. This level of accuracy is achieved through the implementation of 48 MHz processors [58,59]. The specimen dimensions used in the experimental setup are 100 mm X 150 mm as recommended by ASTM D7136 [55]. The specimen-holding device consists of two plates that sandwich the test specimen. The holding jig is then bolted rigidly to the testing platform. The testing setup is shown in Figure 5-7. The calibration results of the gas gun along with the sabot optimization results are presented in the following chapter. The energy of the projectile is calculated using Equation 5-9 and the absorbed energy is calculated using Equation 5-10.

$$E = \frac{1}{2}mv^2 \qquad \textit{Equation 5-9}$$

$$E_A = \frac{1}{2}mv^2{}_I - \frac{1}{2}mv^2{}_R \qquad \textit{Equation 5-10}$$

where v = velocity of the projectile, m = mass of the projectile, v_I and v_R are the incident and residual velocities, respectively.

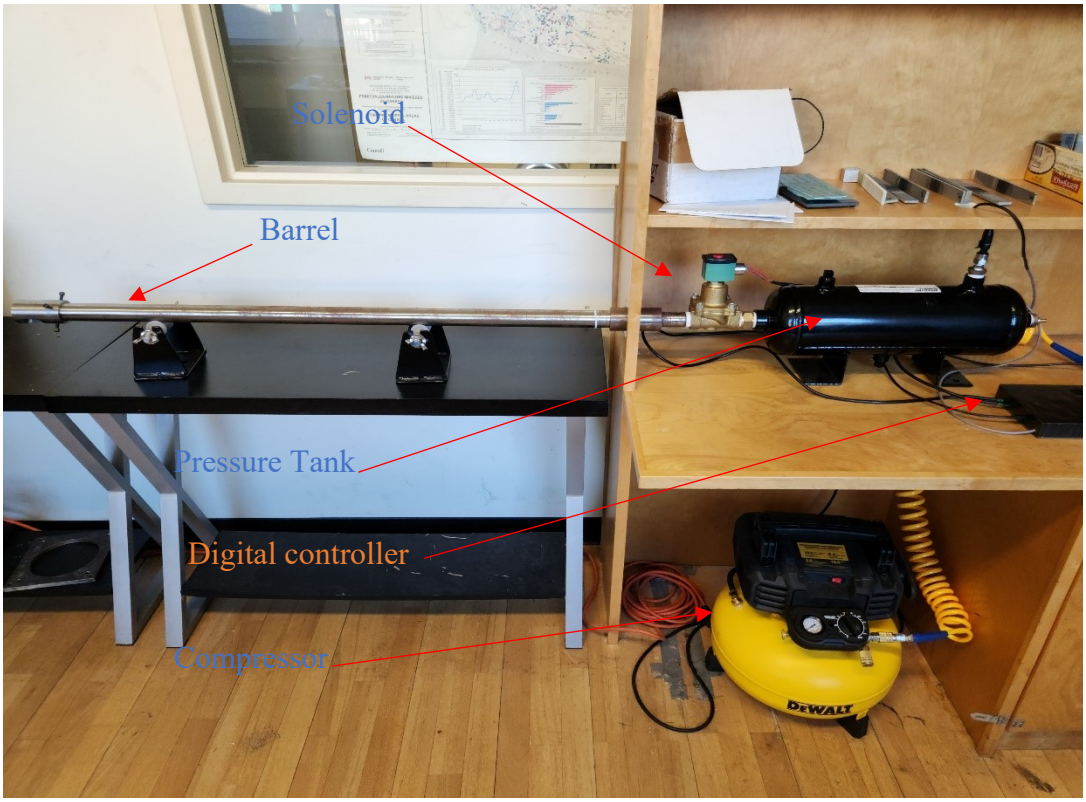

Figure 5-6: The High-velocity Gas Gun

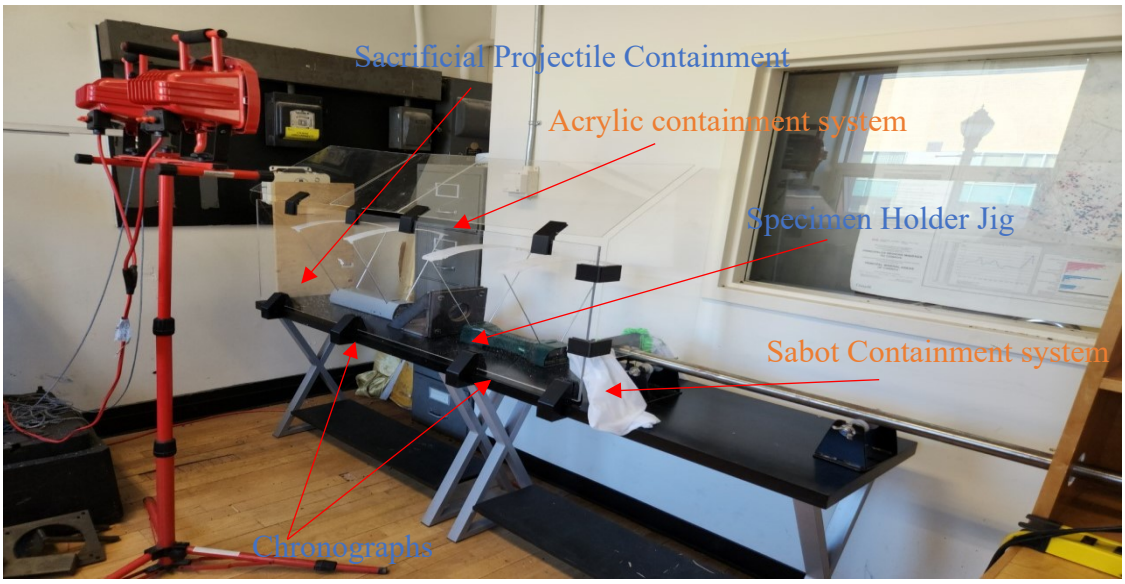

Figure 5-7: Projectile Containment System

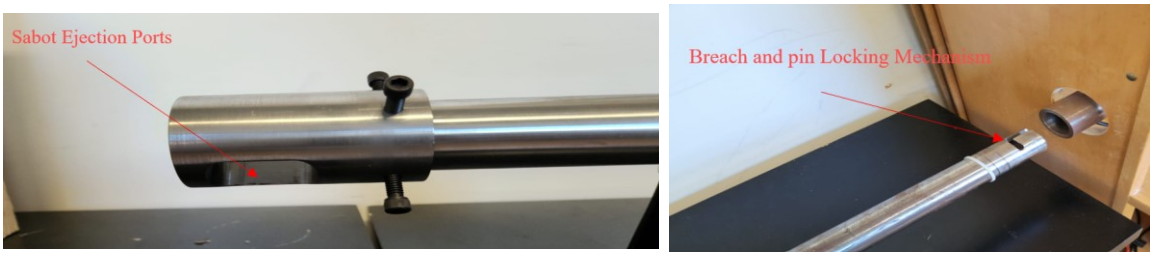

(a) (b)

Figure 5-8: (a) Sabot Arresting System ; (b) Breach Loading Port

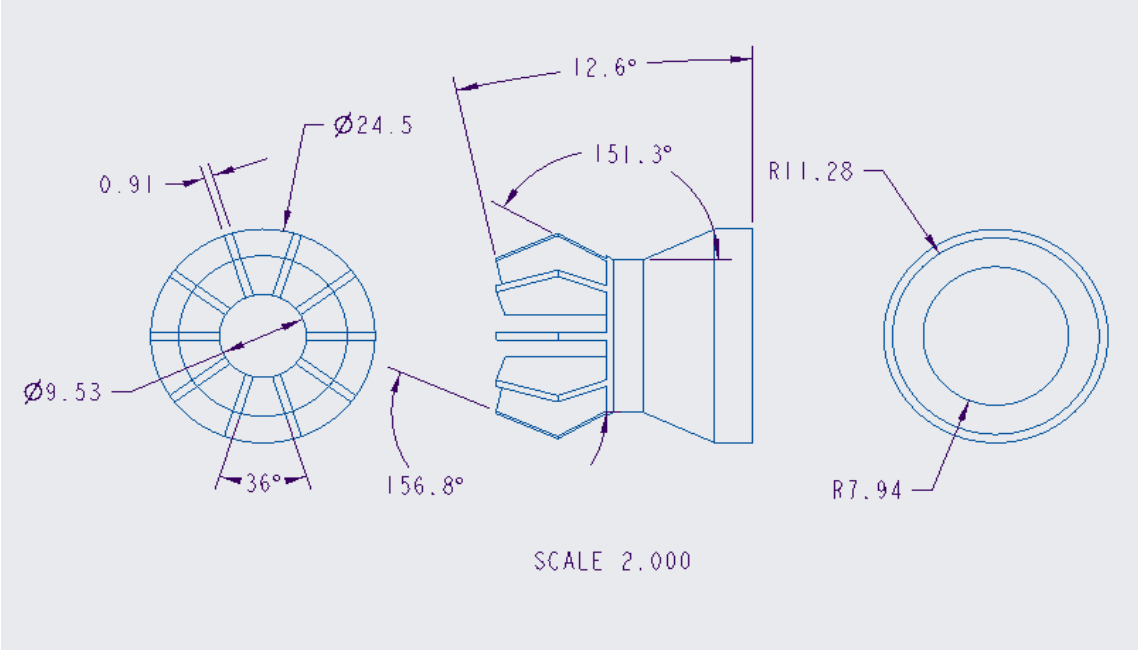

(a)

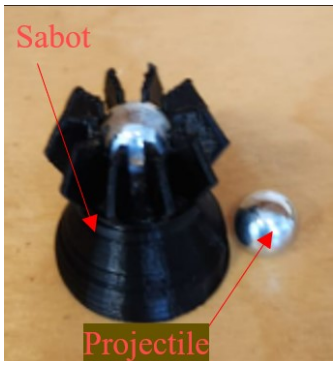

(b)

Figure 5-9: (a) Sabot Design , (b) 3D-printed Sabot with a projectile

5.5.2. Test procedure

The HVI tests were done in accordance with the US Army Research Laboratory's guidelines [10]. This method is called the v_{50} method and is based on the principle that there exists a function that describes the behaviour of the projectile after impact and penetration [10]. This function is continuous and differentiable; therefore, there exists a

point on that function which is the ballistic limit [10]. First, a range velocity is selected which should include the limit velocity. For this experiment, given that the range of the gas gun propellant speed is somewhat limited, the entire velocity range of the gas gun was selected. The specimen is placed and centred into the holding jig. Next, the chronograph, control computer, and air pump are turned on. The breach is then opened and the projectile holding sabot is loaded and the breach is closed. Then the required pressure for the velocity is established in the main air tank. Once ready to conduct the experiment the arming button is pressed and then the firing button. There is a 3-second delay between when the propellant button is pressed to when the sabot is propelled. The velocity of the projectile is picked up by the chronographs and recorded. Subsequently, the impacted specimen is replaced by the next virgin specimen. If penetration is achieved, then the range is halved, and the process is repeated until the ballistic limit is reached. According to the document, this method can accurately obtain the ballistic limit with a tolerance of 1 m/s with an average of 5.5 impact events [10].

Chapter 6: Results and Discussion

6.1. Overview

This chapter covers the results and discussion of the research employed in this thesis. The set-up calibration results presented are the sabot selection and the gas gun calibration. Followed by the experimental results of the material properties which include density and void content, tensile, shear, and compression. Lastly, the characterization results of the low and HVI experiments are presented.

6.2. Pre-Processing

6.2.1. Sabot Selection

For the sabot selection, 5 different designs were tested for the highest projectile kinetic energy. The sabots were printed on a 3D printer with the same printer and material used for each print. The 5 designs are outlined in Figure 6-1, Figure 6-2, Figure 6-3, Figure 6-4, and Figure 6-5. The sample size for each design was five. For the test, the pressure was held constant at 689.48 kPa. The Results of this test are outlined in Table 6-1 and Figure 6-6.

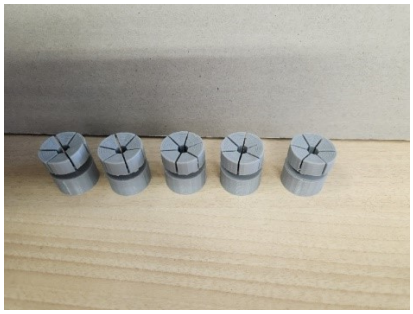

Figure 6-1:Sabot #1 design

The sabot #1 design as seen in Figure 6-1 was configured to optimize the projectile release mechanism by incorporating an inclined plane and undercutting in the projectile holding leaflets. The projectile release mechanism involves an inclined recess that produces a bending moment upon impact that releases the projectile. This mechanism reduces the chance of a projectile sabot interaction.

Figure 6-2:Sabot #2 design

Sabot # 2 as seen in Figure 6-2 was configured to include the features of sabot #1 but with a more aerodynamic profile. This profile was done with the intent of increasing the ultimate velocity.

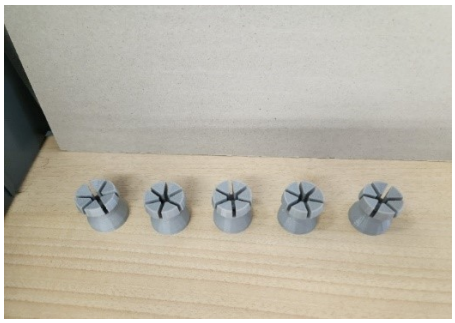

Figure 6-3:Sabot #3 design

The design of sabot #3 as seen in Figure 6-3 incorporated a weight reduction through the removal of 1.6 grams of excess material while including the features of design #1 and #2.

Figure 6-4:Sabot #4 design

Sabot #4 as seen in Figure 6-4 design incorporated an even higher reduction in weight of 2.7 grams and an increased aerodynamic profile. This was done while also retaining the projectile release mechanism seen in the design of sabot # 1.

Figure 6-5:Sabot #5 design

Lastly, sabot design #5 as seen in Figure 6-5 was designed to optimize the sabot release mechanism by incorporating a larger angle to the inclined plane while incorporating the features of sabot # 4.

Table 6-1: Sabot test results

Sabot Number	Kinetic Energy Average (J)	Std Dev	Coeff. var.
1	38.65	1.63	4.20
2	49.56	1.71	3.45
3	55.64	1.45	2.60
4	57.31	2.34	4.08
5	54.99	2.28	4.14

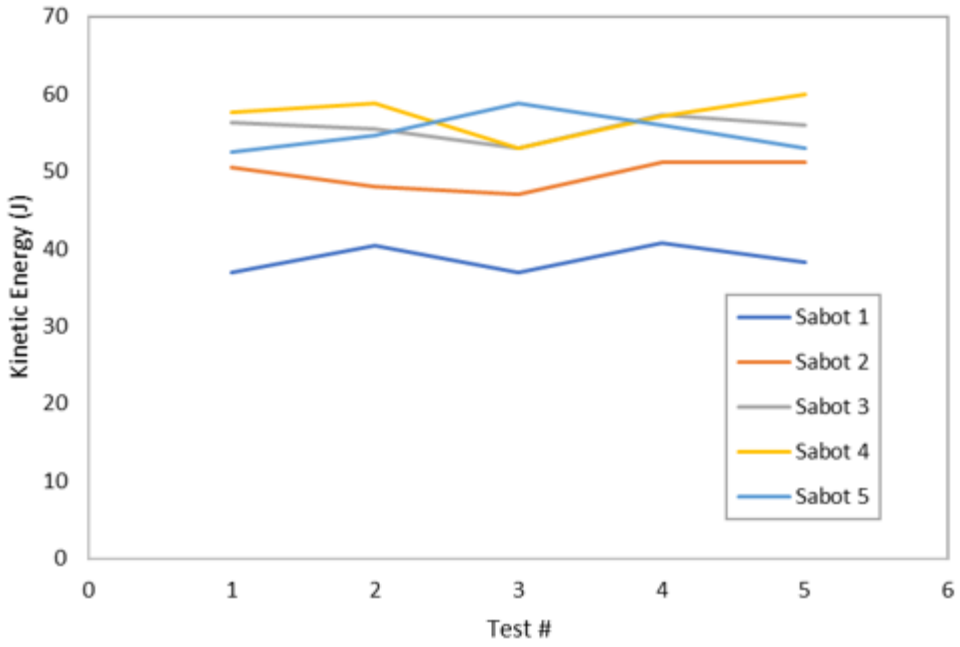

Figure 6-6: Sabot test results plot

The Results of the sabot tests as seen in Table 6-1 showed that sabot design # 4 gave the highest projectile kinetic energy. Sabots starting from design # 1 to # 5 (see appendix A) see a reduction in the weight of the sabot with #4 and #5 having almost similar weights. The coefficient of variance for values of the average kinetic energy seen in Table 6-1 all falls below 5% with the highest value of 4.20%. The mass of the projectile and sabot are comparable with the projectile at times weighing more than the sabot. The mass of the projectile had a small fluctuation since the projectile used for the sabot testing was constructed in-house with a steel cut rod. Since this variation in the projectile mass exists, the kinetic energy is used to verify the validity of the sabot design.

6.2.2. Gas Gun Calibration

The calibration of the gas gun was carried out with the selected sabot which weighed 2.54g and a 9.53 mm spherical steel ball weighing 3.5 g. The test sample size was 5 specimens per pressure increment. The pressure increment was 103.42 kPa and was increased to 827.37 kPa. The results of this experiment are outlined in Figure 6-7, Figure 6-8, and Table 6-2. The data collected is presented in Appendix A. While the characteristic equation is outlined in Equation 6-1.

Table 6-2: Gas gun calibration test results

Pressure (kPa)	Kinetic Energy (J)	Velocity avg (m/s)	Projectile Energy (J)	Standard Dev of Velocity	Coeff. var. of Velocity
103.42	22.04	85.00	12.64	0.00	0.00
206.84	46.14	123.00	26.48	0.63	0.51
310.26	67.17	148.40	38.54	0.49	0.33
413.69	81.43	163.40	46.72	1.50	0.92
517.11	95.77	177.20	54.95	0.40	0.23
620.53	101.03	182.00	57.97	2.19	1.20
723.95	108.95	189.00	62.51	1.26	0.67
827.37	108.49	188.60	62.25	1.02	0.54

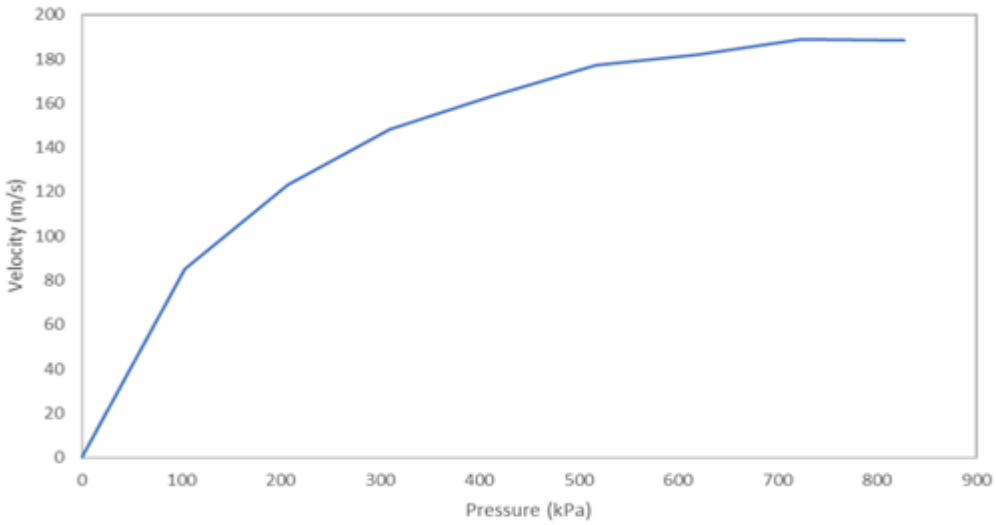

Figure 6-7: Gas gun calibration plot of pressure vs. velocity

The trend of the plot seen in Figure 6-7 shows an almost asymptotic profile as the pressure increases. This trace shows that the gas gun is more efficient at lower pressures since friction and pressure losses will become greater at higher pressures.

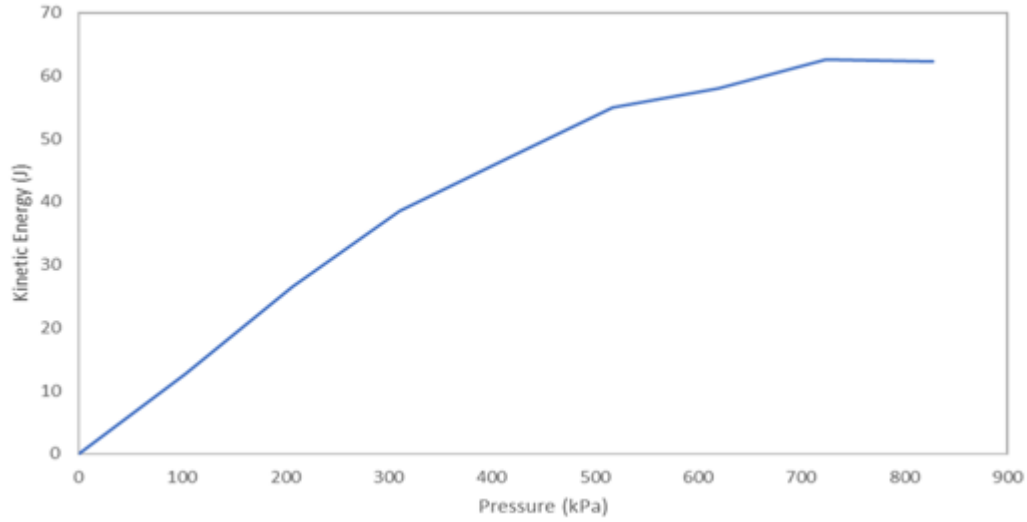

Figure 6-8: Gas gun calibration plot of pressure vs. projectile kinetic energy

$$V = 3E\text{-}07P^3 - 0.0006P^2 + 0.5257P + 37.886 \qquad \textit{Equation 6-1}$$

A consistent velocity-to-pressure correlation was obtained from gas gun calibration tests as seen in Equation 6-1. The characteristic equation was obtained using a linear least square approximation. Which have an R-value of 0.9986 for the pressure vs. velocity relationship. The R-values indicate a strong fit between the data and the equations obtained. The variation in the measured velocities obtained from the test is small with all values of the coefficient of variation falling below 2% as seen in Table 6-2. The coefficient of variation shows an increase with an increase in pressure and velocity up to 620.53 kPa then decreases with a further increase. This behaviour can be due to a form of Helmholtz harmonic resonance that happens between the flow and the barrel assembly as the flow velocity is increased. At the lower velocities, the variance decreases significantly. At the value of 85 m/s, the variance is smaller than the measuring equipment can detect.

6.3. Basic Material and Mechanical Properties

6.3.1. Density and Void Content Results

The density experimentation was carried out for all the fabrics (i.e., basalt, Kevlar 29, and E-glass). The densities of the composites composed of the fibers mentioned previously along with both Elium and epoxy resins were also obtained. Then using the burn-off test, the fibre and resin weight percentages were obtained. Lastly, the void content of the tested composites was established. All procedures were carried out following ASTM D2734-16 [56]. The results can be viewed below.

Table 6-3: Density and void content of the composites

Material	Average Density (g/ml)	Theoretical density (g/ml)	Void content %
E-glass epoxy	1.49	1.56	4.68
E-glass Elium	1.35	1.45	7.04
Basalt epoxy	1.59	1.70	6.54
Basalt Elium	1.49	1.58	5.51
Kevlar-29 epoxy	1.24	1.29	4.19
Kevlar-29 Elium	1.15	1.23	6.42

Table 6-4: Average fiber density

Kevlar-29	Basalt	E-glass
1.43 g/ml	2.70 g/ml	2.44 g/ml

Table 6-5: Average fiber weight percentage and volume fraction

Material	Average Fiber weight%	Average Resin weight%	Average fiber volume fraction	Average resin volume fraction
E-glass epoxy	47.4	52.6	0.29	0.66
E-glass Elium	51.6	48.4	0.29	0.64
Basalt epoxy	54.3	45.7	0.32	0.61
Basalt Elium	57.6	42.4	0.32	0.63
Kevlar epoxy	49.3	50.7	0.43	0.53
Kevlar Elium	60.7	39.3	0.49	0.45

These results were then used to obtain the void content of the composites. All void contents fall below 8% of the total volume of the composites with the E-glass Elium having the highest void content and the Kevlar-29 epoxy having the lowest. The epoxy composite specimens (except for basalt epoxy) have a lower void content than their Elium counterparts with the basalt epoxy being comparable to basalt Elium. This is partially due

to the increased outgassing caused by the rapid increase in temperature caused by the cross-linking of Elium leading the resin to approach its boiling point. The fiber resin weight percentage as seen in Table 6-5 of all the specimens is similar in value, with Kevlar-29 Elium having the highest fiber weight percentage. The resin occupies most of the volume of a composite because it has the lower density of the two and the composite is manufactured with an approximately 1:1 resin to fiber weight ratio. This ratio is observed with all specimens except with the Kevlar-29 Elium where the fibre volume is larger than the resin. The Kevlar-29 fibres are closer in density to the resin therefore this increase in fibre volume with a decrease in fibre density is expected.

6.3.2. Tensile Test Results

As mentioned earlier, the tensile tests were performed following ASTM D3039 [17] on all composite specimens, with five specimens per composite. The measurements of width, length, and thickness were taken at three different points each and the average was recorded.

Table 6-6: Average strength and modulus of elasticity of the test specimens

E-glass epoxy		
Avg Max Tensile Stress (MPa)	Standard Deviation	Coeff. var
301.5	23.39	7.76
Average Tensile Cord Modulus (MPa)	Standard Deviation	Coeff. var.
11072.68	647.77	5.85
E-glass Elium		
Avg Max Tensile Stress (MPa)	Standard Deviation	Coeff. var.
304.9	2.34	0.77
Average Tensile Cord Modulus (MPa)	Standard Deviation	Coeff. var.
12424.42	475.64	3.83
Basalt epoxy		
Avg Max Tensile Stress (MPa)	Standard Deviation	Coeff. var.
298.5	18.12	6.07
Average Tensile Cord Modulus (MPa)	Standard Deviation	Coeff. var.
13854.28	725.13	5.23
Basalt Elium		
Avg Max Tensile Stress (MPa)	Standard Deviation	Coeff. var.
386.8	35.33	9.14
Average Tensile Cord Modulus (MPa)	Standard Deviation	Coeff. var.
16566.94	996.33	6.01
Kevlar-29 epoxy		
Avg Max Tensile Stress (MPa)	Standard Deviation	Coeff. var.
463.2	11.40	2.46
Average Tensile Cord Modulus (MPa)	Standard Deviation	Coeff. var.
27838.57	775.03	2.78
Kevlar-29 Elium		
Avg Max Tensile Stress (MPa)	Standard Deviation	Coeff. var.
641.6	9.80	1.53
Average Tensile Cord Modulus (MPa)	Standard Deviation	Coeff. var.
35044.96	894.66	2.55

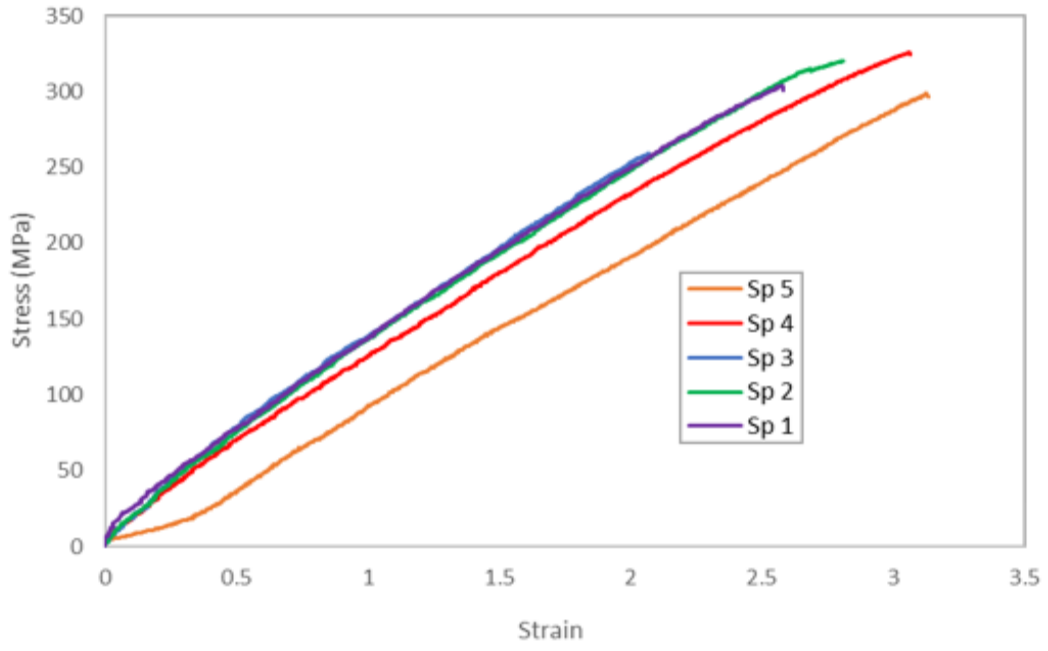

Figure 6-9: Plot of tensile stress vs. strain curves of E-glass epoxy specimens

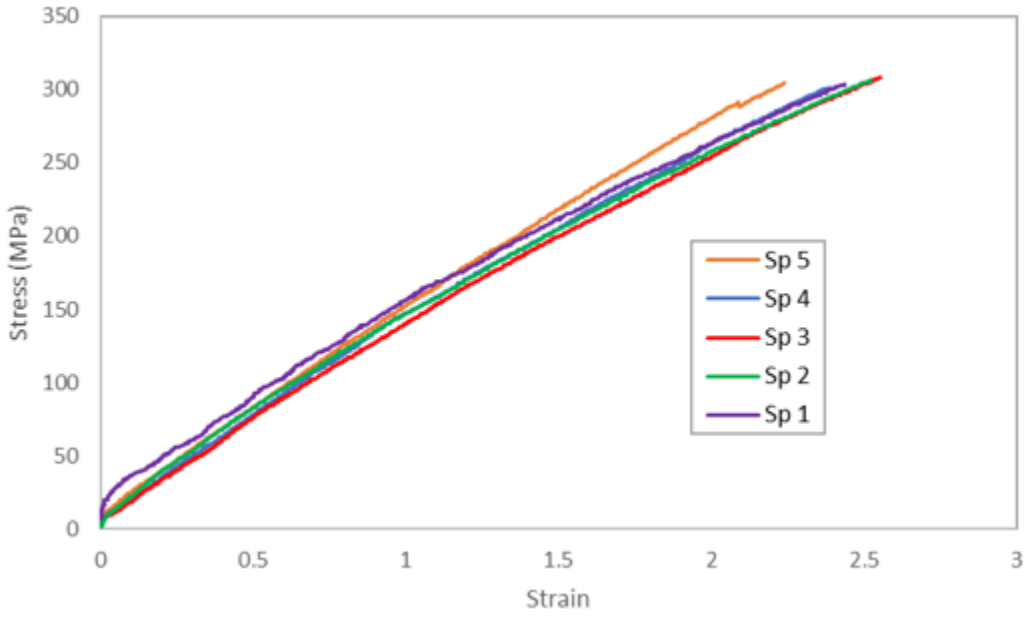

Figure 6-10: Plot of tensile stress vs. strain curves of E-glass Elium specimens

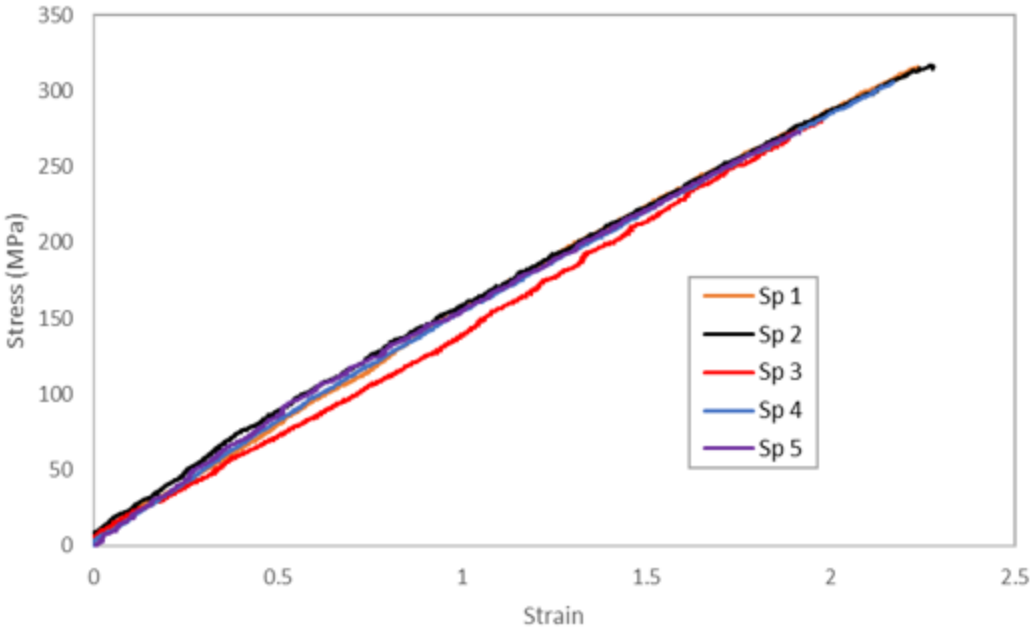

Figure 6-11: Plot of tensile stress vs. strain curves of basalt epoxy specimens

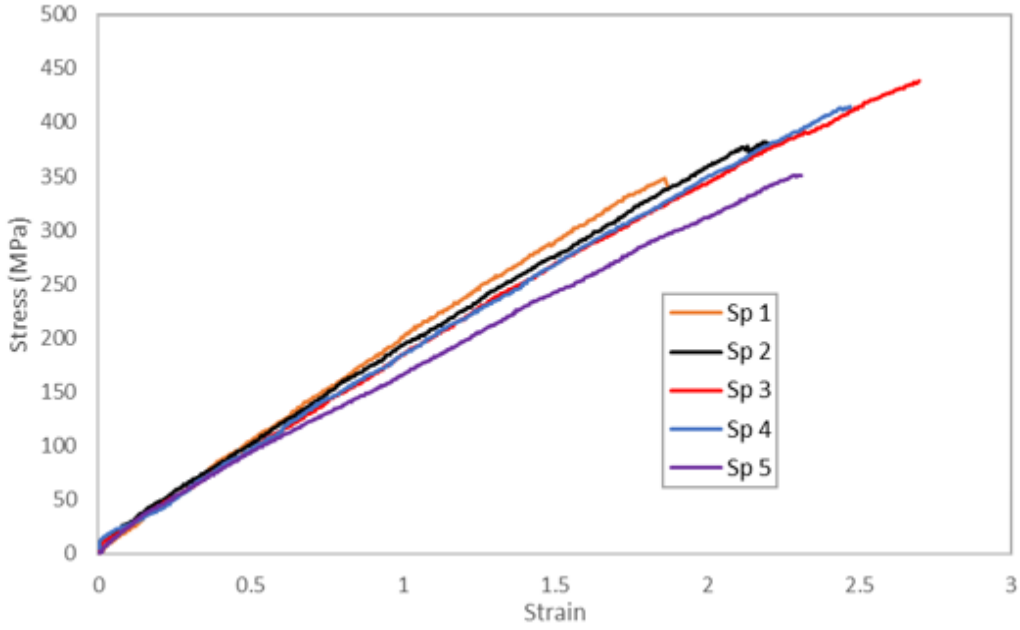

Figure 6-12: Plot of tensile stress vs. strain curves of basalt Elium specimens

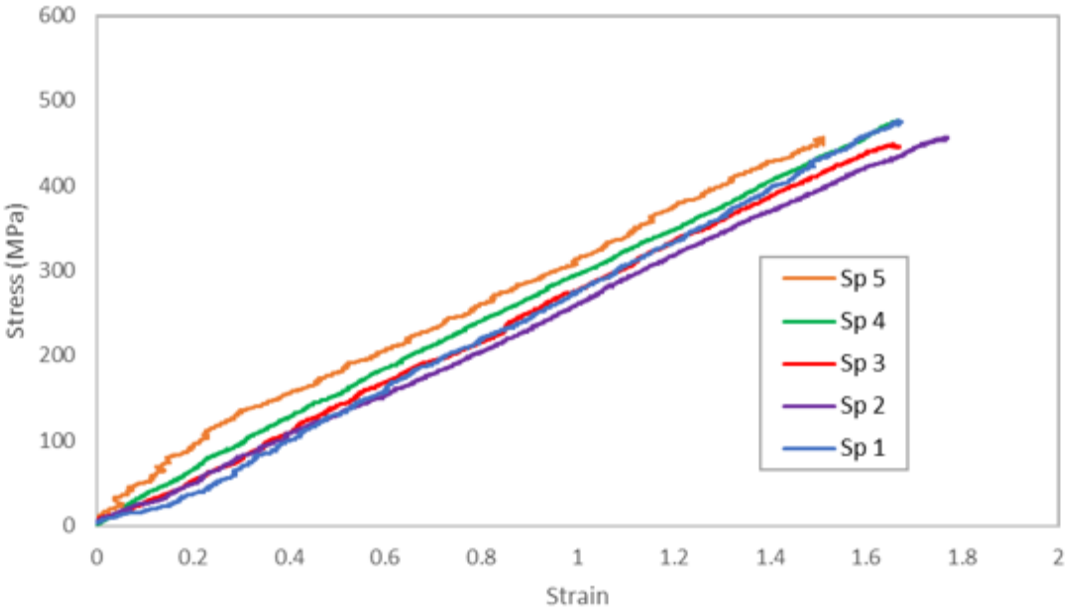

Figure 6-13: Plot of tensile stress vs. strain curves of Kevlar-29 epoxy specimens

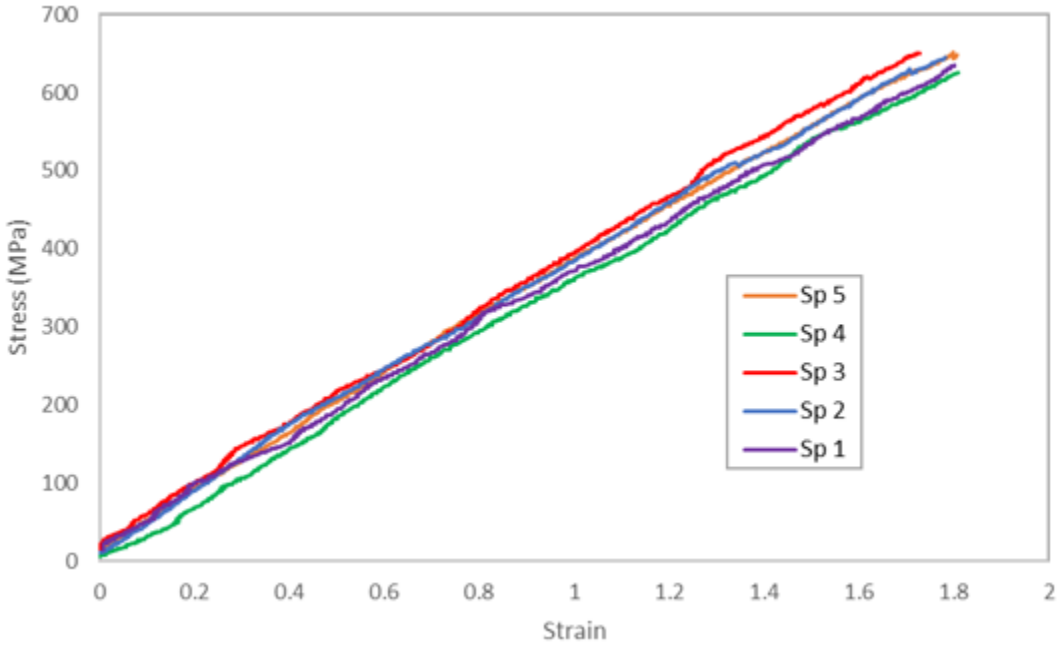

Figure 6-14: Plot of tensile stress vs. strain curves of Kevlar-29 Elium specimens

As seen, the ultimate tensile strength of each Elium composite has a higher value than its epoxy-based counterpart with Kevlar-29 Elium having the highest value of 641.6 MPa. The increase in strength can be explained by looking at the fundamentals of composite mechanics. In composites, the matrix facilitates load transfer among the fibers. In unidirectional fiber-reinforced composites, the fibers primarily take a great majority of the load even if their volume content is low. However, any deviation in fiber angle with respect to the applied load reduces the load bearing of the fibers, at which state the resin contribution comes into action, with the contribution becoming significantly increased as the fiber angle increases. In the case of our specimens, there are also fibers laid in the transverse directions. With consideration of this phenomenon, one should also consider the ductile nature of Elium compared to the rigid and brittle nature of epoxy resins. Any malalignment during the assembly process, which is a function of the stochasticity of the system, and any void content will have graver consequences in a brittle matrix than a ductile one. This effect can also be observed in the materials recorded modulus of elasticity.

6.3.3. Shear Test Results

As also stated earlier, the shear tests were performed as per ASTD D 3518 [54], which is quite similar to the tensile test, except in this test, the specimen fiber orientation consists of +45^{o} and -45^{o}. The fiber orientation is symmetric from the mid-plane. Each test was performed with a sample size of 5 specimens per test. The results of the test are reported below.

Table 6-7: Average shear strength and modulus of test specimens

E-glass epoxy		
Avg Max Shear Stress (MPa)	Standard Deviation	Coeff. var.
47.9	1.78	3.72
Average Shear Cord Modulus (MPa)	Standard Deviation	Coeff. var.
3145.12	198.60	6.31
E-glass Elium		
Avg Max Shear Stress (MPa)	Standard Deviation	Coeff. var.
69.8	1.82	2.61
Average Shear Cord Modulus (MPa)	Standard Deviation	Coeff. var.
4475.86	273.12	6.10
Basalt epoxy		
Avg Max Shear Stress (MPa)	Standard Deviation	Coeff. var.
36.8	1.16	3.15
Average Shear Cord Modulus (MPa)	Standard Deviation	Coeff. var.
2677.89	130.26	4.86
Basalt Elium		
Avg Max Shear Stress (MPa)	Standard Deviation	Coeff. var.
39.9	2.67	6.70
Average Shear Cord Modulus (MPa)	Standard Deviation	Coeff. var.
3365.78	96.87	2.88
Kevlar-29 epoxy		
Avg Max Shear Stress (MPa)	Standard Deviation	Coeff. var.
61.3	2.82	4.61
Average Shear Cord Modulus (MPa)	Standard Deviation	Coeff. var.
4221.63	197.27	4.67
Kevlar-29 Elium		
Avg Max Shear Stress (MPa)	Standard Deviation	Coeff. var.
11.2	0.66	5.85
Average Shear Cord Modulus (MPa)	Standard Deviation	Coeff. var.
1269.08	63.95	5.04

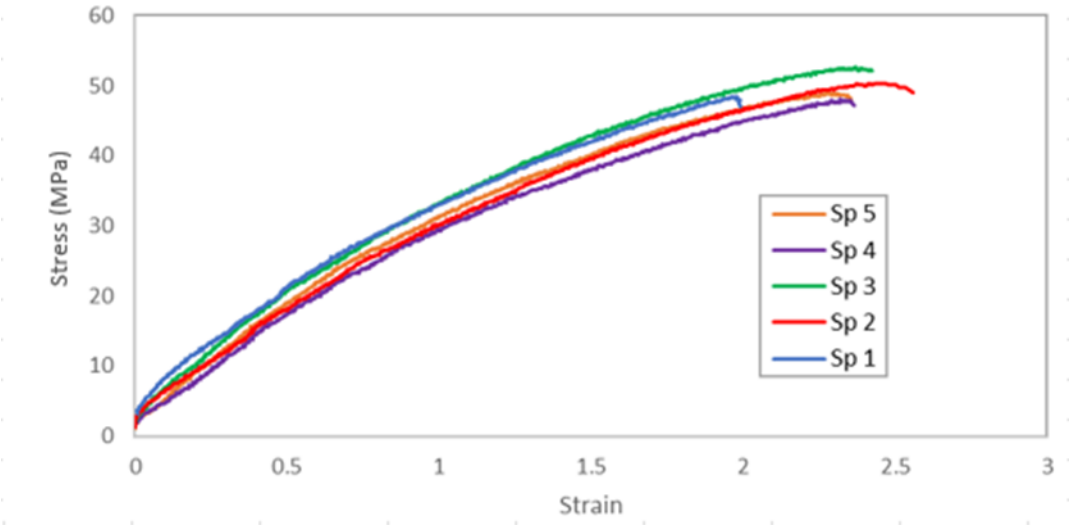

Figure 6-15: Plot of shear stress vs. strain curves of E-glass epoxy specimens

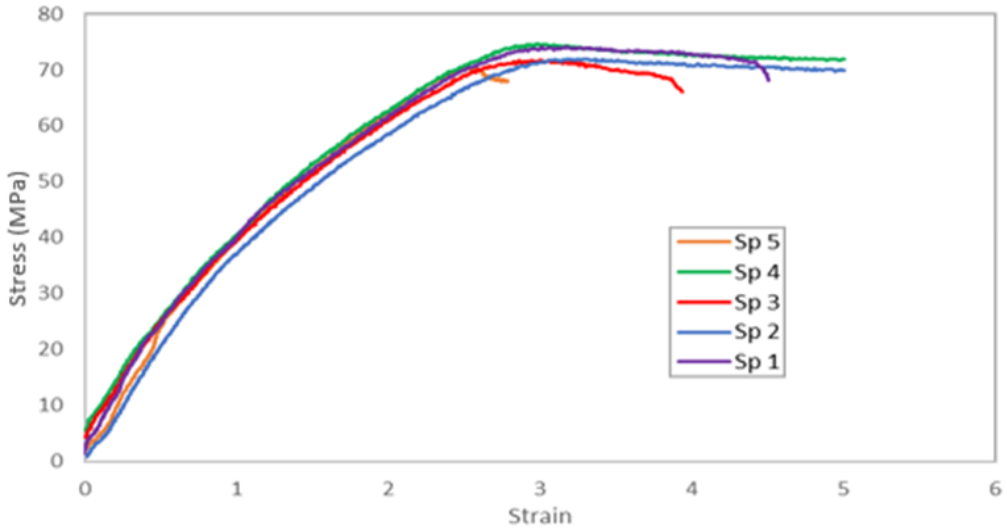

Figure 6-16: Plot of shear stress vs. strain curves of E-glass Elium specimens

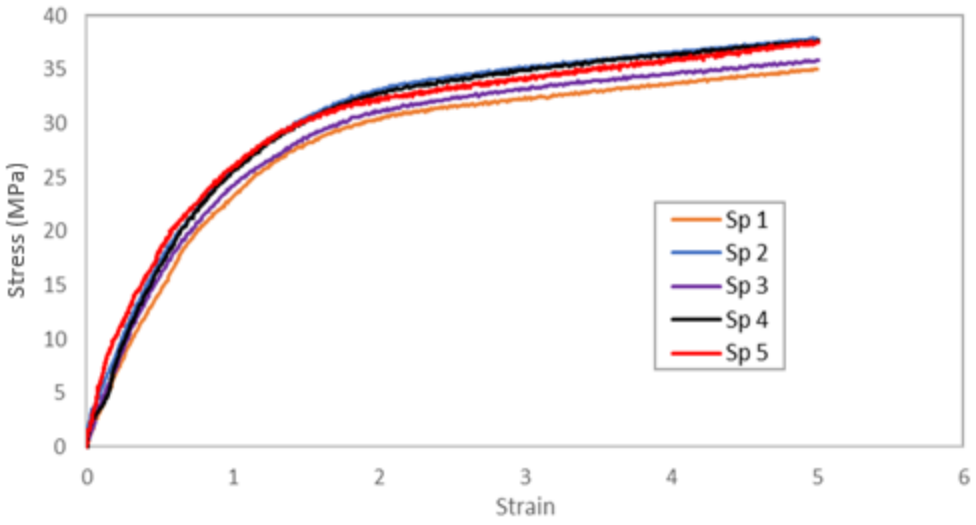

Figure 6-17: Plot of shear stress vs. strain curves of basalt epoxy specimens

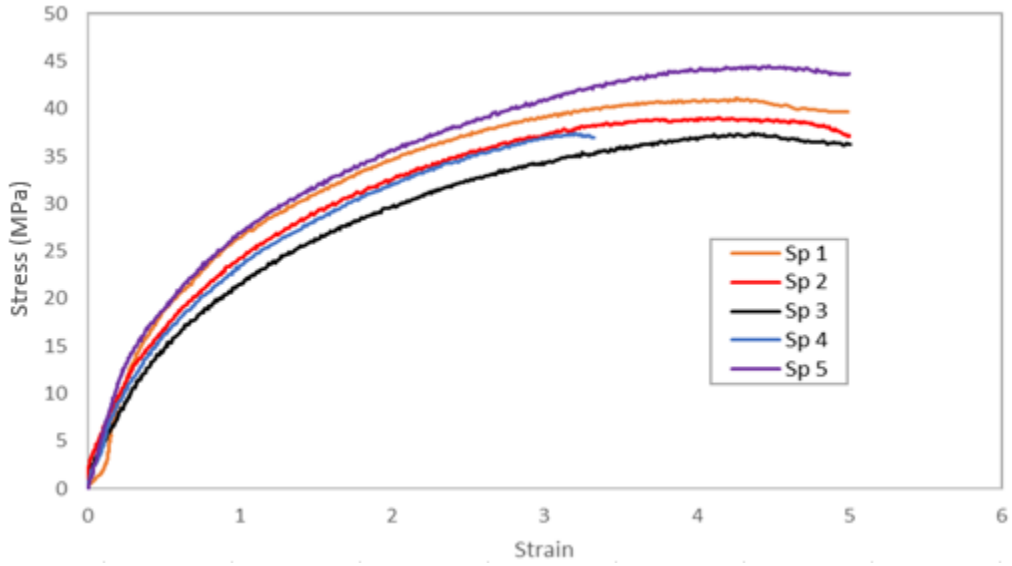

Figure 6-18: Plot of shear stress vs. strain curves of basalt Elium specimens

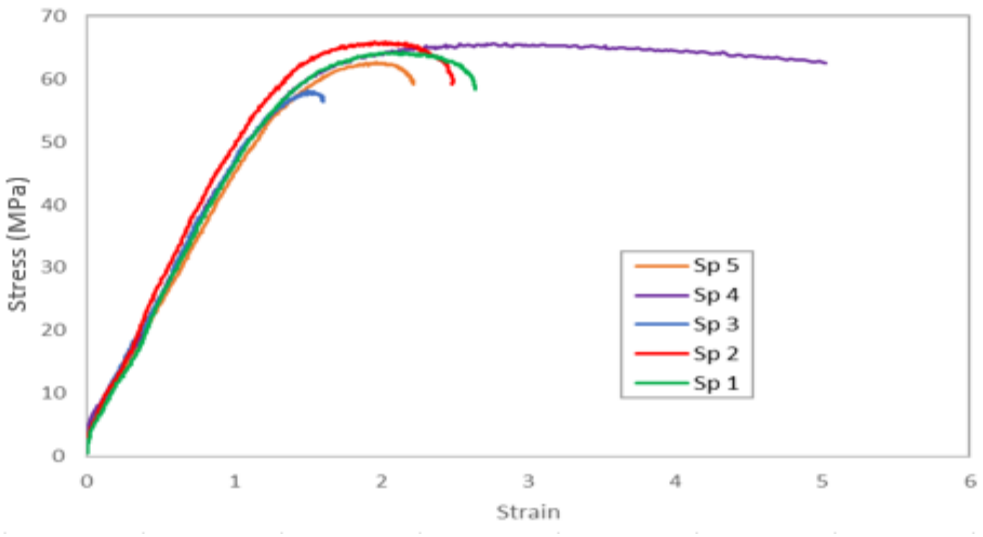

Figure 6-19: Plot of shear stress vs. strain curves of Kevlar-29 epoxy specimens

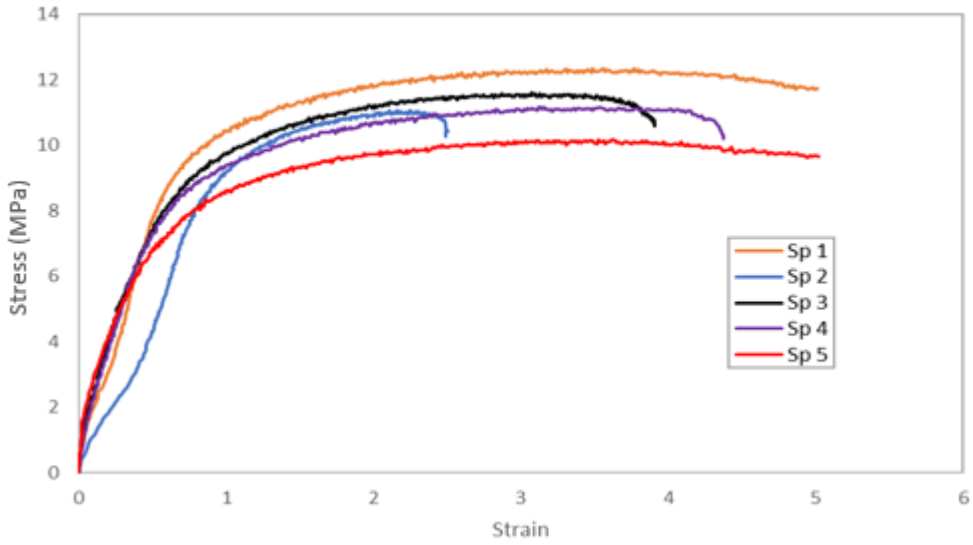

Figure 6-20: Plot of shear stress vs. strain curves of Kevlar-29 Elium specimens

The plots of shear stress vs strain show the characteristic dome shape that is expected as seen in the above six figures. For the basalt and E-glass specimens, the Elium-based matrix exhibited a higher value of the ultimate shear strength (see Table 6-7). The higher ultimate shear strength is due in part to the efficient transfer of load among the fibers that

are accommodated by the matrix. Elium, as mentioned previously, has a more ductile nature leading to greater deformability before failure when compared to the lower ductility of the epoxy resin. Also, the ductile nature reduces the effect of stress concentration which would exhibit a much graver consequence in a brittle matrix. However, the Kevlar-29 Elium did not follow the trend. The reason for this is that the Kevlar-29 fibers are significantly finer than E-glass and basalt fibers. This small fiber diameter combined with the low viscosity of the Elium resin at its liquid state would cause most of the resin to be absorbed within the fibers rather than be between fiber bundles. Given that the in-plane shear strength is a function of the resin matrix, more resin within the fibers and less between the bundles would lead to a decrease in the effective shear strength. This effect was not observed with the basalt and E-glass composites as the fiber size is significantly larger than the Kevlar-29 fibers and is comparatively less absorbent due to their nature. Moreover, the space between fiber bundles for both the E-glass and basalt is significantly larger than the Kevlar-29. Therefore, the smaller space facilitates the resin placement in between the fibre bundles leading to a reversed trend as seen.

6.3.4. Compression Test Results

As stated earlier, ASTM D3410 [53] was followed to carry out the compression tests. A CLC fixture was used to secure the specimen, with 5 specimens tested for each composite. The test specimens were prepared with fiber orientations of $[0,90]_s$. The minimum specimen thickness was 1.55 mm while the gauge length was 15 mm. The results of this test are reported below.

Table 6-8: Average compressive strength and modulus of test specimens

E-glass epoxy		
Avg Max Stress (MPa)	Standard Deviation	Coeff. var.
158.06	10.00	6.32
Average compression Modulus (MPa)	Standard Deviation	Coeff. var.
18262.20	1139.30	6.24
E-glass Elium		
Avg Max Stress (MPa)	Standard Deviation	Coeff. var.
152.4	7.89	5.18
Average compression Modulus (MPa)	Standard Deviation	Coeff. var.
16765.8	1533.99	9.15
Basalt epoxy		
Avg Max Stress (MPa)	Standard Deviation	Coeff. var.
140.3	8.52	6.07
Average compression Modulus (MPa)	Standard Deviation	Coeff. var.
19773.2	832.45	4.21
Basalt Elium		
Avg Max Stress (MPa)	Standard Deviation	Coeff. var.
106.1	10.21	9.63
Average compression Modulus (MPa)	Standard Deviation	Coeff. var.
17585	1465.07	9.90
Kevlar-29 epoxy		
Avg Max Stress (MPa)	Standard Deviation	Coeff. var.
51.4	4.90	9.53
Average compression Modulus (MPa)	Standard Deviation	Coeff. var.
14982.4	1417.24	9.46
Kevlar-29 Elium		
Avg Max Stress (MPa)	Standard Deviation	Coeff. var.
68.9	5.21	7.44
Average compression Modulus (MPa)	Standard Deviation	Coeff. var.
23041.8	2108.031	9.15

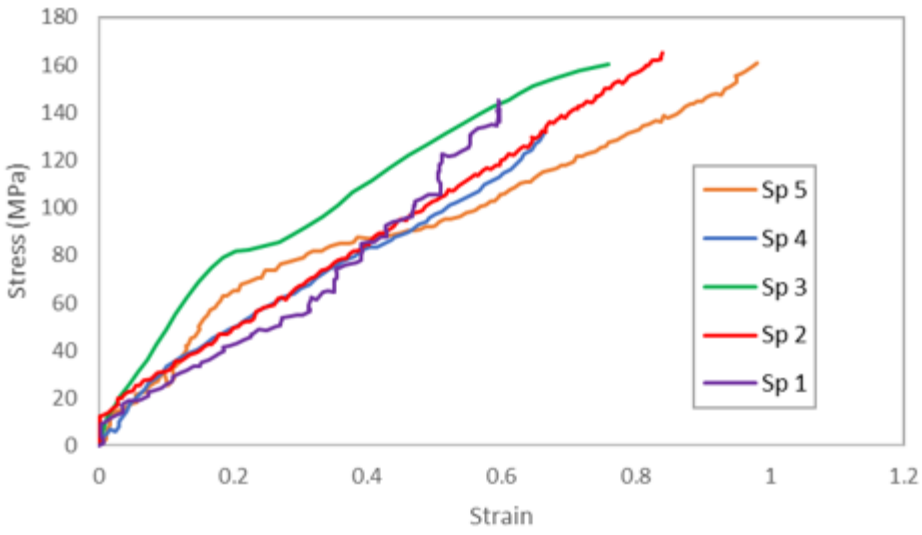

Figure 6-21: Plot of compressive stress vs. strain E-glass epoxy specimens

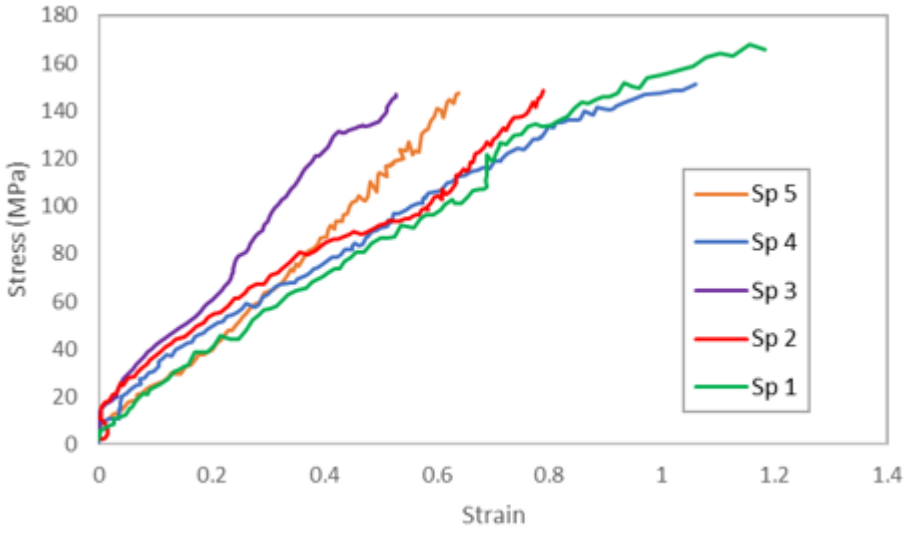

Figure 6-22: Plot of compressive stress vs. strain E-glass Elium specimens

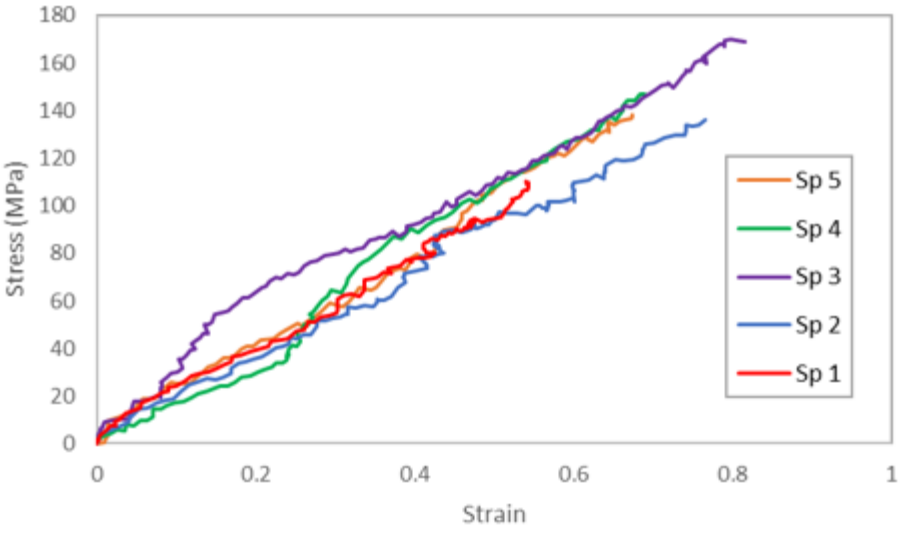

Figure 6-23: Plot of compressive stress vs. strain basalt epoxy specimens

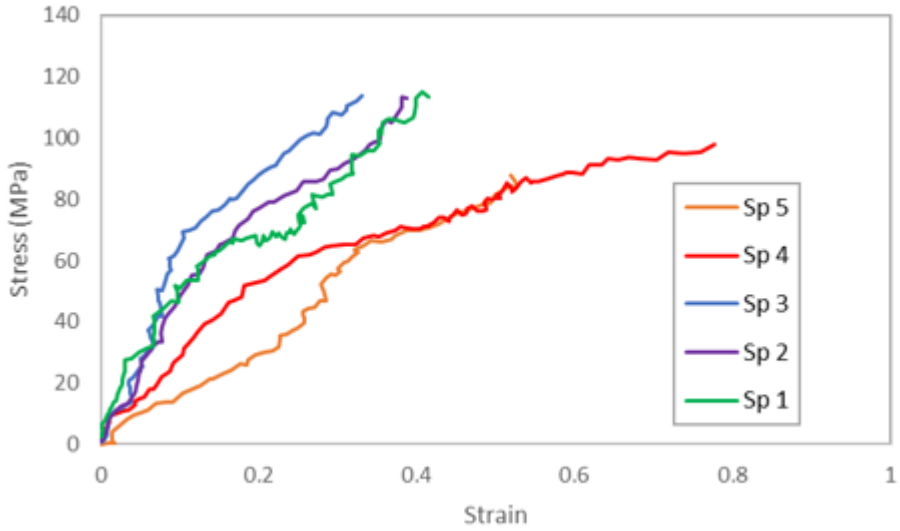

Figure 6-24: Plot of compressive stress vs. strain basalt Elium specimens

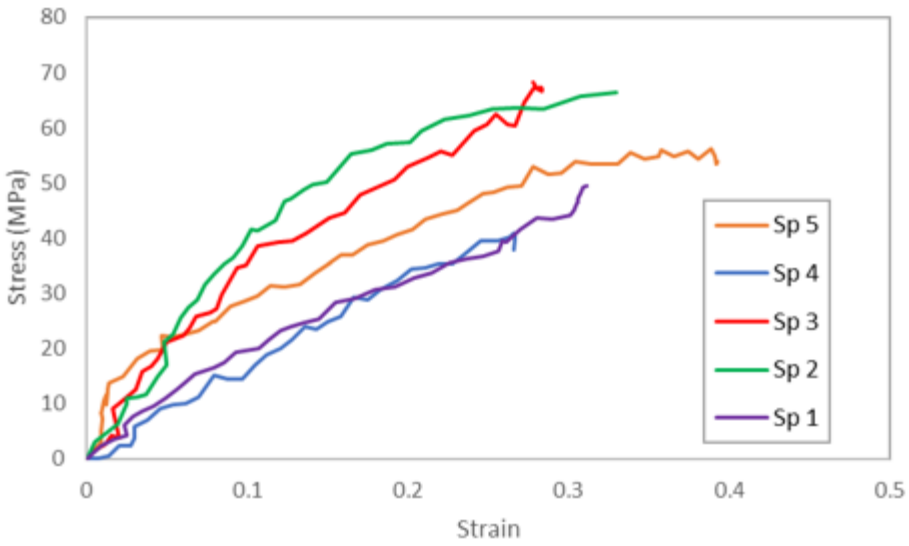

Figure 6-25: Plot of compressive stress vs. strain Kevlar-29 epoxy specimens

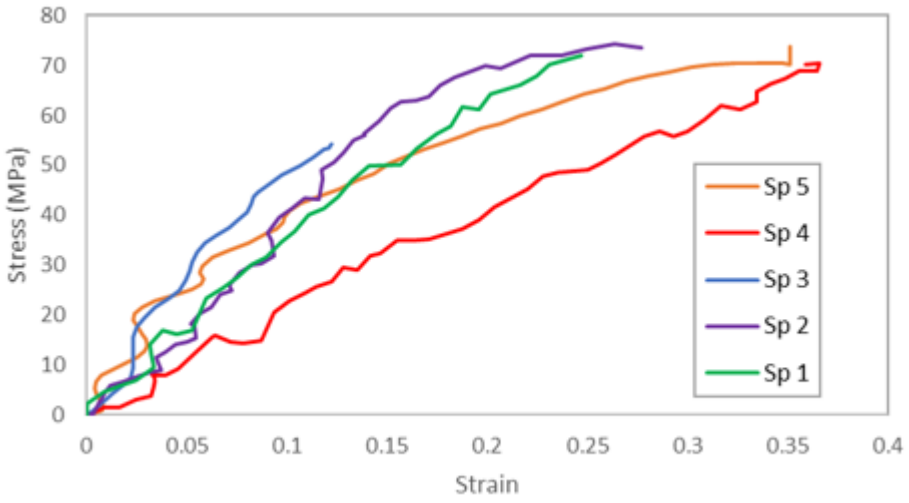

Figure 6-26: Plot of compressive stress vs. strain Kevlar-29 Elium specimens

As seen, the differences in the compressive stress-strain curve for each composite are significantly larger compared to the stress-strain responses obtained through tensile and shear tests. As a result, further microscopic examinations were carried out. Before disclosing the results of the examination, it is worth discussing the issues that are encountered in any compressive mechanical properties evaluation of composites.

Owing to the inherent nature of the compression test, the shorter gauge length compared to the tensile and shear tests, and the bi-directionality of the fabric used to fabricate the specimens, the results would have more nonlinearity and scattering than the two mentioned tests. Unlike in a tensile test where fibers take a majority of the load (over 90% of the load in composites with relatively large fiber contents, as in the composites considered in this study), in a compression test, any flaws in the matrix would have a significant impact on the response of composites. For instance, the presence of voids will lower the stability of the fibers in compression due to the absence of resin to provide lateral support to the fiber tows, thus leading to micro-buckling or shear-out of the fibers. The void content of a composite also has a significant effect on the non-linearity (the response seen in most of the tested composites) since these voids hinder the efficient transfer of load between the fibers.

For each material combination, except Kevlar-29, the epoxy-based matrix has a higher ultimate compressive strength, as seen in Table 6-8. To explain this observation, consider the failure modes in compression loading. Compressive fiber buckling, kinking, and shear-out fracturing failure modes are all dependent on maintaining the fiber load alignment, as any deviations lead to the formation of undesirable bending stress. A stiffer matrix material

would facilitate the alignment and thus the efficient bearing of load. While epoxy is a relatively stiff resin, however, it is also a brittle material that, under loading, while it could offer more resistance to fiber buckling, but it would also undergo small deformation in the presence of any voids, it would crack and cause premature failure. Elium, given its more ductile nature, would facilitate more fiber deformation. This trend was not observed in the Kevlar-29 material combinations since as explained earlier, there was greater resin absorption within the fiber bundles for Elium resin. This effect, which leads to a decrease in shear strength, under compressive loading will offer greater fiber stability as it would lead to stronger fiber bundles.

As stated, further microscopic examinations were carried out. Two composites were selected for this examination: (i) basalt-epoxy and (ii) basalt-Elium. First, the edges of the specimens were examined using a digital microscope, as illustrated in Figure 6-27 to Figure 6-30. Subsequently, scanning electron microscopy (SEM) was used to further examine the fibers and resin conditions in the two composites (see Figure 6-31 to Figure 6-35).

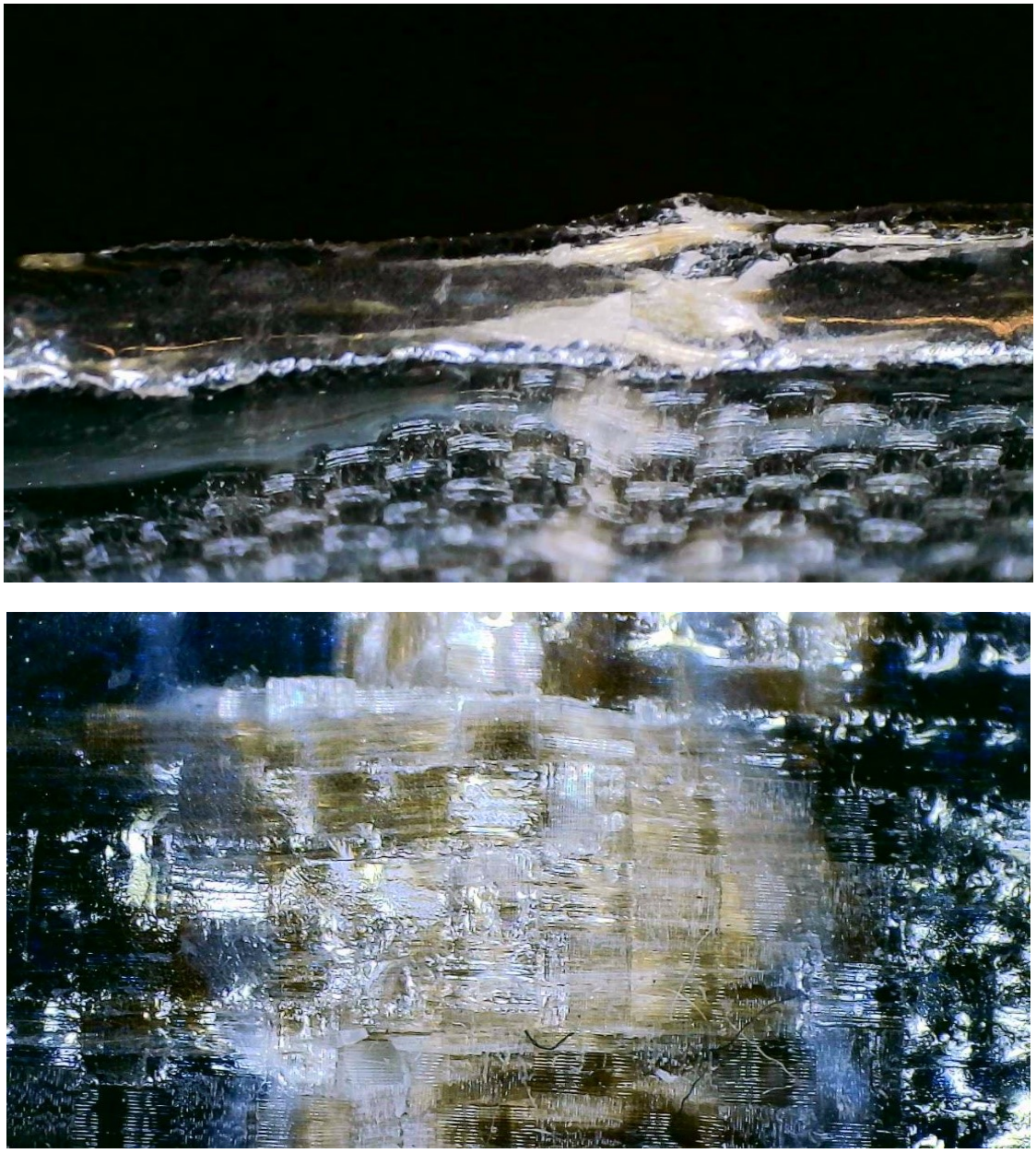

Figure 6-27: Digital microscope images of the failure region of basalt epoxy compression Sp 3 (side and top views, respectively)

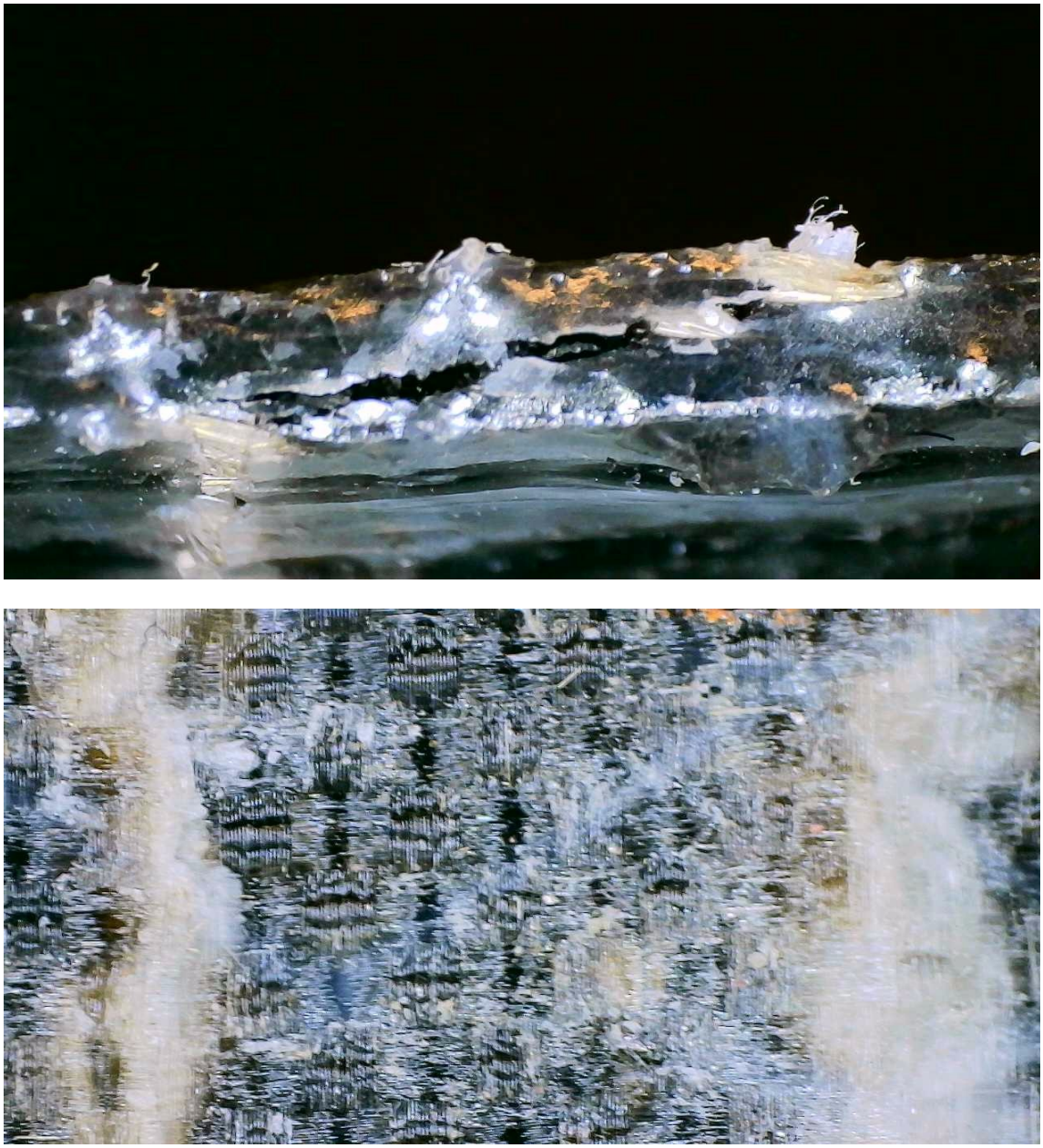

Figure 6-28: Digital microscope images of the failure region of basalt epoxy compression Sp 2 (side and top views, respectively)

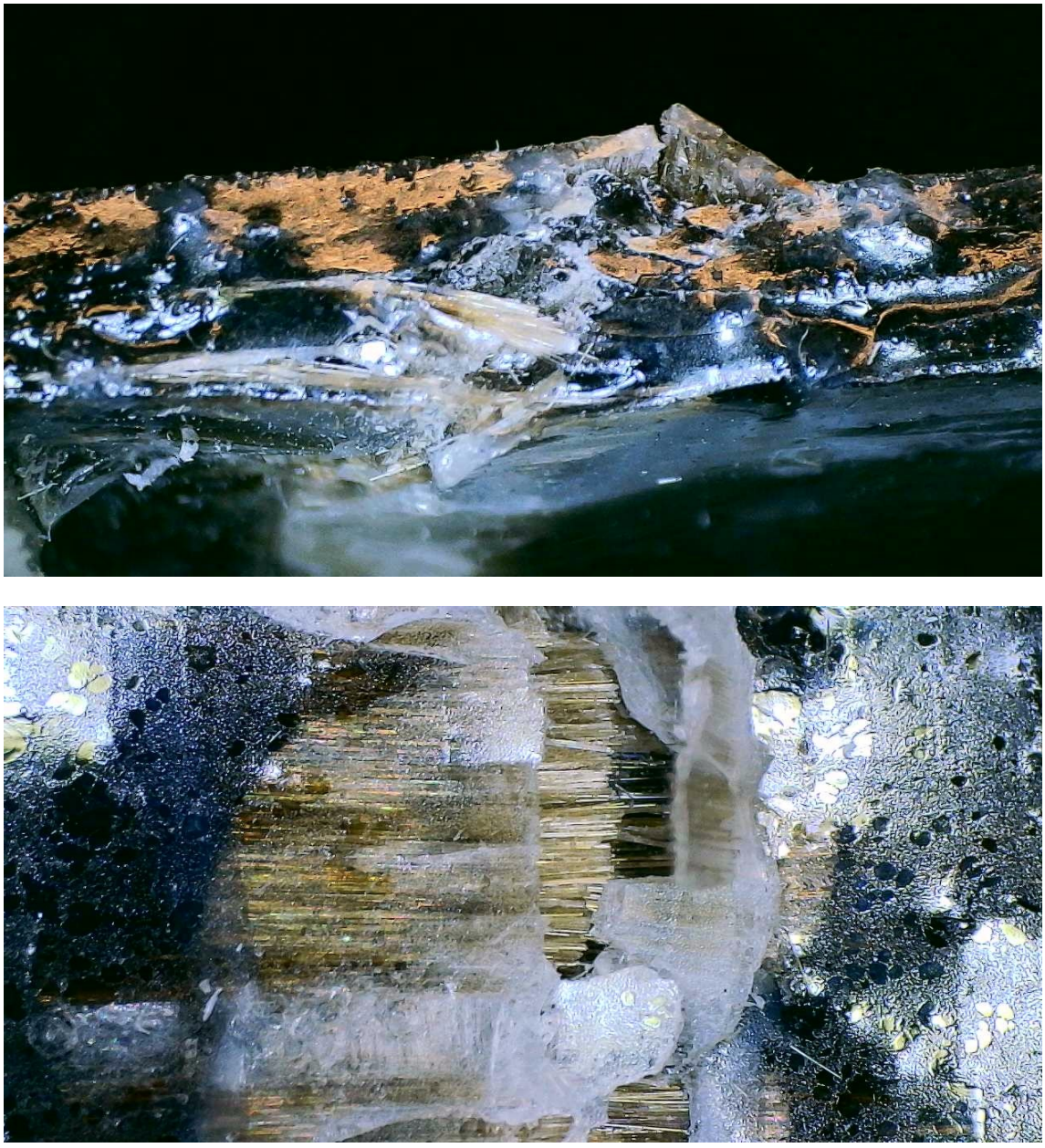

Figure 6-29: Digital microscope images of the failure region of basalt Elium compression Sp 5 (side and top views, respectively)

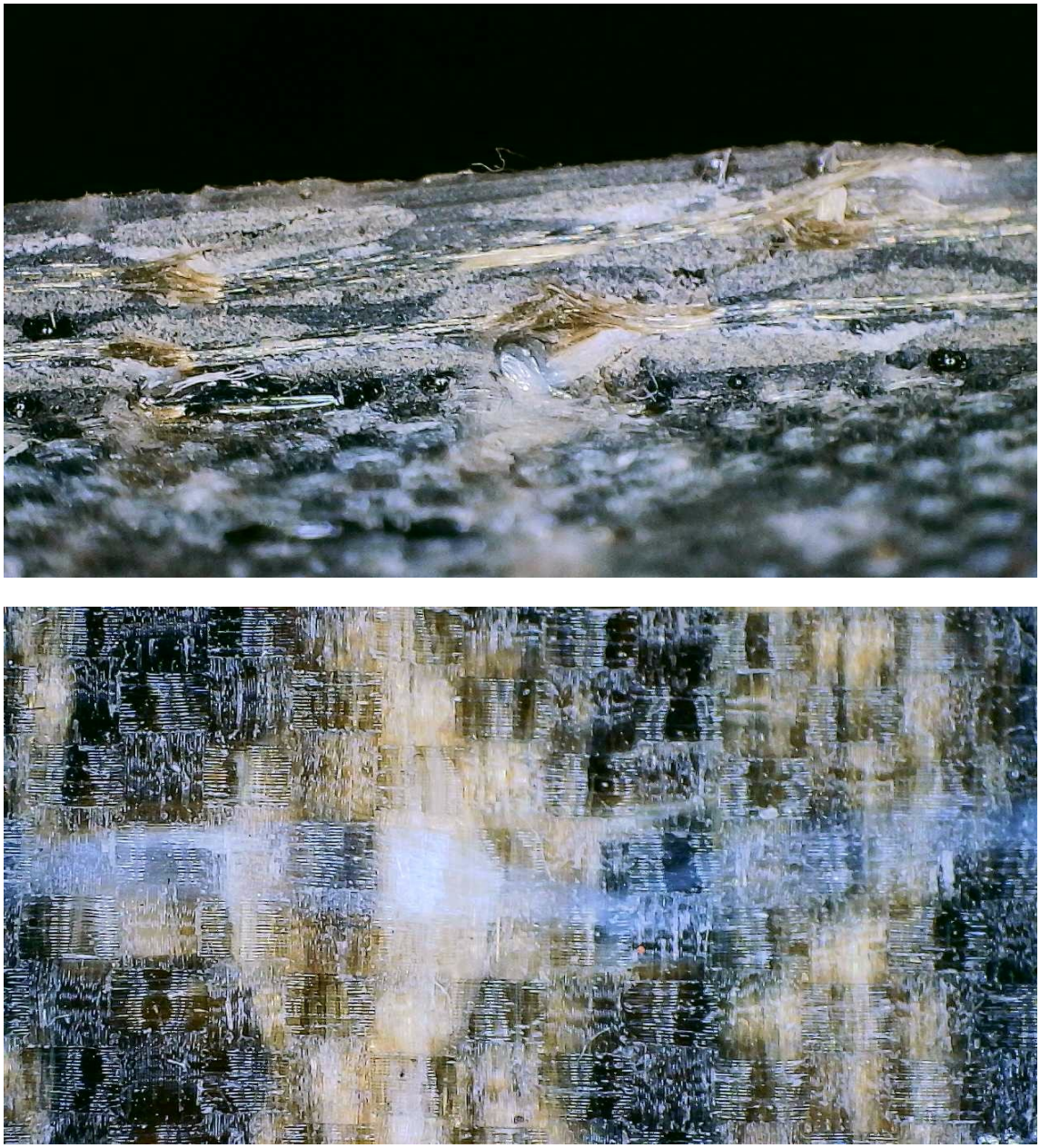

Figure 6-30: Digital microscope images of the failure region of basalt Elium compression Sp 3 (side and top views, respectively)

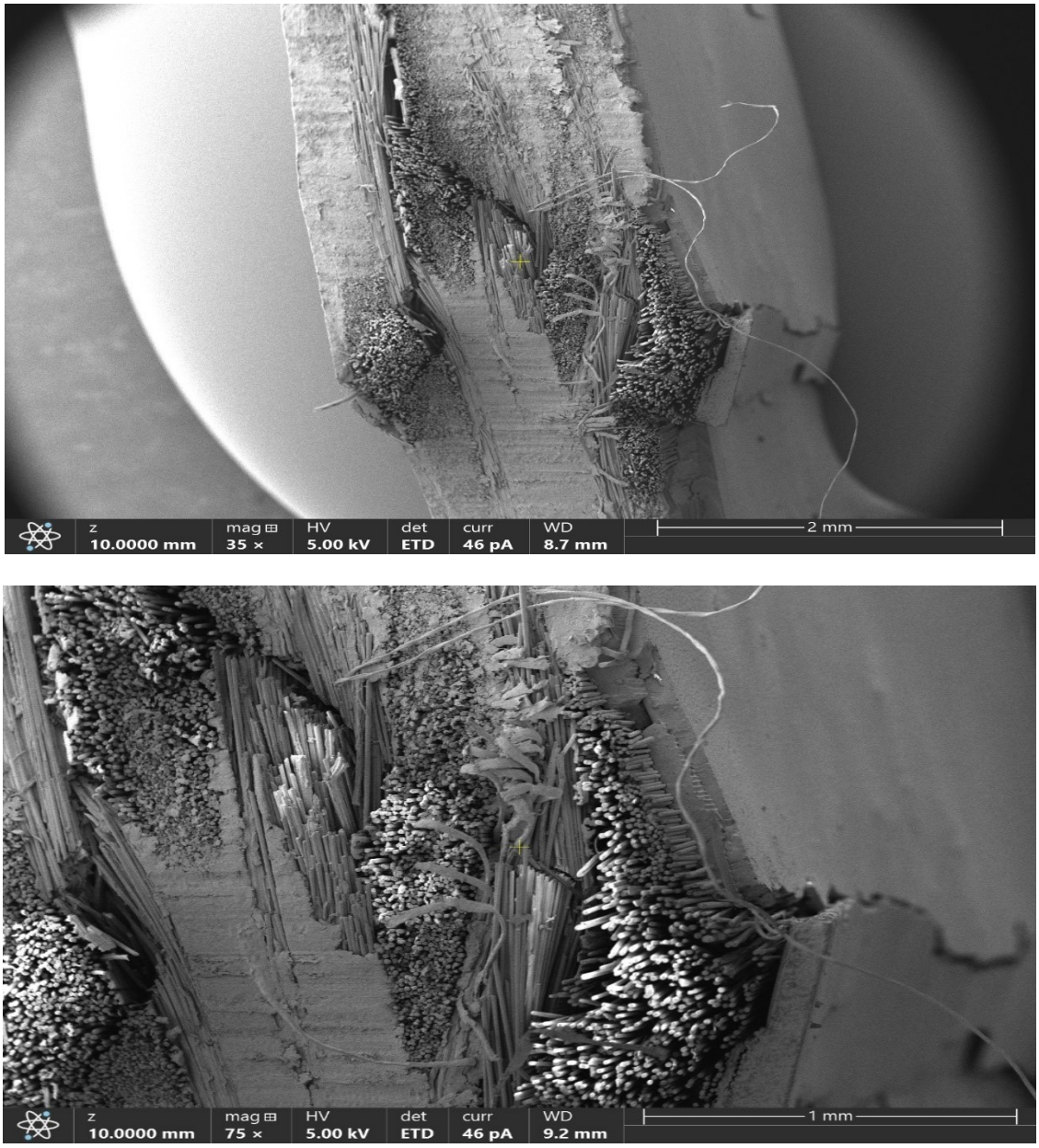

Figure 6-31: SEM images of the failure region of basalt epoxy compression Sp 3

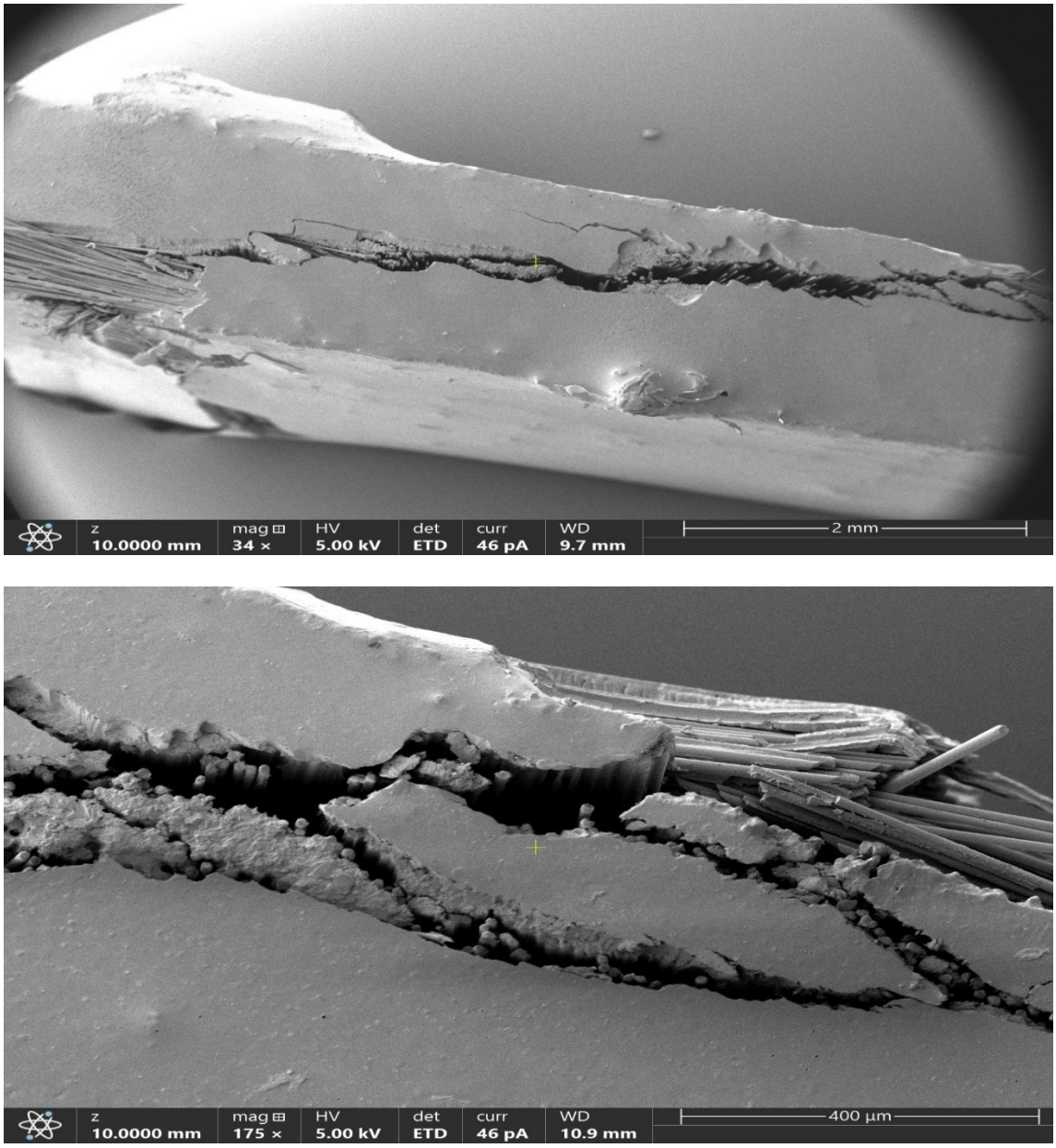

Figure 6-32: SEM images of the failure region of basalt epoxy compression Sp 2

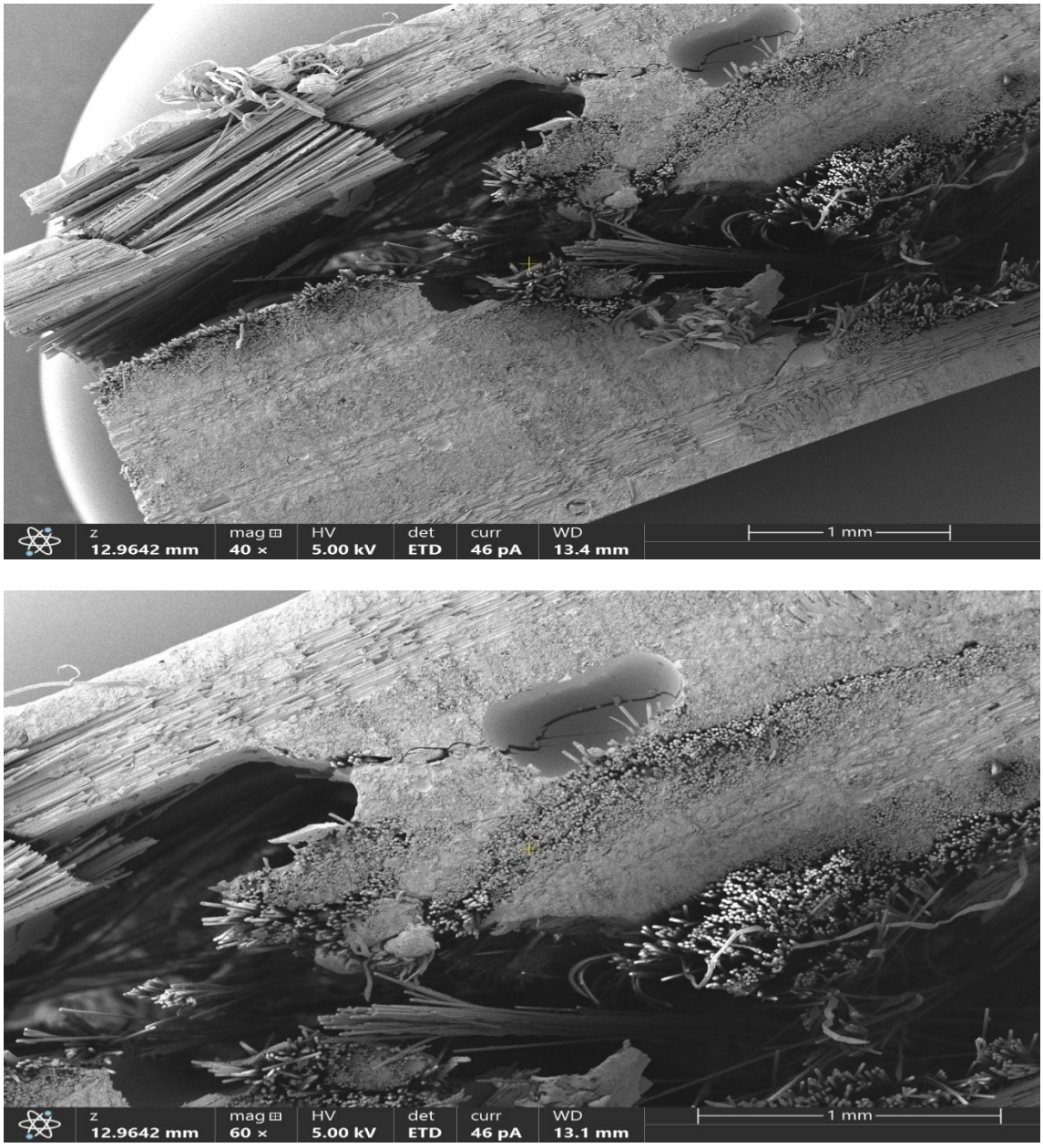

Figure 6-33: SEM images of the failure region at the cross-section of basalt Elium compression Sp 5

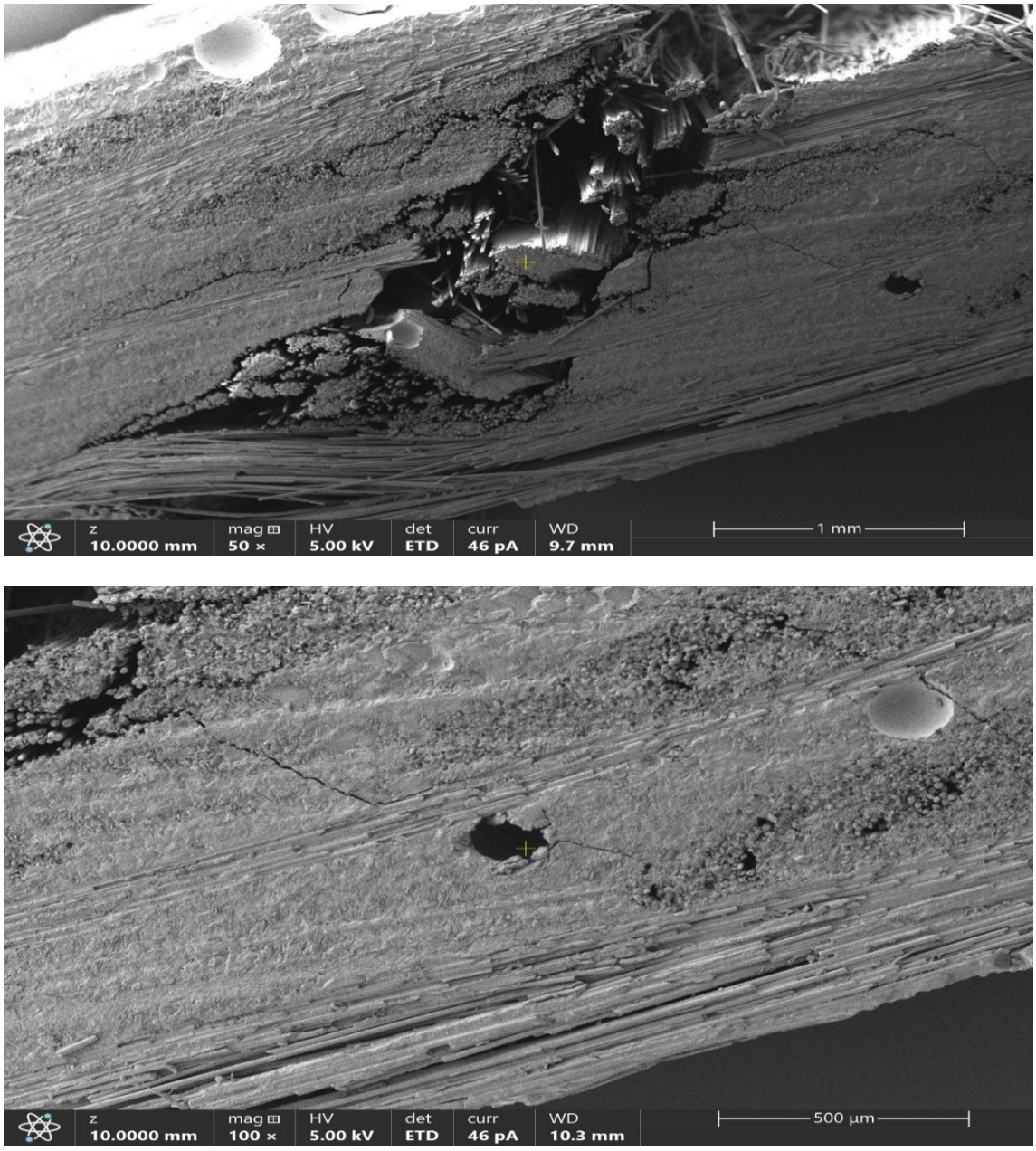

Figure 6-34: SEM images of the failure region at the cross-section of basalt Elium compression Sp 3

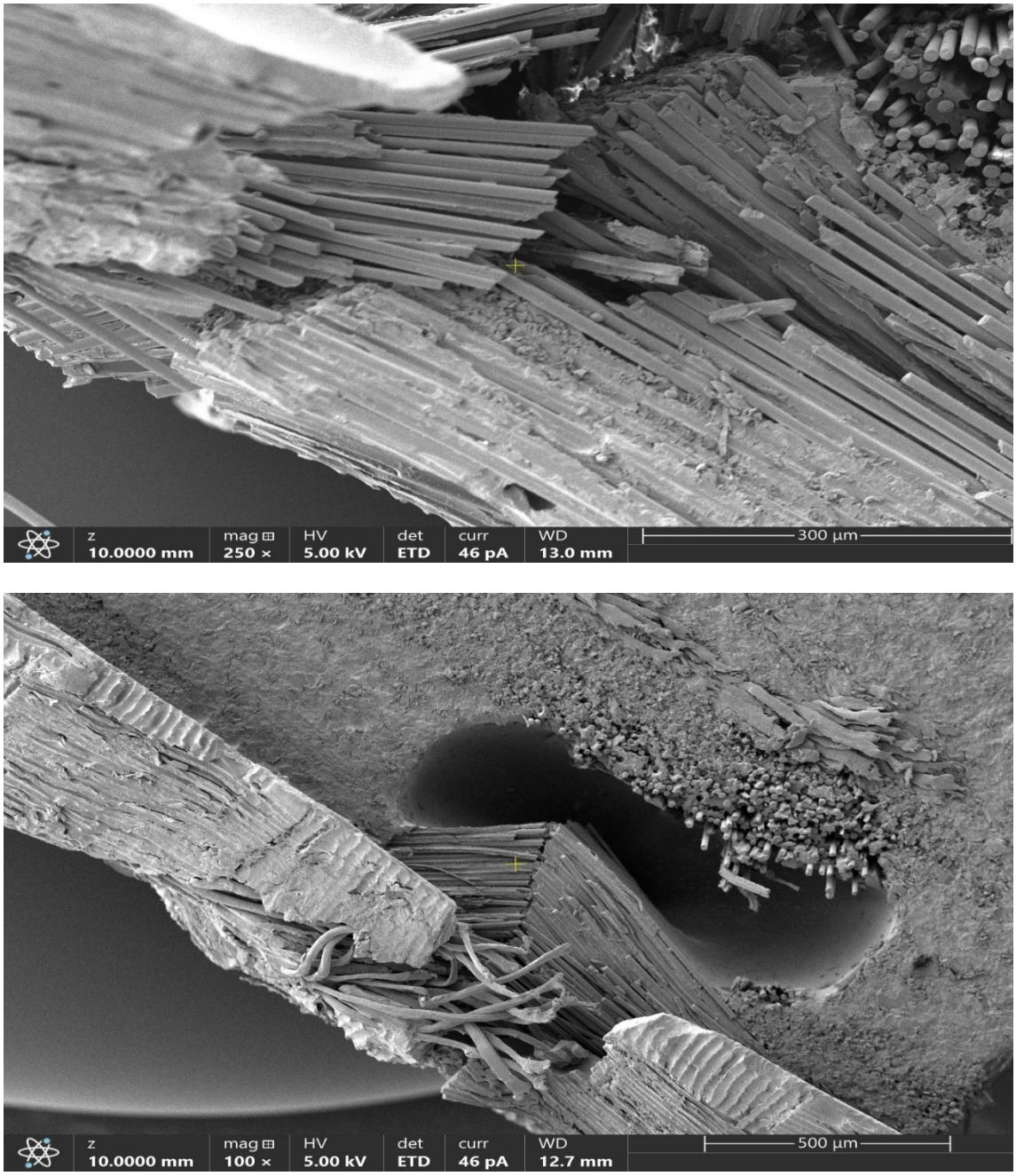

Figure 6-35: SEM images of the damaged but not failed region of basalt Elium compression Sp 35

Figure 6-27 illustrates the failure mode of the basalt-epoxy specimen 3 as micro-buckling. This failure mode is further examined by the SEM image shown in Figure 6-31. The figure shows that the failure of the specimen more accurately as fiber shear-out failure seemingly initiated by the crumpling of the non-loaded transverse fiber tows, thereby reducing the stability of the load-bearing adjacent fibers. The SEM images in Figure 6-34 show a similar failure mode for the basalt-Elium specimen 3, even though the digital microscopic image in Figure 6-30 appears again to show micro-buckling. The location of micro-buckling in basalt-Elium specimen 3 is in a section of the test specimen that did not cause the catastrophic failure of the specimen. Figure 6-35 shows micro-buckling of loaded fibers due to instability, most probably initiated due to the lack of lateral support to the fiber tows adjacent to the relatively large void visible in the image. It is postulated that the voids seen in the SEM images were created as a result of the higher outgassing of Elium resin. The effect of the outgassing, whose outcome could also be observed in the density and void content results, increases the likelihood of a micro-buckling event. The results of these micro-buckling events are believed to have caused the undulations seen in the compressive stress-strain curves illustrated earlier.

It should be emphasized that the presence of a relatively large void causes the development of a significant stress concentration that can initiate failure within a composite that could have otherwise exhibited a greater load-bearing capacity. Figure 6-35 shows the SEM image of the failure of the basalt-Elium compression specimen 5, which was initiated by the adjacent void within the material. The microcracks extending from the failure regions traveled through the voids and the transverse fiber tows, as these features offer a

path of lower resistance. Similar stress relief fractures can be seen radiating outward from the failure mode in Figure 6-34, where again a crack traverses through both the voids and transverse fiber tows. The fractures from the failure of the basalt-epoxy specimen 2 seen in the SEM images in Figure 6-32 show the shear failure caused by the axial load, causing interlaminar debonding in the region adjacent to the neighboring, which in turn caused the shear-out failure of the load-bearing fibers.

6.4. Impact Test Results

6.4.1. High-Velocity Impact Test Results

The HVI test is performed following the US Army Research Laboratory Bisection Method [10]. The test is performed using a compressed air gas gun firing a 9.53 mm dia. steel spherical projectile with a mass of 3.5 g. Six specimens were used per composite material configuration. The velocity before and after were recorded using the two chronographs.

Table 6-9: Ballistic limit velocity of the composites

Material	Ballistic limit
E-glass epoxy	128.5 m/s
E-glass Elium	131 m/s
Basalt epoxy	142.5 m/s
Basalt Elium	148 m/s
Kevlar epoxy	116 m/s
Kevlar Elium	122 m/s

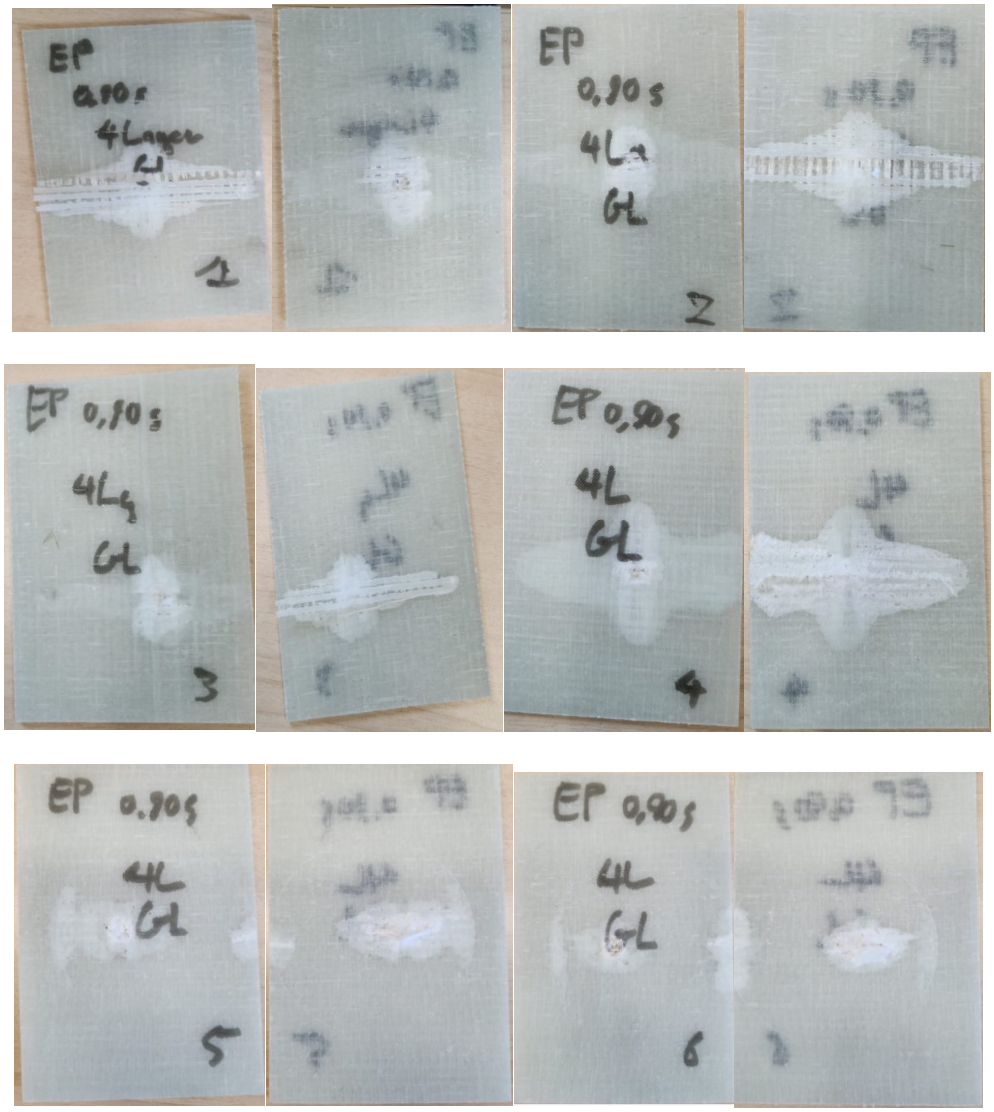

Figure 6-36: Post HVI view of E-glass epoxy specimens (front and rear, respectively)

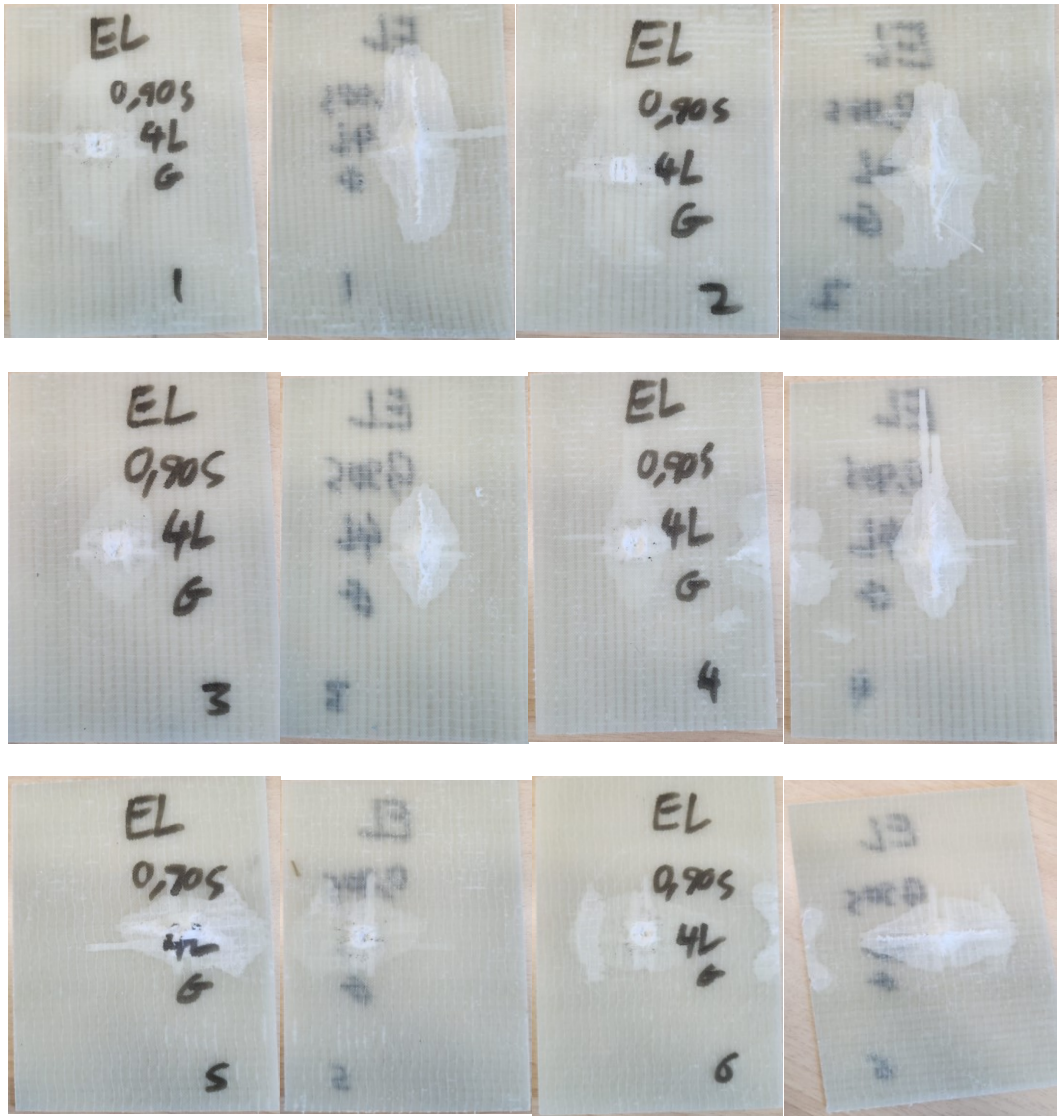

Figure 6-37: Post HVI view of E-glass Elium specimens (front and rear, respectively)

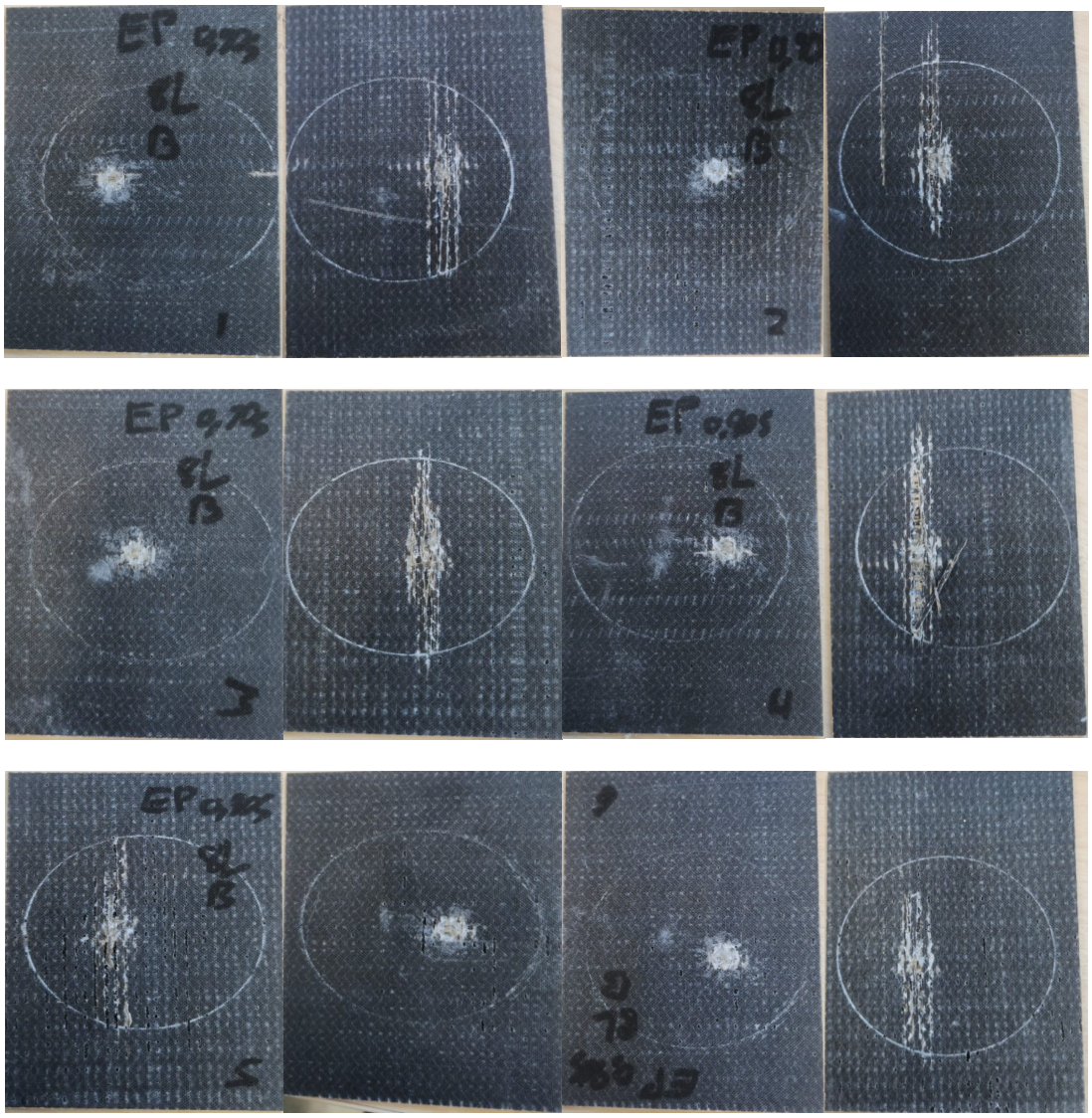

Figure 6-38: Post HVI view of basalt epoxy specimens (front and rear, respectively)

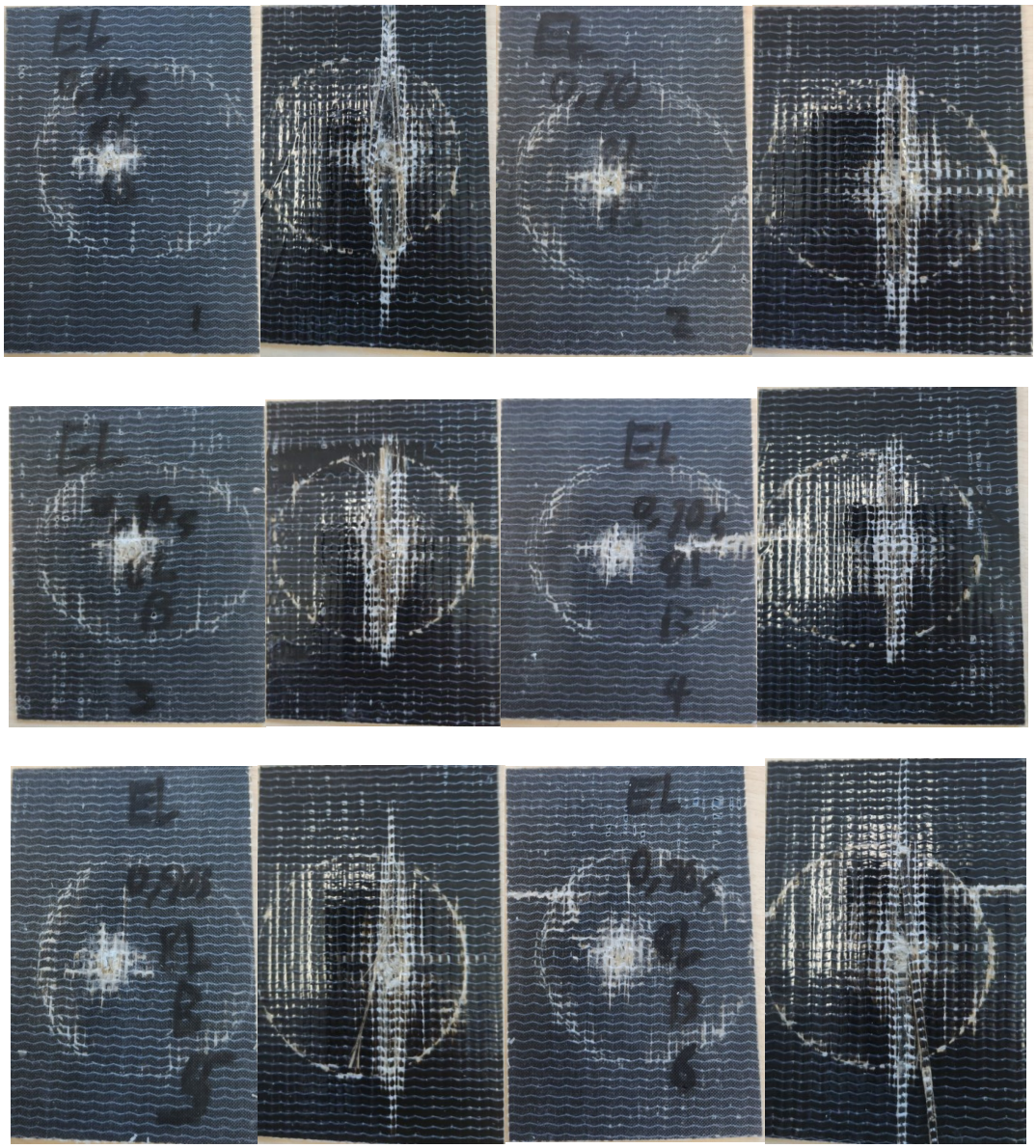

Figure 6-39: Post HVI view of basalt Elium specimens (front and rear, respectively)

Figure 6-40: Post HVI view of Kevlar-29 HVI specimens (front and rear, respectively)

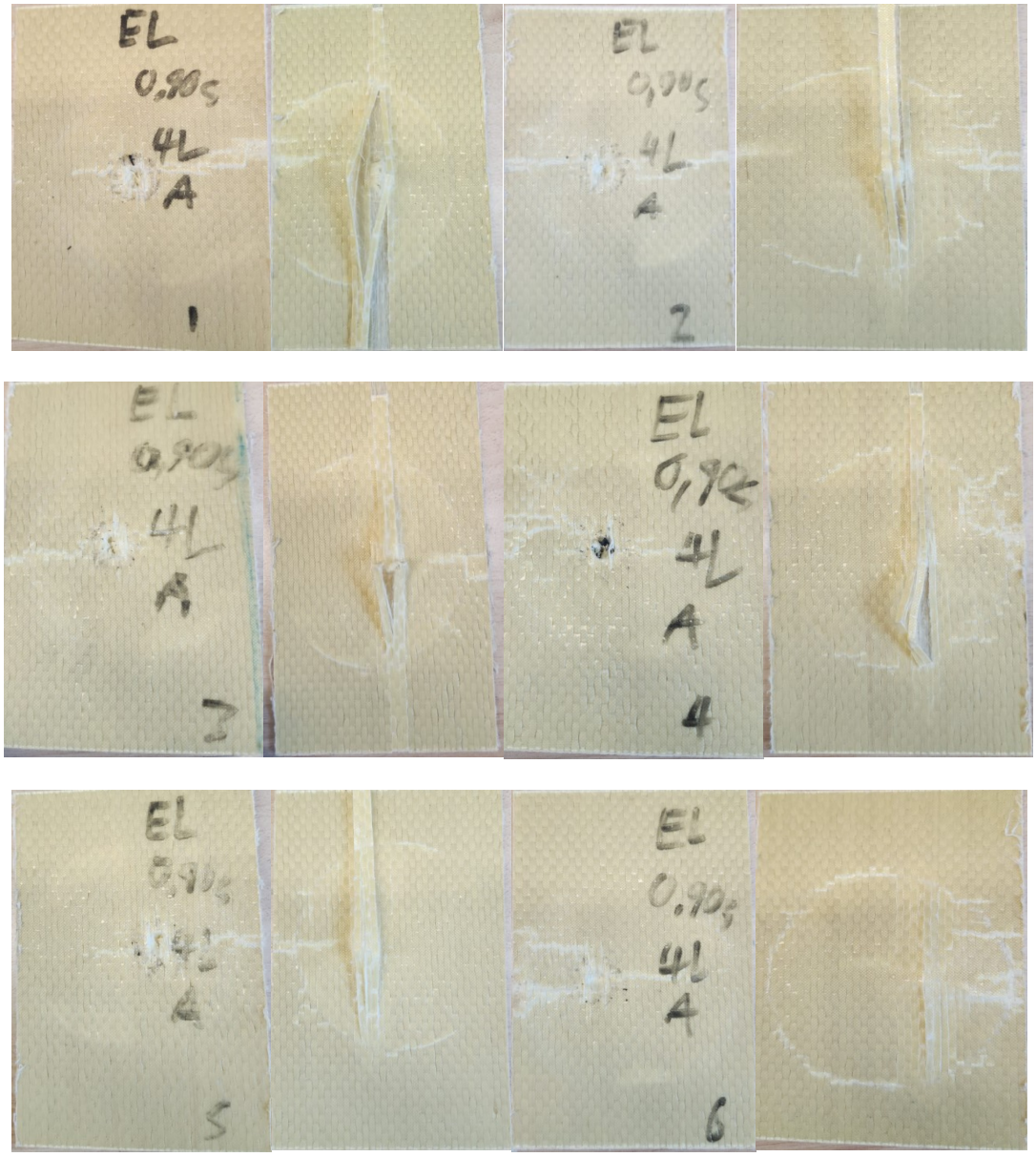

Figure 6-41: Post HVI view of Kevlar-29 Elium specimens (front and rear, respectively)

Table 6-10: Ballistic limit energy increase of Elium composites compared to epoxy composites

Material	Energy increase	% increase
E-glass Ballistic limit Energy increase	1.14 J	1.95
Basalt Ballistic limit Energy increase	2.80 J	3.86
Kevlar-29 Ballistic limit Energy increase	2.50 J	5.17

Table 6-11: Ballistic limit velocities normalized with respect to the average value of E-glass epoxy specimen

Materials	Normalized values
E-glass epoxy	1 m/s
E-glass Elium	1.02 m/s
Basalt epoxy	1.11 m/s
Basalt Elium	1.15m/s
Epoxy kevlar	0.90 m/s
Kevlar Elium	0.95 m/s

Table 6-12: Ballistic limit velocities normalized with respect to specimen resin weight percentage

Material	Normalized values
E-glass epoxy	2.44 m/s
E-glass Elium	2.71 m/s
Basalt epoxy	3.12 m/s
Basalt Elium	3.49 m/s
Kevlar epoxy	2.29 m/s
Kevlar Elium	3.10 m/s

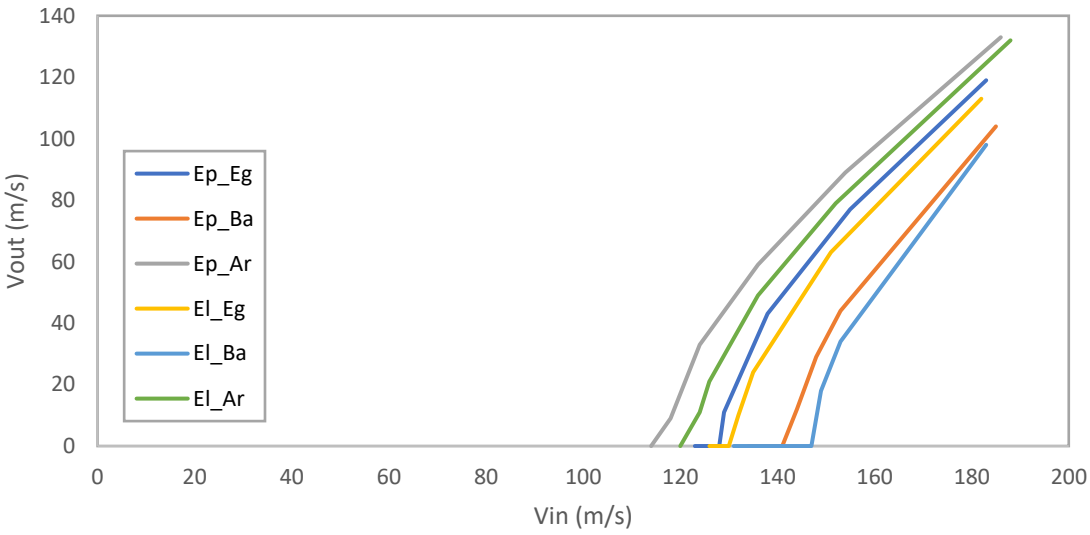

Figure 6-42: Graphs of impact velocity vs. velocity after penetration of the composites

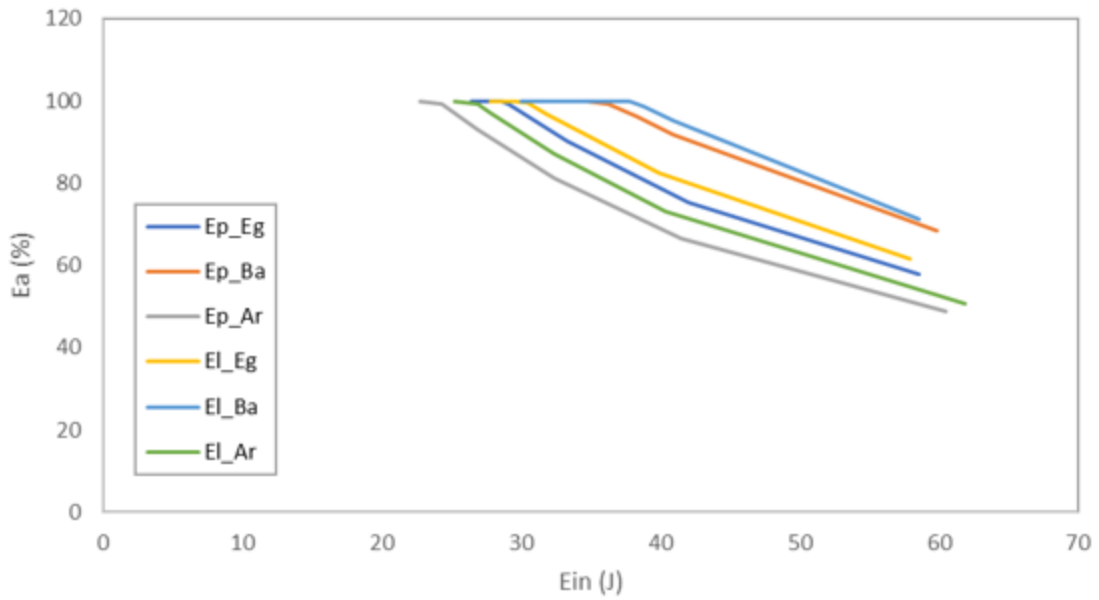

Figure 6-43: Graphs of energy incident vs. percent absorbed energy of the composites

It can be seen from the results, that the ballistic limit of the composites made with an Elium-based matrix has a higher value. This higher ballistic limit is due to the more ductile nature of Elium and its higher fracture toughness compared to epoxy. The higher ductility and fracture toughness facilitates the absorption of more energy when compared to a brittle material. This increased energy absorption is based on the fact that the area under the stress-strain curve signifies the energy that can be absorbed by a material or the strain energy capacity of the material. A ductile material has a larger area as it has a curve that extends past its linear elastic region (or past its yield strength). The same is not true for brittle materials, since brittle materials tend to have a linear region with no or minimal strain carrying capacity beyond the yield point.

In Figure 6-36, Figure 6-38, and Figure 6-40 the failure modes for the epoxy-based

composites can be characterized as fiber pull-out, fiber tear-out, and delamination. The Most dominant failure mode that can be observed is the fiber pull-out for both the E-glass and basalt-based composites while the fiber tear-out and delamination are both less significant contributors. For the Kevlar-29 composites, the most common failure mode is the fiber tear-out, where the tear-out event is primarily localized to the point of penetration. Through examination of Figure 6-37, Figure 6-39, and Figure 6-41 one could characterize the failure modes of Elium-based composites as fiber tear-out, fiber pull-out, delamination, and local deformation. The E-glass composite's dominant failure mode is delamination while the basalt has delamination, fiber pull-out, and local deformation. The Kevlar-29 composites have similar failure mode profiles as the basalt composites.

The observation of local deformation in the Elium-based composites is characteristic of the thermoplastic nature of Elium. It is worth noting that while the similarities in failure modes of delamination fiber pull-out, and fiber tear-out are common on both specimens, the characteristics of these modes differ for the two plastics. Where the fiber pull-out, fiber tear-out, and delamination contain sharper borders and inflexibility in the protrusions for the epoxy matrix, while Elium exhibits a rounded and flexible nature to these modes. Table 6-10 indicates that the Kevlar-29 composites had the greatest increase in ballistic performance with the addition of Elium with basalt being closely comparable. The normalized results in Table 6-11 show that basalt epoxy outperformed the E-glass epoxy. This higher performance is worth noting since basalt is a naturally occurring substance and its pairing with a recyclable plastic can see applications potentially replacing E-glass epoxy composites as a more environmentally friendly alternative.

Next, the normalization with the resin content showed the trend of Elium outperforming epoxy with the ballistic limit per material resin percentage having higher values for Elium when compared to epoxy. Basalt again shows the most promise. The charts seen in Figure 6-42 and Figure 6-43 show that as the incident velocity increases the observed energy absorption remains mostly constant with a convergence at the extreme values. This convergence is due in part to the effectiveness of the resin to absorb energy being reduced with significantly higher velocities while the fiber becomes the dominant loading constituent.

6.4.2. Low-Velocity Impact Test Results

As stated earlier, the LVI test is performed following ASTM D7139 with a few modifications to the setup as also explained in the previous chapter [55]. Briefly, this test was performed using a modified Charpy impacting device. This device is the only modification to the testing setup outlined in ASTM D7139 since the method employed in the standard is a drop-weight testing setup. The use of the modified method eliminates the bouncing back of the drop weight method and the resulting uncontrollable multi-impacting.

Three levels of impact energy (i.e., 25, 40 and 55 Joules) were used and three specimens per energy level were tested. The test results are reported as follows:

Table 6-13: LVI results

E-glass epoxy		
Average Force (N) @ 55 J	Standard Deviation	Coeff. var.
7114.85	527.07	6.66
Average Force (N) @ 40 J	Standard Deviation	Coeff. var.
7511.58	44.96	0.60
Average Force (N) @ 25 J	Standard Deviation	Coeff. var.
5982.90	735.46	12.29
E-glass Elium		
Average Force (N) @ 55 J	Standard Deviation	Coeff. var.
8373.15	466.14	5.58
Average Force (N) @ 40 J	Standard Deviation	Coeff. var.
7892.95	260.80	3.30
Average Force (N) @ 25 J	Standard Deviation	Coeff. var.
6631.65	443.14	6.68
Basalt epoxy		
Average Force (N) @ 55 J	Standard Deviation	Coeff. var.
7165.22	617.11	18.02
Average Force (N) @ 40 J	Standard Deviation	Coeff. var.
6886.80	244.49	10.49
Average Force (N) @ 25 J	Standard Deviation	Coeff. var.
6029.54	88.67	1.48
Basalt Elium		
Average Force (N) @ 55 J	Standard Deviation	Coeff. var.
8831.26	518.70	5.87
Average Force (N) @ 40 J	Standard Deviation	Coeff. var.
7942.06	718.62	9.05
Average Force (N) @ 25 J	Standard Deviation	Coeff. var.
6484.40	511.77	7.89
Kevlar-29 epoxy		
Average Force (N) @ 55 J	Standard Deviation	Coeff. var.
3051.58	670.51	21.97
Average Force (N) @ 40 J	Standard Deviation	Coeff. var.
4115.38	222.93	5.42
Average Force (N) @ 25 J	Standard Deviation	Coeff. var.
3648.67	196.26	5.38
Kevlar-29 Elium		
Average Force (N) @ 55 J	Standard Deviation	Coeff. var.
3497.20	41.13	1.18
Average Force (N) @ 40 J	Standard Deviation	Coeff. var.
3885.79	52.61	1.35
Average Force (N) @ 25 J	Standard Deviation	Coeff. var.
4634.42	517.83	11.17

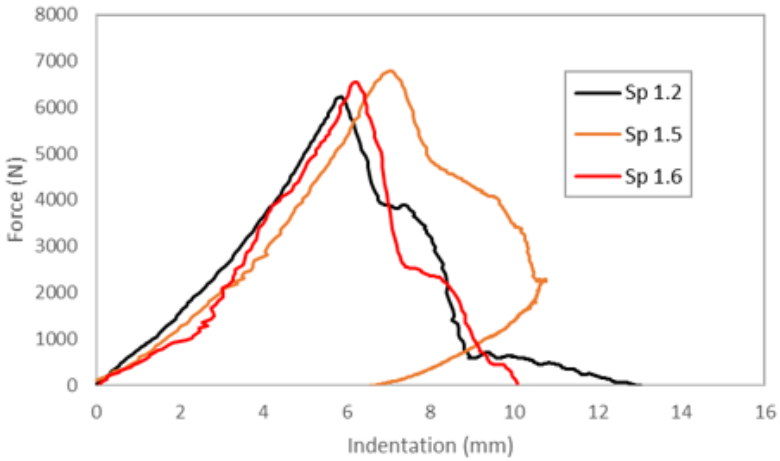

Figure 6-44: Plot of LVI force vs. indentation of E-glass epoxy with an impact energy of 55 J

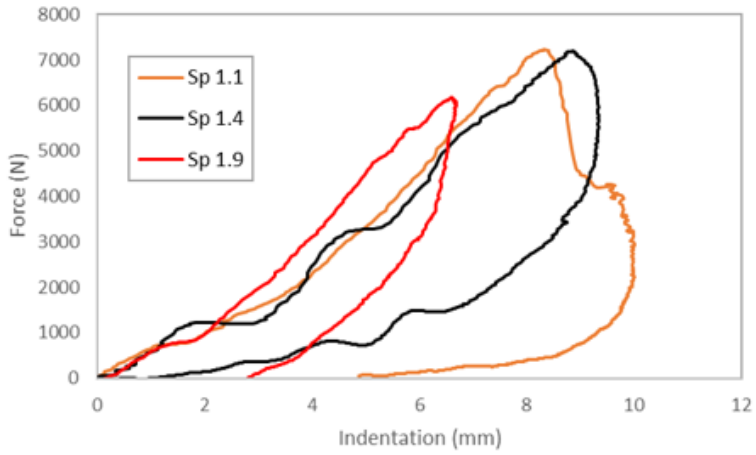

Figure 6-45: Plot of LVI impact force vs. indentation of E-glass epoxy with an impact energy of 40 J

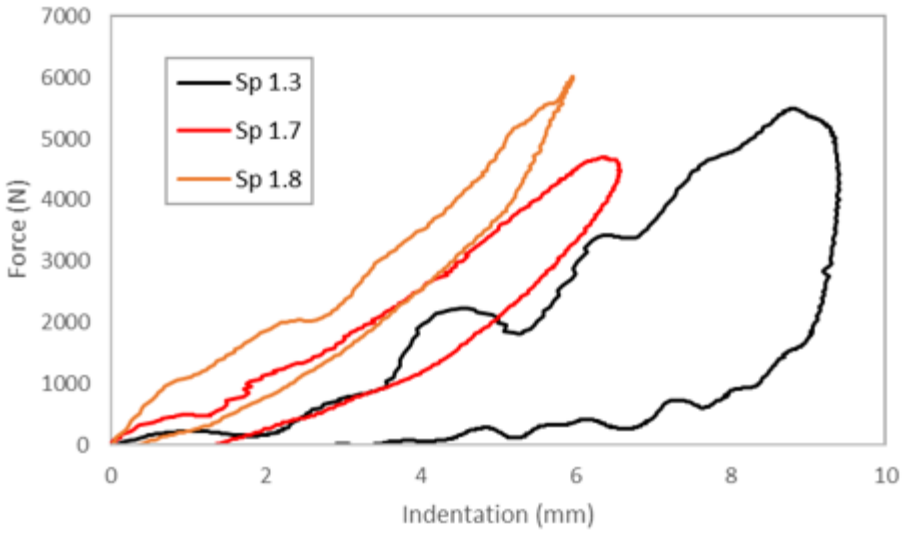

Figure 6-46: Plot of LVI impact force vs. indentation of E-glass epoxy with an impact energy of 25 J

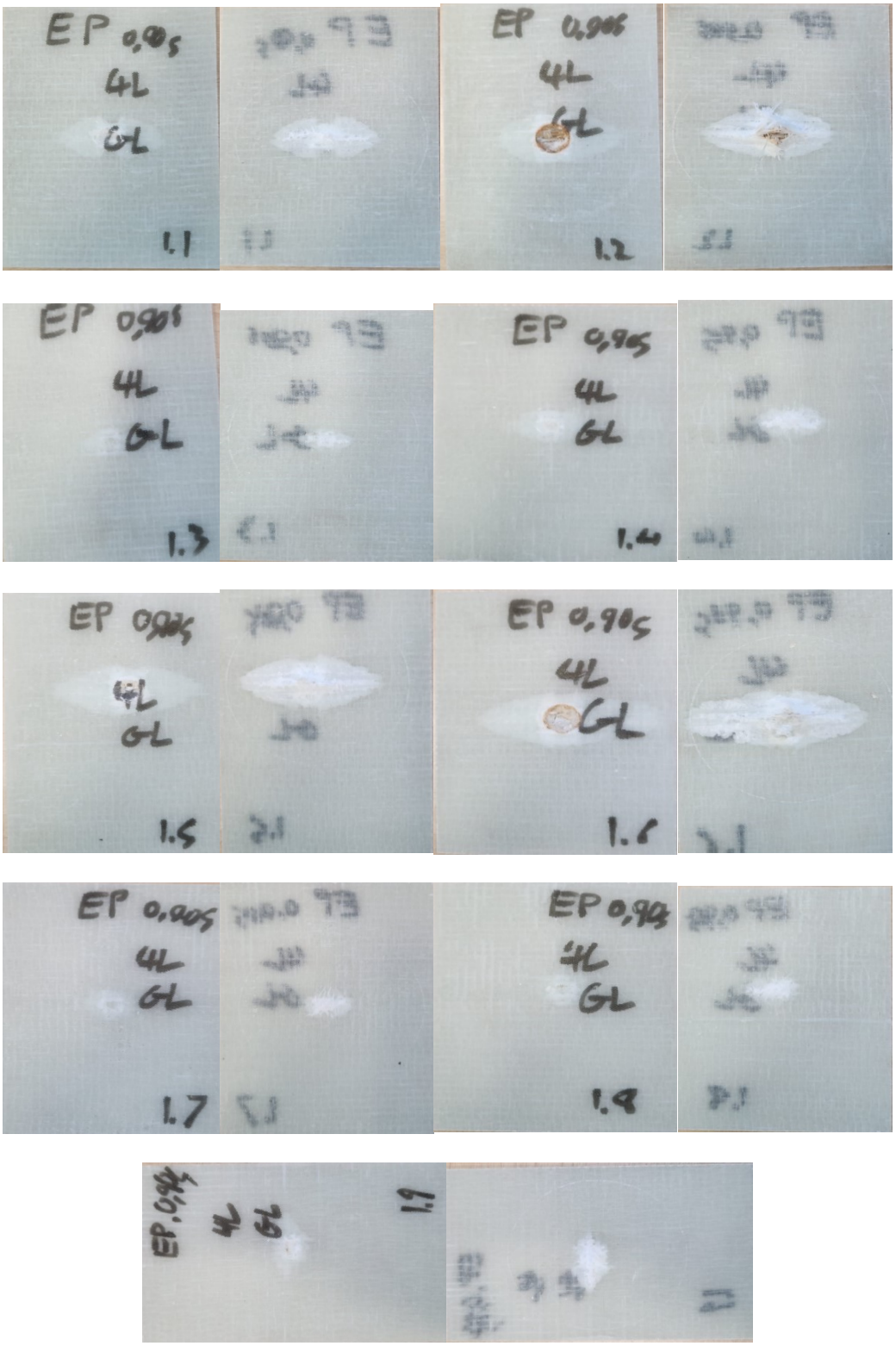

Figure 6-47: Post LVI view of E-glass epoxy specimens (front and rear, respectively)

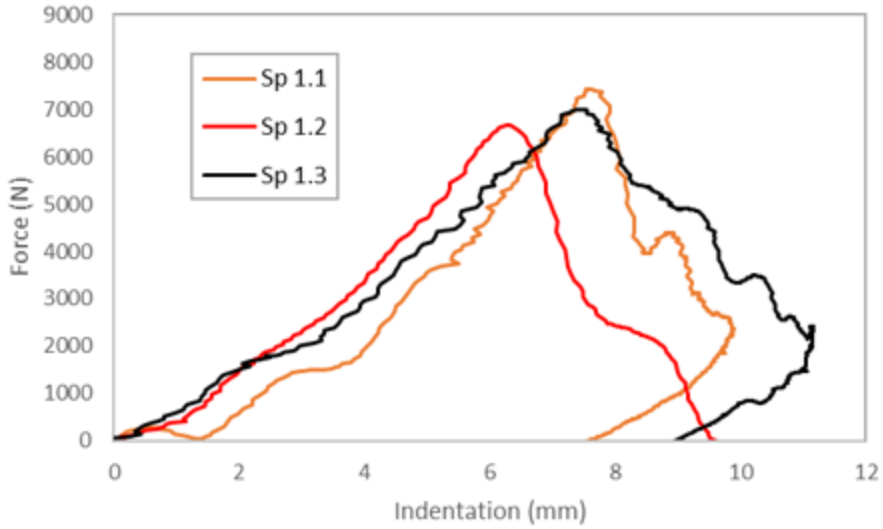

Figure 6-48: Plot of LVI impact force vs. indentation of E-glass Elium with an impact energy of 55J

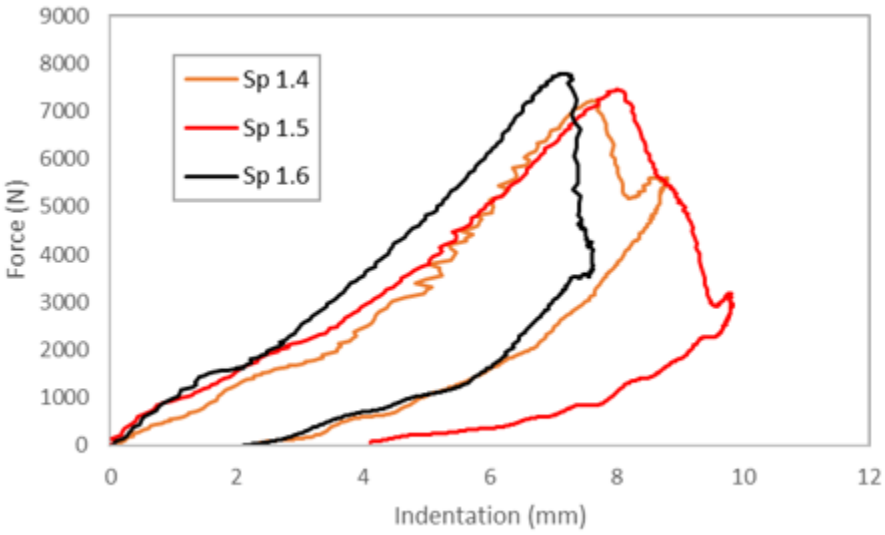

Figure 6-49: Plot of LVI impact force vs. indentation of E-glass Elium with an impact energy of 40 J

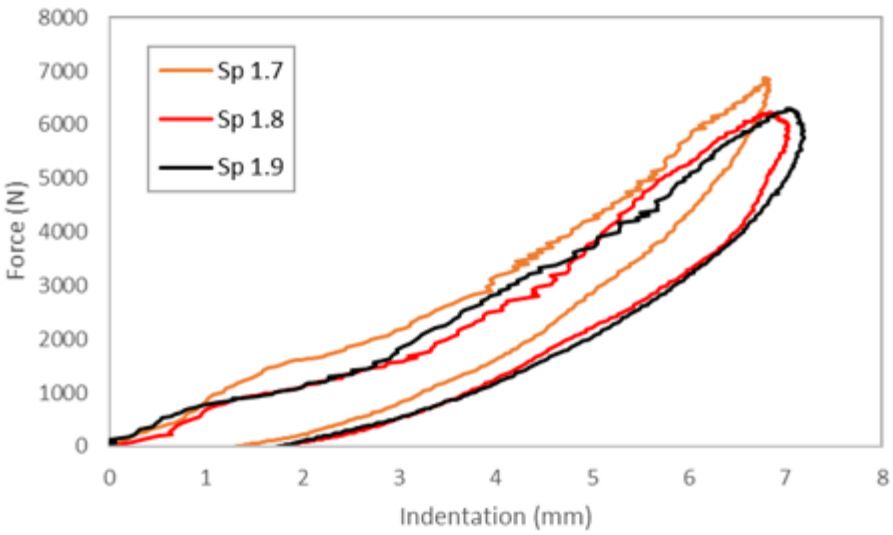

Figure 6-50: Plot of LVI impact force vs. indentation of E-glass Elium with an impact energy of 25 J

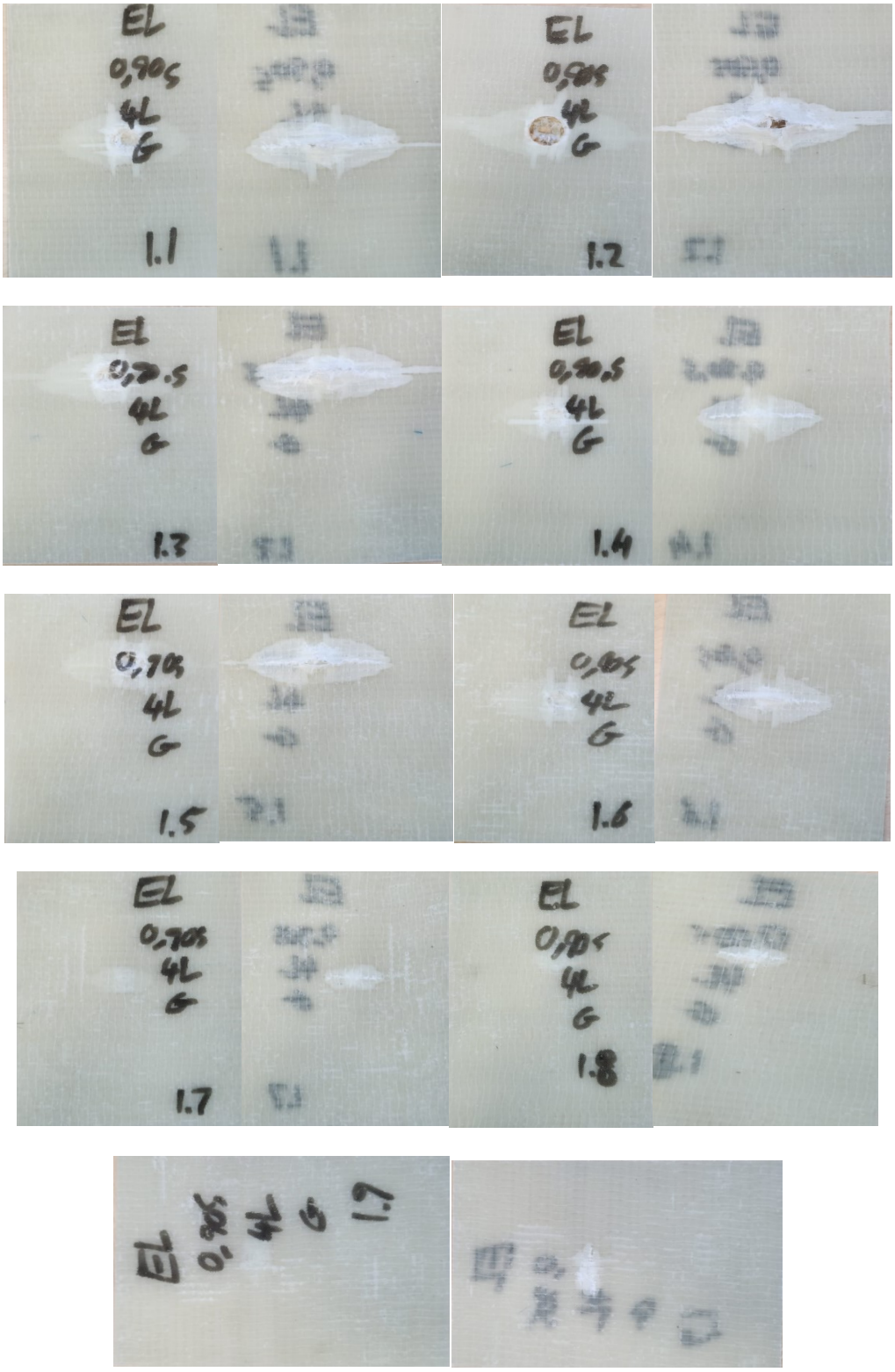

Figure 6-51: Post LVI view of E-glass Elium specimens (front and rear, respectively)

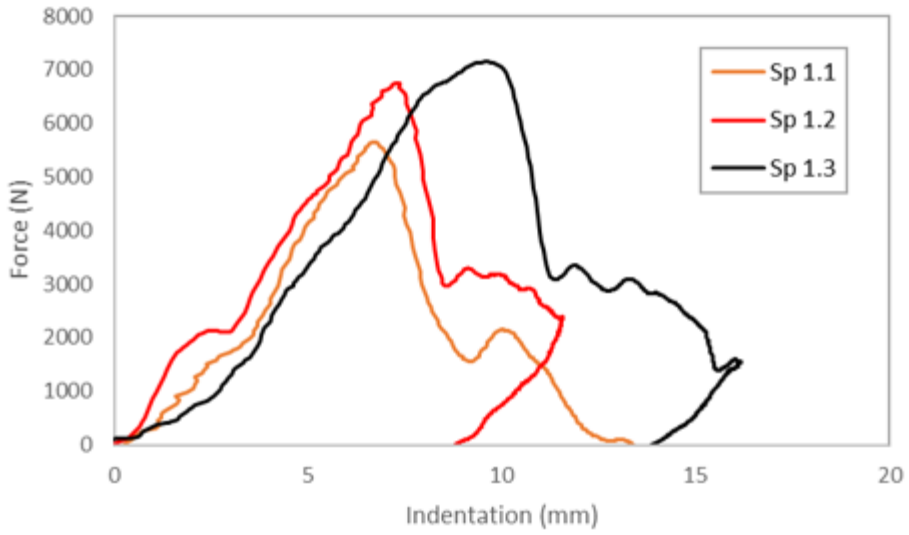

Figure 6-52: Plot of LVI impact force vs. indentation of basalt epoxy with an impact energy of 55 J

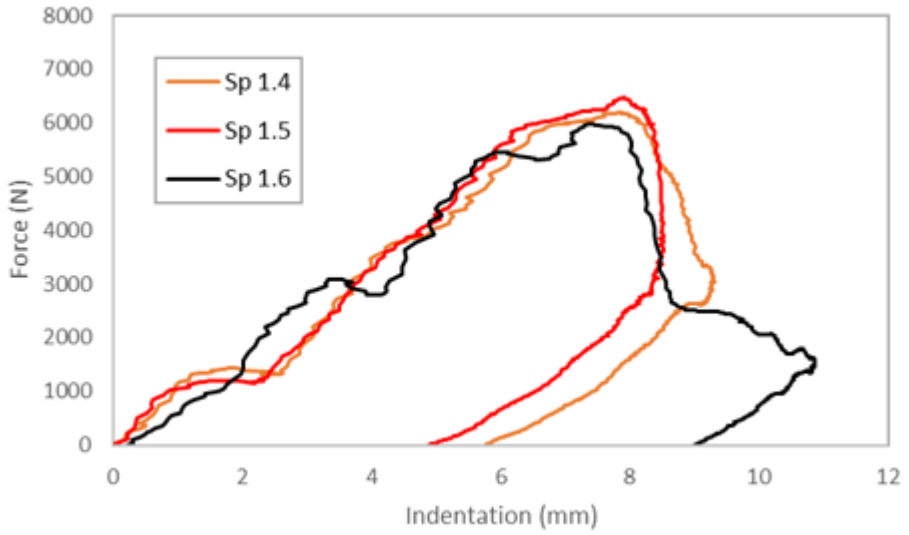

Figure 6-53: Plot of LVI impact force vs. indentation of basalt epoxy with an impact energy of 40 J

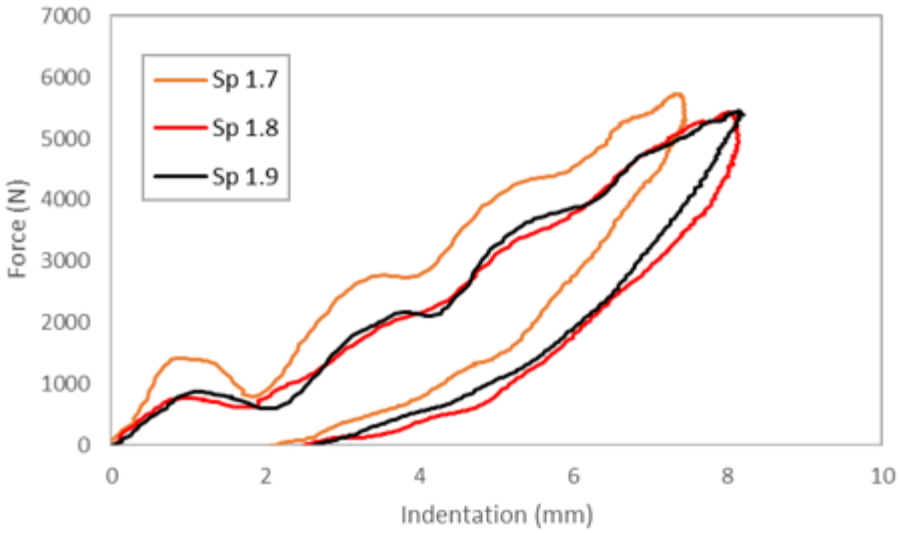

Figure 6-54: Plot of LVI impact force vs. indentation of basalt epoxy with an impact energy of 25 J

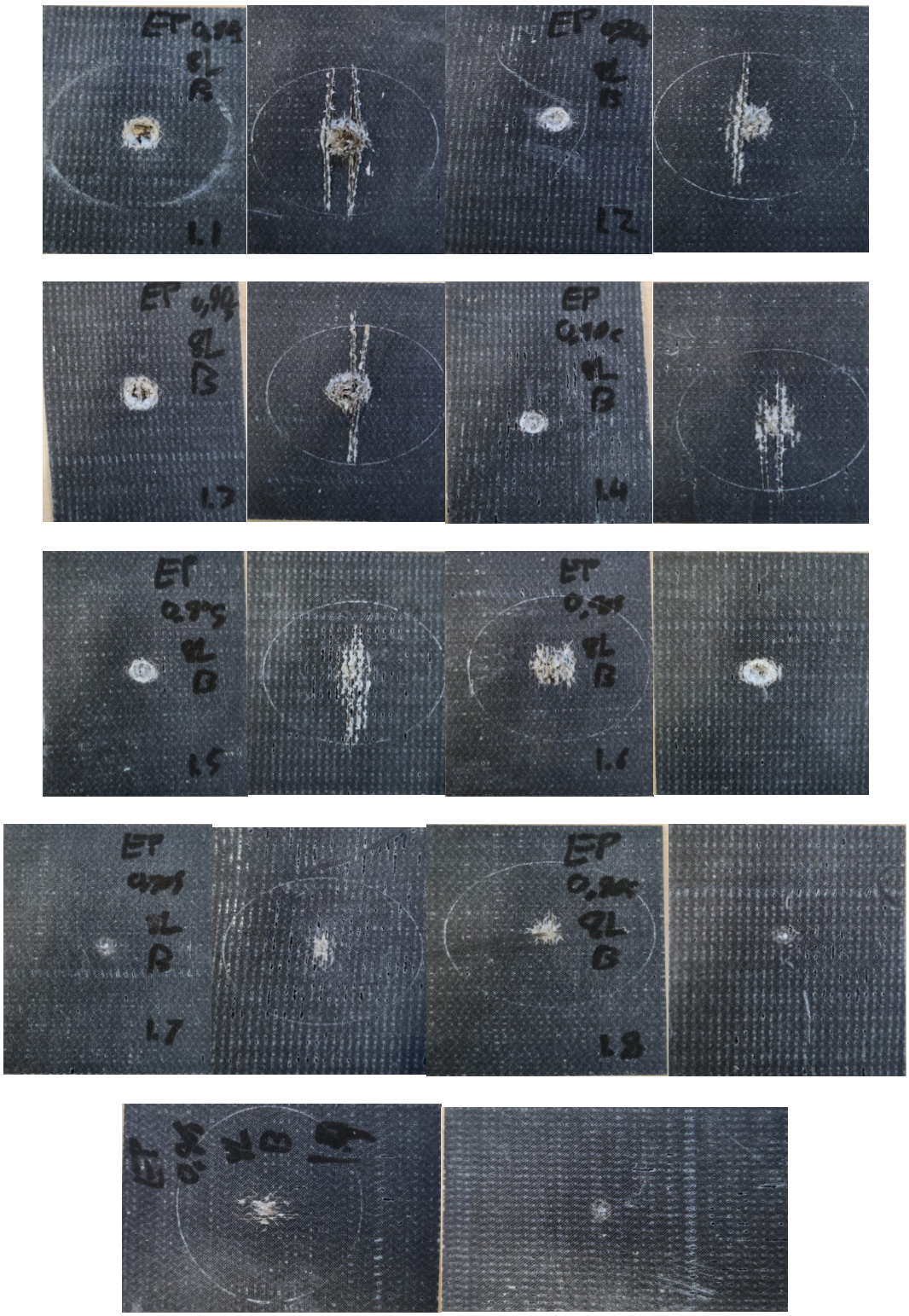

Figure 6-55: Post LVI view of basalt epoxy specimens (front and rear, respectively)

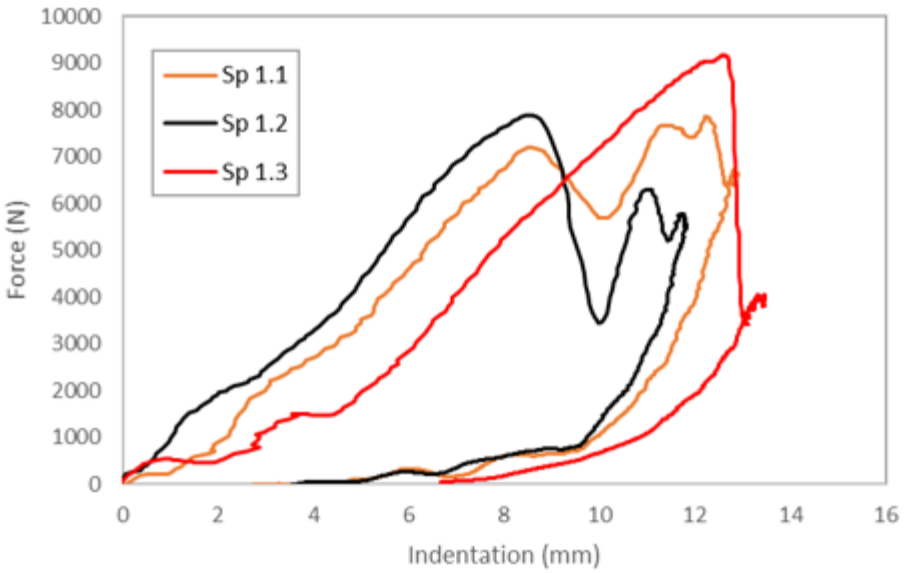

Figure 6-56: Plot of LVI impact force vs. indentation of basalt Elium with an impact energy of 55 J

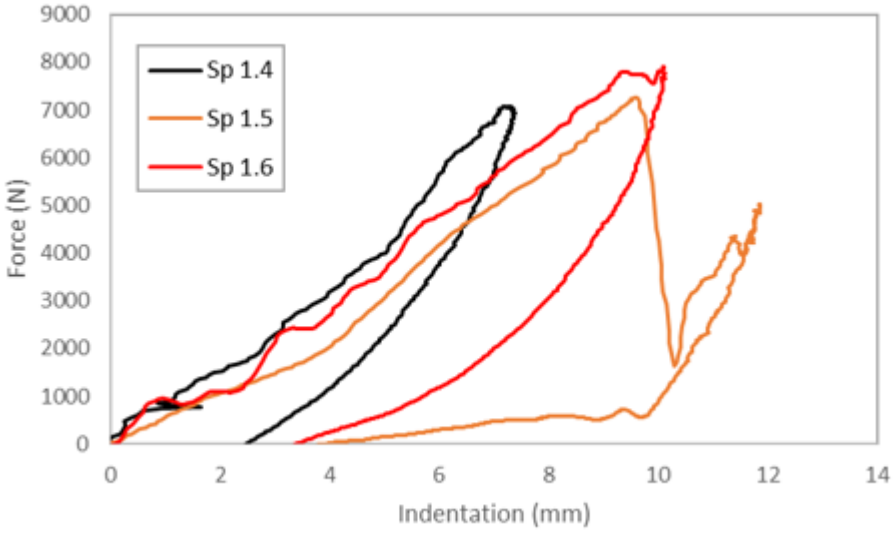

Figure 6-57: Plot of LVI impact force vs. indentation of basalt Elium with an impact energy of 40 J

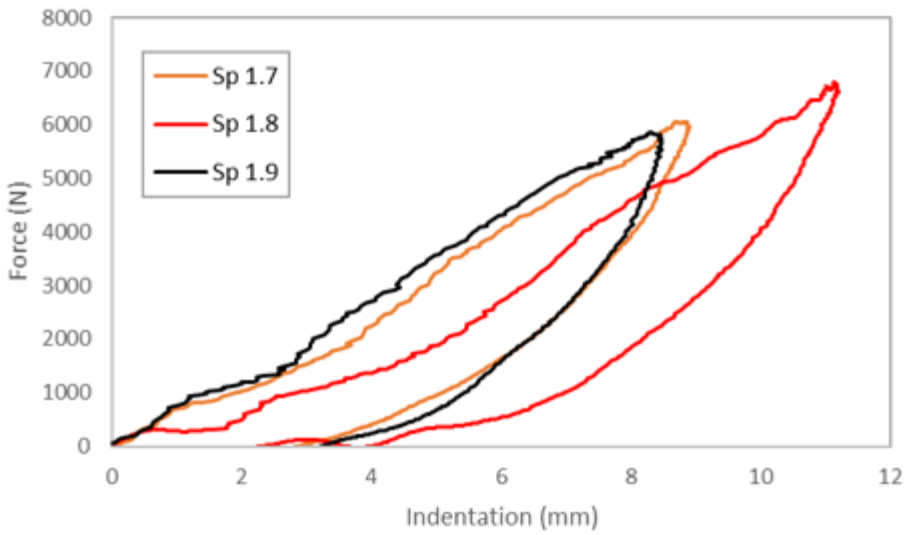

Figure 6-58: Plot of LVI impact force vs. indentation of basalt Elium with an impact energy of 25 J

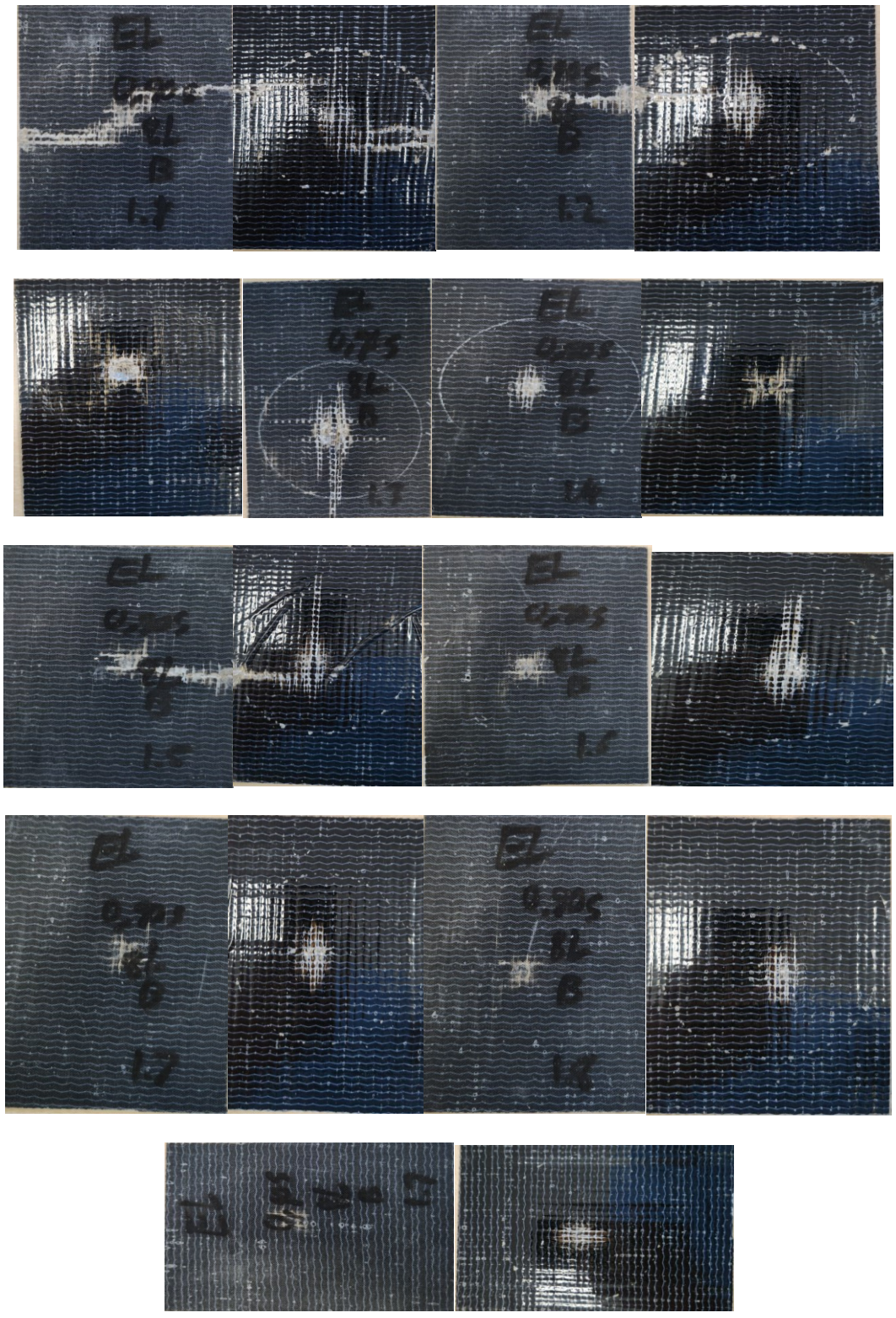

Figure 6-59: Post LVI view of basalt Elium specimens (front and rear, respectively)

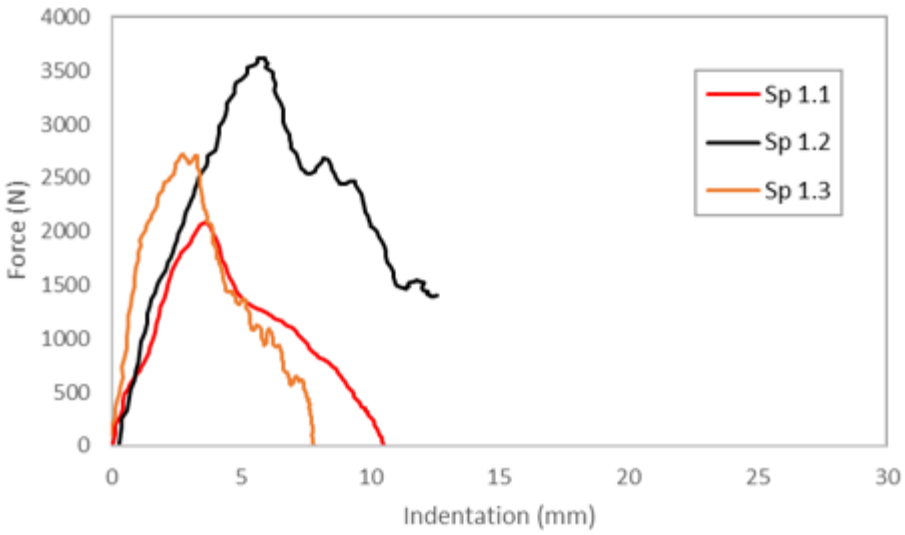

Figure 6-60: Plot of LVI impact force vs. indentation of Kevlar-29 epoxy with an impact energy of 55 J

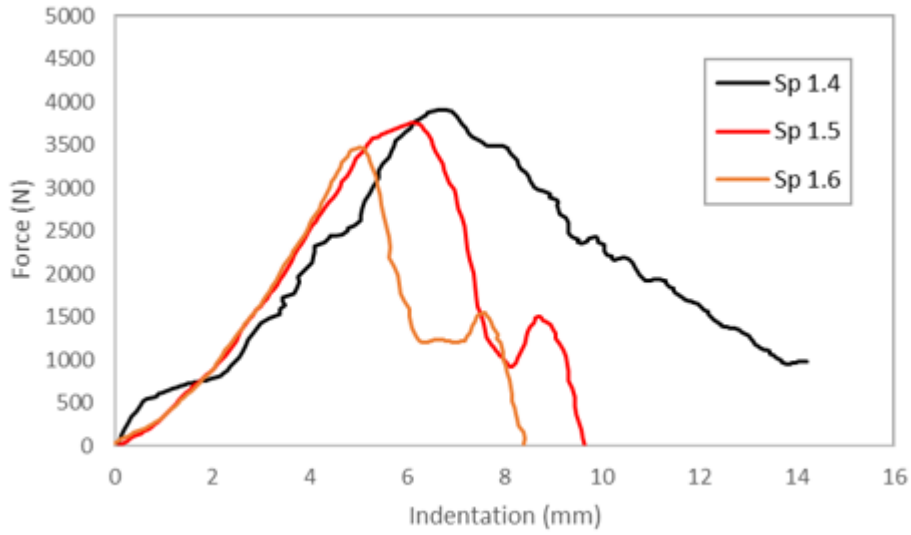

Figure 6-61: Plot of LVI impact force vs. indentation of Kevlar-29 epoxy with an impact energy of 40 J

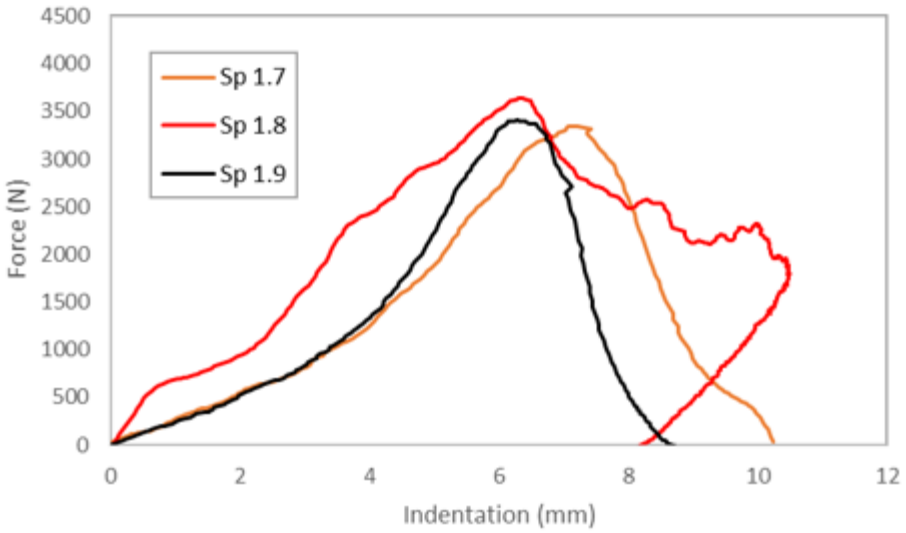

Figure 6-62: Plot of LVI impact force vs. indentation of Kevlar-29 epoxy with an impact energy of 25 J

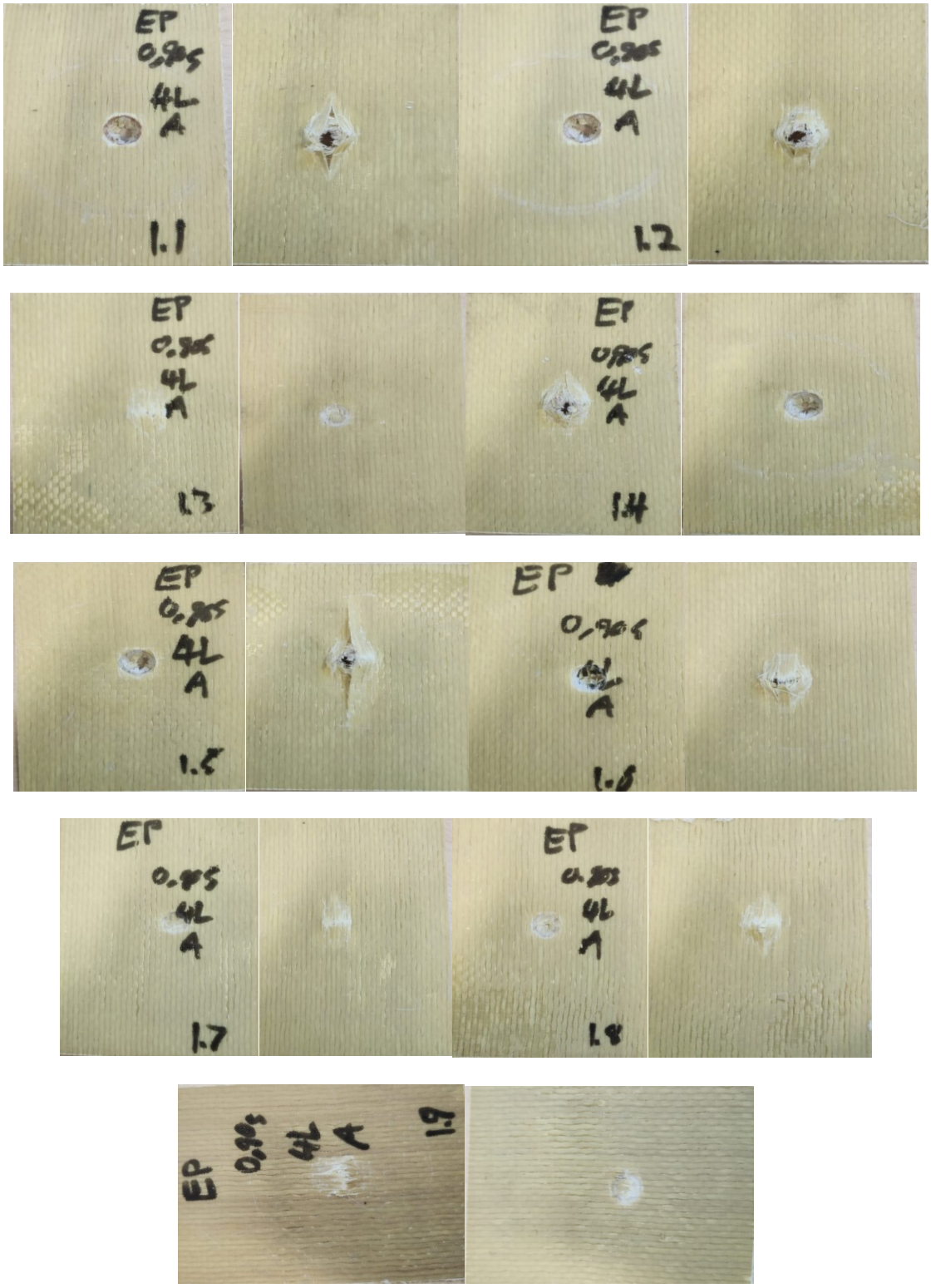

Figure 6-63: Post LVI view of Kevlar-29 epoxy specimens (front and rear, respectively)

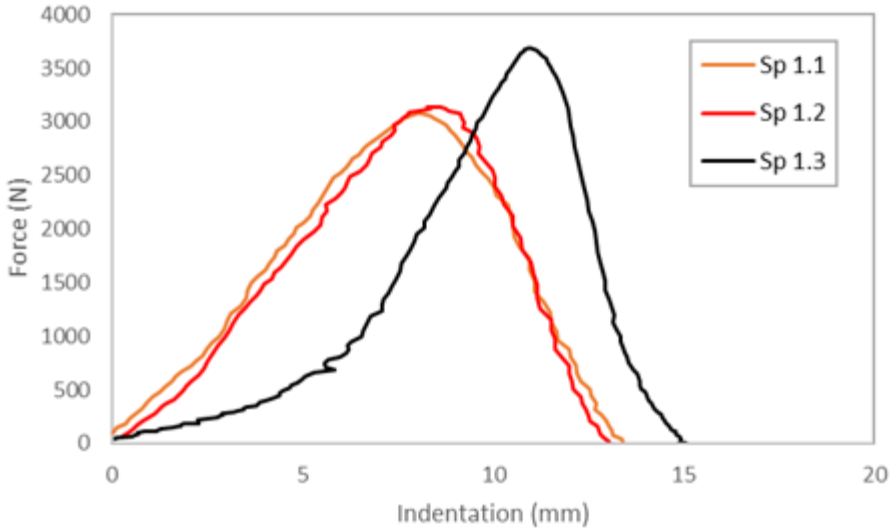

Figure 6-64: Plot of LVI impact force vs. indentation of Kevlar-29 Elium with an impact energy of 55 J

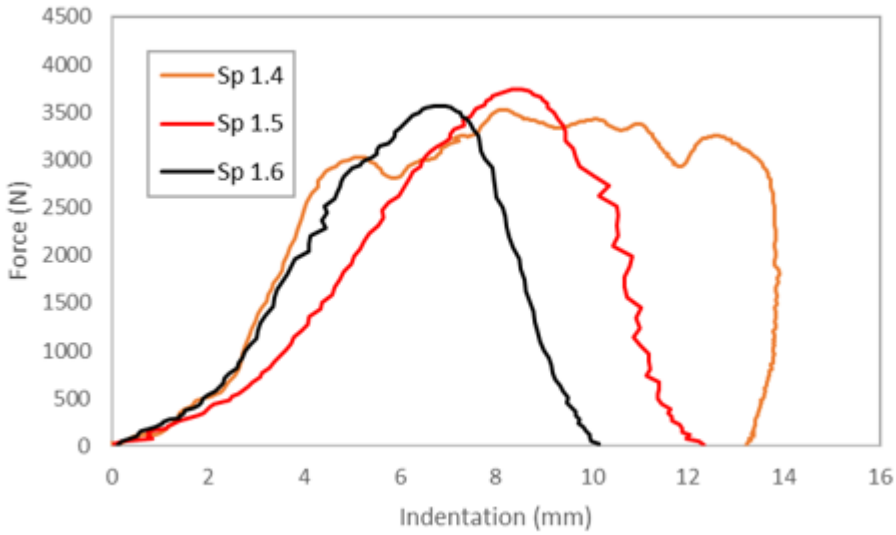

Figure 6-65: Plot of LVI impact force vs. indentation of Kevlar-29 Elium with an impact energy of 40 J

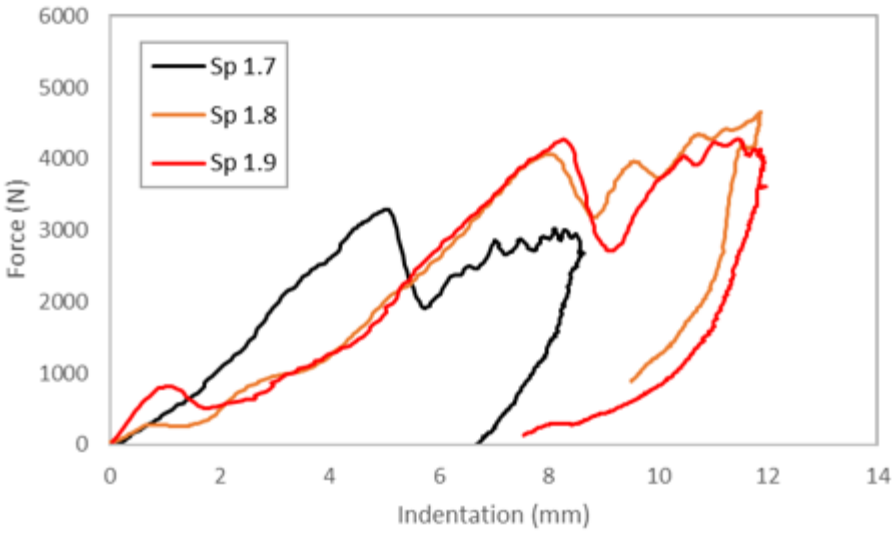

Figure 6-66: Plot of LVI impact force vs. indentation of Kevlar-29 Elium with an impact energy of 25 J

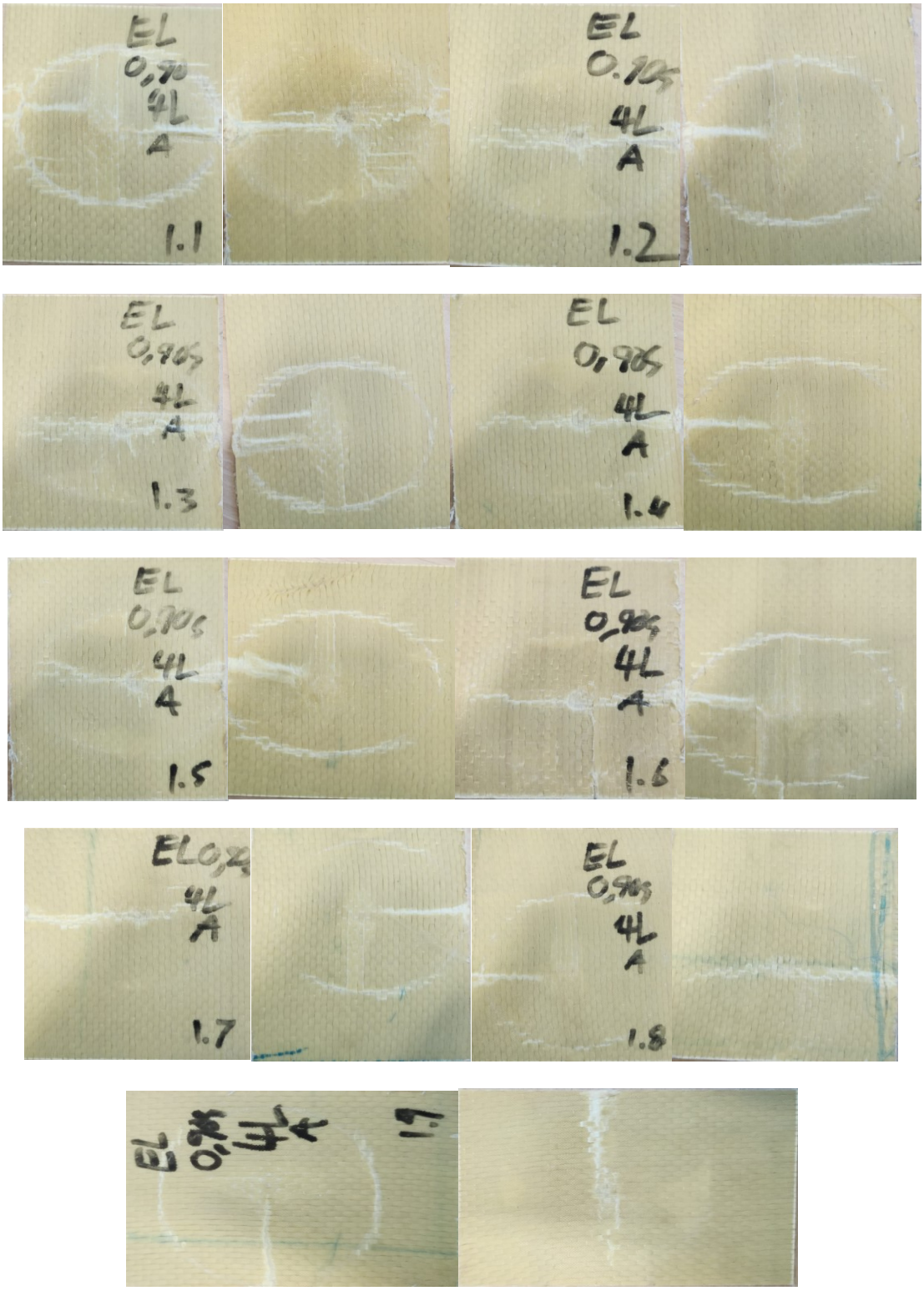

Figure 6-67: Post LVI view of Kevlar-29 Elium specimens (front and rear, respectively)

The 55 Joules low-velocity response of E-glass epoxy as seen in Figure 6-44 shows a spike in the force during the impact, which is short lasting (0.004 seconds). The short duration is due to the penetration experienced by the material. This failure is evident in the indentation depth trace as the indentation increases without a reverberation. As the impact Energy is decreased to 40 Joules then 25 Joules this force vs indentation trace, as seen in Figure 6-45 and Figure 6-46, respectively, shows that the sharpness of this curve is reduced to a more bell- shape. The indentation depth for both the 40 Joule and 25 Joule responses shows that a reverberation has taken place. This reverberation signifies that a penetration event has not taken place, rather, the material has progressively damaged locally, though insignificantly. Note that since both the symmetry and the indentation deviate, hence, the deformation of the material varies as a function of the applied impact energy.

The E-glass Elium 55-joule response seen in Figure 6-48, shows a similar response as the epoxy composite but with a more gradual force decrease after reaching the peak force. In Figure 6-48 specimen 1.2 experienced a complete penetration while specimens 1.1 and 1.3 had only partial penetration. This penetration event is evident in the trace of the indentation for specimen 1.2, in that there is no reverberation while the other two specimens exhibited a mild reverberation. The failure modes that dominate in the previously mentioned specimens are delamination and fiber tear-out. The results of these impact events seen in Table 6-13 show that Elium maintained a higher impact force before any deformation occurred when compared with the epoxy composites. This trend was observed for all energy levels. The basalt epoxy has a similar response to the E-glass epoxy. The sudden and abrupt nature of the impact event can be seen in Figure 6-52, signified by

the abrupt increase and decrease in force as the event progresses.

The indentation shows a partial penetration with a mild reverberation. The sharpness of the trace is reduced as it takes a more bell-shaped form with a decrease in impact energy as seen in Figure 6-53 and Figure 6-54. The visual effect of these events shown in Figure 6-55 shows that the major failure modes observed are similar to the E-glass with delamination and fiber tear-out being the most prominent modes. A different response can be observed when comparing these results with basalt Elium composites. Looking at Figure 6-56, Figure 6-57, and Figure 6-58, it can be observed that the characteristic sharp response in the curves is not projected. Even in the 55 Joule energy test, the response is a more gradually varying response compared to basalt epoxy. Additionally, the observed indentations trace shows that non-penetration impact events are transpired. Looking at the physical responses shown in Figure 6-59 reveals that no penetration took place, even at the 55 Joule impact energy. The observable major failure modes are local deformation and mild delamination. This deformation is characteristic of the plastic deformation of a ductile material.

The same pattern was observed for Elium composites, which resisted a higher impact force under all applied energies for basalt material combinations. Looking at the Kevlar-29 epoxy composite impact response in Figure 6-60, Figure 6-61, and Figure 6-62, one sees a more gradual response, with the highest force values being significantly lower than both the basalt and epoxy specimens. The indentation traces give insight into this observed effect. Every specimen, except for specimen 1.8, experienced penetration. This behaviour

is confirmed by Figure 6-63, which shows that partial penetration occurred (with the most dominant failure mode being fiber tear-out), even at the lowest energy levels.

Comparing this to the Kevlar-29 Elium specimens' responses seen in Figure 6-64, Figure 6-65, and Figure 6-66, it can be seen that the characteristic dome shape that represents a smooth transition in force during an event has taken place. The observed indentation traces indicate that for the higher energy levels of 55 and 40 Joules, the specimens were penetrated or had no reverberation. Looking at the physical responses in Figure 6-67 it can be seen that no penetration has occurred. The indentation trace shows that no reverberation has occurred, which in the case of E-glass and basalt Elium composites suggests penetration or significant surface damage to the material. The Kevlar-29 Elium composite had significant local nonlinear deformation that absorbed most of the impact energy without compromising the structural integrity of the fibers within the composite. This local nonlinear deformation explains why the indentation trace occurred the way it did, whereas mild reverberation is observed in the case when the composite was subjected to 25 Joule impact.

This non-penetration nonlinear deformation is what leads to the traces of force which shows the smooth nature of non-penetration while the indentation trace shows the non-reverberation trace. The results show that a smaller observable difference in the ultimate force can be seen between epoxy and Elium for Kevlar-29 composites with Elium having larger sustained values for both the 55 Joule and 25 Joule impact cases but a deviation from that trend is seen in the case of 40 Joules impacts.

Chapter 7: Conclusion and Recommendations

7.1. Summary

The main goal of this research was to characterize the mechanical performance of fiber-reinforced plastics with epoxy and Elium-based matrices, particularly focusing on their responses to low and HVIs. The motivation behind this study was to enhance the rather limited mechanical response database for Elium-based composites with various fiber reinforcements, especially in the case of basalt fiber. Basalt is an eco-friendly fiber that, when combined with Elium, a reformable and recyclable thermoplastic resin, offers a cost-effective and, more importantly, environmentally friendly composite material with outstanding mechanical properties suitable for structural applications. Composite specimens, composed of E-glass, basalt, and Kevlar-29 fibers, with both room-cured epoxy and Elium matrices, were fabricated according to ASTM D7136 standards [55].

For the HVI tests, several sabot-projectile systems were designed and optimized by testing different configurations to determine the most effective one. The in-house designed and built gas gun was subsequently calibrated using the selected sabot-projectile configuration. The static mechanical properties were assessed using an MTS servo-hydraulic universal testing machine with WATG and CLC testing fixtures. Next, using a modified Charpy impact testing setup, specimens of each composite were tested under LVI conditions and subjected to three impact energy levels (25, 40, and 55 joules). The HVI tests were conducted using a compressed air gas gun, following the methods established

by the US Army Research Laboratory [10]. Specimens of each material were evaluated to determine their ballistic limits.

7.2. Conclusion

The following conclusions are drawn based on the results obtained from the investigation:

- The sabot-projectile configuration was successfully optimized by selecting the configuration that provided the highest projectile kinetic energy. The gas gun was effectively calibrated for the selected configuration within pressure values ranging from 103.4 kPa to 827.4 kPa, and the gas gun's characteristic equation was determined.
- The densities of the specimens were measured, along with void contents and fiber weight percentages. This analysis revealed that the densities of the pure substances were consistent with the manufacturer-reported values. The void contents were all below 8%, with E-glass Elium having the highest void content at 7%. It was also observed that Elium-based composites generally had slightly higher void contents, except for the basalt specimens, where the void contents were comparable, with basalt Elium having a lower void content than basalt epoxy. When comparing the fiber weight percentages to the resin weight percentages, they were mostly in parity, except for Kevlar Elium, which had slightly higher values for fiber weight.
- The tensile properties obtained indicated that Elium composites outperformed epoxy composites, demonstrating higher ultimate tensile strengths and moduli due to proper fiber alignment, resulting in efficient fiber loading. Kevlar Elium, in particular,

exhibited values of 641.6 MPa for ultimate tensile strength and a modulus of 35.04 GPa.

- The shear properties obtained showed that both E-glass and basalt Elium-based composites exhibited higher values for both ultimate shear strength and modulus. E-glass Elium had the highest values for shear strength (69.8 MPa) and shear modulus (4.48 GPa). However, the trend of Elium outperforming epoxy specimens was not observed in the case of Kevlar samples, primarily because Kevlar has significantly smaller fiber filament sizes. In other words, since the weight of the resin is held constant for both the epoxy and Elium composite of a specific fiber type, then any area that has a higher concentration of resin would reduce the resin in other areas since mass is quasi-conserved. It is hypothesized that aramid filaments, due to their relatively smaller diameters, and the low viscosity of Elium cause more Elium to be absorbed within the tows, effectively reducing the resin content between the tows. As a result, pillars made of fiber tows with a higher concentration of Elium within the tows are created. The outcome would be a reduction in the in-plane shear strength but an increase in the compression strength of aramid Elium.
- Because of its low viscosity, compared to epoxy, Elium resin wets the fiber tows more thoroughly while the between fiber tow resin content is depleted. This resin absorption behaviour has a negative effect on the in-plane shear properties as resin surrounding the fibers governs the in-plane shear strength.
- The experimentally evaluated compressive properties indicate that the epoxy-based composites performed slightly better than the Elium-based composites, with the

exception of Kevlar-29. E-glass epoxy exhibited the highest values, with a compressive strength of 158.06 MPa and a modulus of 18.26 GPa. The reason for Elium performing lower than epoxy-based composites can be attributed to the more ductile nature of Elium, which increases the probability of fiber buckling and crimping. However, even with this effect, the differences were relatively small.

- Regarding low-velocity impact (LVI) performance, Elium-based composites outperformed epoxy-based composites significantly, with basalt Elium sustaining an average force of 8.83 kN at an impact energy of 55 J. Epoxy specimens exhibited more brittle failure modes with a higher degree of penetration during impact events compared to Elium-based composites. In contrast, Elium composites displayed more ductile failures with fewer penetration events, featuring observable failure modes characterized by nonlinear elastic-plastic deformation. Kevlar-29 Elium experienced no penetration but underwent significant impact surface deformation. Basalt Elium also had no penetration events, and their surface indentations were considerably smaller than those of Kevlar Elium.

- The results of the high-velocity impact (HVI) test demonstrated that Elium-based composites, irrespective of their fiber configuration, outperformed epoxy-based composites, with basalt Elium achieving the highest ballistic limit of 148 m/s. Similar failure modes could be observed between the low and HVI tests, with Elium-based specimens also exhibiting higher elastic-plastic deformation. In contrast, the epoxy

composites showed brittle failure modes, including highly localized deformation in the form of matrix cracking and projectile punch-through.

7.3. Recommendations for future work

The Novel Elium resin was introduced to the market as recently as 2014, resulting in a limited amount of research concerning Elium-based FRPs. The available database of information becomes even scarcer when specific fields, including high and LVI properties, are considered. Expanding this database can help realize the true potential of this recyclable and reformable matrix. These studies should encompass environmental factors as well as basic material properties. The following are a few recommendations that would benefit further investigations related to Elium and its high and low-velocity properties:

The impact behaviour of Elium-based composites at extreme temperature conditions is very limited or even non-existent. Given the increasing applications of composites in industries such as aviation, automotive, marine, and space, it's essential to understand how these materials perform in dynamic environments with extreme temperatures that can potentially degrade composite properties. Research into the temperature and moisture dependency of Elium resin under various static and dynamic loading conditions, especially under both low and HVIs, is strongly recommended.

In this research, a stacking sequence of [0,90]s was implemented. However, other fiber orientations and ply sequencing, such as various quasi-isotropic layups, should be investigated, particularly to target the interlaminar shear performance of such FRPs. The

effects of stacking sequence on the low and HVI characteristics of composites with an Elium-based matrix are sparsely studied, making further research in this area necessary.

After an impact event, the material properties of a composite are altered. Existing research on the material properties of Elium-based composites post-impact mainly focuses on LVIs. Therefore, it would be beneficial for industries like aerospace and high-speed trains to investigate the effects of HVIs on laminate material properties, including tensile, compression, shear, and bending. Implementing Elium composites could yield environmental and cost-saving benefits.

Elium, as part of the acrylic family of thermoplastics, may be susceptible to the effects of ultraviolet radiation. Little is known about the impact of ultraviolet aging and embrittlement on the material's capability to maintain its structural integrity. Therefore, research into the effects of ultraviolet aging and embrittlement of Elium-based composites subjected to both low and HVI is recommended and encouraged.

Lastly, Elium, like most thermoplastic matrices, exhibits toughness in response to fracture and fatigue. Therefore, the performance of FRPs made with Elium, especially basalt Elium, with its proven preliminary potential, should be systematically investigated.

Bibliography

[1] Friedrich, L. A., & Preston Jr, J. L. (1973). *Impact resistance of fiber composite blades used in aircraft turbine engines*. NASA report No. NASA-CR-134502, May 1973.

[2] Di Caprio, F., Cristillo, D., Saputo, S., Guida, M., & Riccio, A. (2019). Crashworthiness of wing leading edges under bird impact event. *Composite Structures*, *216*, 39-52.

[3] Fawcett, A. J., & Oakes, G. D. (2006, July). Boeing Transport Experience with Composite Damage Tolerance & Maintenance. In *FAA workshop for composite damage tolerance and maintenance. CHICAGO2006* (p. 32).

[4] Boria, S., Scattina, A., & Belingardi, G. (2017). Impact behavior of a fully thermoplastic composite. *Composite Structures*, *167*, 63-75.

[5] Khan, M. I., Umair, M., Hussain, R., Karahan, M., & Nawab, Y. (2023). Investigation of impact properties of para-aramid composites made with a thermoplastic-thermoset blend. *Journal of Thermoplastic Composite Materials*, *36*(2), 866-866.

[6] Yoshihara, K., Kamei, Y., Mizuno, A., Ohgaki, H., Hori, T., & Ueno, I. (2020). Effect of wettability on viscous fluid impregnation in single-layer woven-fibre bundles driven by pressure difference. *Composites Part A: Applied Science and Manufacturing*, *138*, 106049.

[7] Yoshihara, K., Kamei, Y., Mizuno, A., Ohgaki, H., Hori, T., & Ueno, I. (2020). Effect of wettability on viscous fluid impregnation in single-layer woven-fibre bundles driven by pressure difference. *Composites Part A: Applied Science and Manufacturing*, *138*, 106049.

[8] *WEST SYSTEM Epoxy* -105 system (n.d.). Www.westsystem.com. Retrieved September 4, 2023, from http://www.westsystem.com/products/105-system/

[9] Liquid Thermoplastic Resin for Glass-Reinforced Composite, cstjmateriauxcomposites.files.wordpress.com/2017/11/Elium_150_tech_data_sheet_grp_160908.pdf. Accessed 4 Sept. 2023.

[10] Ferriter, E. A., McCulloh, I. A., deRosset, W., & ARMY RESEARCH LAB ABERDEEN PROVING GROUND MD. (2005, January). Techniques Used to Estimate Limit Velocity in Ballistics Testing with Small Sample Size. In *Proceedings of the 13th Annual US Army Research Laboratory/United States Military Academy Technical Symposium, New York, United States* (pp. 72-95).

[11] Cantwell, W. J., & Morton, J. (1991). The impact resistance of composite materials—a review. *composites*, *22*(5), 347-362.

[12] Richardson, M. O. W., and M. J. Wisheart. "Review of low-velocity impact properties of composite materials." *Composites Part A: Applied Science and Manufacturing* 27.12 (1996): 1123-1131.

[13] Robinson, P., and G. A. O. Davies. "Impactor mass and specimen geometry effects in low velocity impact of laminated composites." *International journal of impact engineering* 12.2 (1992): 189-207.

[14] Liu, D. (1988). Impact-induced delamination—a view of bending stiffness mismatching. *Journal of composite materials*, *22*(7), 674-692.

[15] Dorey, G. (1986). Impact damage tolerance and assessment in advanced composite materials. In *Seminar on Advanced Composites*. UK Cranfield Institute of Technology.

[16] Joshi, S. P., and C. T. Sun. "Impact-induced fracture in a quasi-isotropic laminate." *Composites Technology and Research* 9.2 (1987): 40-46.

[17] Jih, C. J., and C. T. Sun. "Prediction of delamination in composite laminates subjected to low velocity impact." *Journal of composite materials* 27.7 (1993): 684-701.

[18] Cantwell, W. J., and J. Morton. "Geometrical effects in the low velocity impact response of CFRP." *Composite Structures* 12.1 (1989): 39-59.

[19] Sela, N., and O. Ishai. "Interlaminar fracture toughness and toughening of laminated composite materials: a review." *Composites* 20.5 (1989): 423-435.

[20] Safri, S. N. A., Sultan, M. T. H., Yidris, N., & Mustapha, F. (2014). Low velocity and high velocity impact test on composite materials–a review. *Int. j. eng. sci*, *3*(9), 50-60.

[21] Daniel, I. M., T. Liber, and R. H. LaBedz. "Wave propagation in transversely impacted composite laminates: An experimental investigation was conducted of wave-propagation characteristics, transient strains and residual properties of composite laminates under high-velocity impact." *Experimental Mechanics* 19 (1979): 9-16.

[22] Olsson, R. (2000). Mass criterion for wave controlled impact response of composite plates. *Composites Part A: Applied Science and Manufacturing*, *31*(8), 879-887.

[23] Olsson, R. (2003). Closed form prediction of peak load and delamination onset under small mass impact. *Composite Structures*, *59*(3), 341-349.

[24] Siva Kumar, K., and T. Balakrishna Bhat. "Response of composite laminates on impact of high velocity projectiles." *Key Engineering Materials* 141 (1997): 337-348.

[25] Backman, M. E., & Goldsmith, W. (1978). The mechanics of penetration of projectiles into targets. *International Journal of Engineering Science*, *16*(1), 1-99. [26]

[26] Moallemzadeh, A. R., S. A. R. Sabet, and H. Abedini. "Preloaded composite panels under high velocity impact." *International Journal of Impact Engineering* 114 (2018): 153-159.

[27] Reid, S. R., & Zhou, G. (Eds.). (2000). *Impact behaviour of fibre-reinforced composite materials and structures*. Elsevier.

[28] Mines, R. A. W., Roach, A. M., & Jones, N. (1999). High velocity perforation behaviour of polymer composite laminates. *International Journal of Impact Engineering*, *22*(6), 561-588.

[29] Kazemi, M. E., Shanmugam, L., Lu, D., Wang, X., Wang, B., & Yang, J. (2019). Mechanical properties and failure modes of hybrid fiber reinforced polymer composites with a novel liquid thermoplastic resin, Elium®. *Composites Part A: Applied Science and Manufacturing*, *125*, 105523.

[30] Raponi, O. D. A., Barbosa, L. C. M., de Souza, B. R., & Ancelotti Junior, A. C. (2018). Study of the influence of initiator content in the polymerization reaction of a thermoplastic liquid resin for advanced composite manufacturing. *Advances in Polymer Technology*, *37*(8), 3579-3587.

[31] Bhudolia, S. K., Gohel, G., Vasudevan, D., Leong, K. F., & Gerard, P. (2022). On the mode II fracture toughness, failure, and toughening mechanisms of wholly thermoplastic composites with ultra-lightweight thermoplastic fabrics and innovative Elium® resin. *Composites Part A: Applied Science and Manufacturing*, *161*, 107115.

[32 Barbosa, L. C. M., Bortoluzzi, D. B., & Ancelotti Jr, A. C. (2019). Analysis of fracture toughness in mode II and fractographic study of composites based on Elium® 150 thermoplastic matrix. *Composites Part B: Engineering*, *175*, 107082..

[33] Yaghoobi, H., & Taheri, F. (2021). Mechanical performance of a novel environmentally friendly basalt-elium® thermoplastic composite and its stainless steel-based fiber metal laminate. *Polymer Composites*, *42*(9), 4660-4672.

[34] Bhudolia, S. K., Joshi, S. C., Bert, A., Di, B. Y., Makam, R., & Gohel, G. (2019). Flexural characteristics of novel carbon methylmethacrylate. Composites. *Composites Communications*, *13*, 129-133.

[35] Allagui, S., El Mahi, A., Rebiere, J. L., Beyaoui, M., Bouguecha, A., & Haddar, M. (2021). Effect of recycling cycles on the mechanical and damping properties of flax fibre reinforced elium composite: experimental and numerical studies. *Journal of Renewable Materials*, *9*(4), 695.

[36 Sahki, A. (2022). *Development of thermoplastic composites reinforced with basalt and glass fabrics: Study of their Durability and Recyclability*. Doctoral dissertation, IMT-MINES ALES-IMT-Mines Alès Ecole Mines-Télécom, A lès, France.

[37] Bhudolia, S. K., Gohel, G., Fai, L. K., & Barsotti Jr, R. J. (2020). Fatigue response of ultrasonically welded carbon/Elium® thermoplastic composites. *Materials Letters*, *264*, 127362.

[38] Bhudolia, S. K., Perrotey, P., & Joshi, S. C. (2017). Enhanced vibration damping and dynamic mechanical characteristics of composites with novel pseudo-thermoset matrix system. *Composite Structures*, *179*, 502-513.

[39] Bhudolia, S. K., & Joshi, S. C. (2018). Low-velocity impact response of carbon fibre composites with novel liquid Methylmethacrylate thermoplastic matrix. *Composite Structures*, *203*, 696-708.

[40] Kazemi, M. E., Shanmugam, L., Li, Z., Ma, R., Yang, L., & Yang, J. (2020). Low-velocity impact behaviors of a fully thermoplastic composite laminate fabricated with an innovative acrylic resin. *Composite Structures*, *250*, 112604.

[41] Gohel, G., Bhudolia, S. K., Elisetty, S. B. S., Leong, K. F., & Gerard, P. (2021). Development and impact characterization of acrylic thermoplastic composite bicycle helmet shell with improved safety and performance. *Composites Part B: Engineering*, *221*, 109008.

[42] Bhudolia, S. K., Gohel, G., Kantipudi, J., Leong, K. F., & Gerard, P. (2021). Manufacturing and investigating the load, energy and failure attributes of thin ply carbon/elium® thermoplastic hollow composites under low-velocity impact. *Materials & Design*, *206*, 109814.

[43] Kazemi, M. E., Shanmugam, L., Dadashi, A., Shakouri, M., Lu, D., Du, Z., ... & Yang, J. (2021). Investigating the roles of fiber, resin, and stacking sequence on the low-velocity impact response of novel hybrid thermoplastic composites. *Composites Part B: Engineering*, *207*, 108554.

[44] Kinvi-Dossou, G., Boumbimba, R. M., Bonfoh, N., Garzon-Hernandez, S., Garcia-Gonzalez, D., Gerard, P., & Arias, A. (2019). Innovative acrylic thermoplastic composites versus conventional composites: Improving the impact performances. *Composite Structures*, *217*, 1-13.

[45] Gohel, G., Bhudolia, S. K., Leong, K. F., & Gerard, P. (2023). Understanding the impact properties and damage phenomenon of ultra-lightweight all-thermoplastic composite structures. *International Journal of Impact Engineering*, *172*, 104405.

[46] Libura, T., Rusinek, A., Rodrigue, M. B., Kowalewski, Z., & Gerard, P. (2022). Influence of fatigue aging and fiber orientation on the high velocity impact resistance of glass woven reinforced Elium acrylic laminates [*Review of Influence of fatigue aging and fiber orientation on the high velocity impact resistance of glass woven reinforced Elium acrylic laminates*]. In *Composites and Adhesives* (pp. 185–186). Institute of Fundamental Technological Research. https://www.ippt.pan.pl/repository/open/o8027.pdf

[47] Naslain, R., and F. Christin. "SiC-matrix composite materials for advanced jet engines." *MRS Bulletin* 28.9 (2003): 654-658.

[48] Hayat, M. D., Singh, H., He, Z., & Cao, P. (2019). Titanium metal matrix composites: An overview. *Composites Part A: Applied Science and Manufacturing*, *121*, 418-438.

[49] *Kevlar® Aramid Fiber Technical Guide - Dupont*, www.dupont.com/content/dam/dupont/amer/us/en/safety/public/documents/en/Kevlar_Technical_Guide_0319.pdf. Accessed 7 Sept. 2023.

[50] *E-glass & S-Glass Fabrics*. (n.d.). JPS Composite Materials. https://jpscm.com/products/e-glass-s-glass/

[51] "Basalt Continuous Fibers." *Basalt Continuous Fiber*, web.archive.org/web/20091103234348/www.albarrie.com/techfabrics/continuousfiber.aspx. Accessed 7 Sept. 2023.

[52] Standard, A. S. T. M. (2008). ASTM D3039-Standard test method for tensile properties of polymer matrix composite materials. *ASTM International: Philadelphia, PA, USA.*

[53] ASTM, D. (2008). 3410, Standard test method for compressive properties of polymer matrix composite materials with unsupported gage section by shear loading. *ASTM International: West Conshohocken, Philadelphia, PA, USA.*

[54] Standard, A. S. T. M. (2007). ASTM-D3518 Standard Test Method for In-Plane Shear Response of Polymer Matrix Composite Materials by Tensile Test of a 45 Laminate. *ASTM International: West Conshohocken, Philadelphia, PA, USA.*

[55] Standard, A. S. T. M. (2005). D7136: Standard test method for measuring the damage resistance of a fiber-reinforced polymer matrix composite to a drop-weight impact event. *ASTM International: West Conshohocken, Philadelphia, PA, USA.*

[56] Standard, A. S. T. M. (2016). D2734-16: Standard Test Methods for Void Content of Reinforced Plastics. *ASTM International, West Conshohocken: West Conshohocken, PA, USA*.

[57] Wang, K., & Taheri, F. (2023). Comparison of the Low-Velocity Impact Responses and Compressive Residual Strengths of GLARE and a 3DFML. *Polymers*, *15*(7), 1723.

[58] "Ballistic Precision Chronograph: Shooting Chronograph." *Caldwell*, www.caldwellshooting.com/range-gear/chronographs-and-wind-meters/ballistic-precision-chronograph/720001.html. Accessed 8 Sept. 2023.

[59] Londero Sports. "Competition Electronics Prochrono Ltd Ballistic Chronograph." *Londero Sports*, www.londerosports.com/bows/competition-electronics-prochrono-ltd-ballistic-chronograph. Accessed 11 Sept. 2023.

Appendix A : Summary of Test Data

Table A-1: Sabot # 1 test data

Rep #	Pressure (kPa)	Velocity (m/s)	Kinetic Energy Projectile (J)	Mass Sabot (g)	Mass Projectile (g)
1	689.48	152	36.97	5.3	3.2
2	689.48	159	40.45	5.3	3.2
3	689.48	152	36.97	5.3	3.2
4	689.48	162	40.68	5.3	3.1
5	689.48	157	38.21	5.3	3.1
Avg	689.48	156.4	38.65	5.3	3.16

Table A-2: Sabot # 2 test data

Rep #	Pressure (kPa)	Velocity (m/s)	Kinetic energy p (J)	Mass Sabot (g)	Mass Projectile (g)
1	689.48	175	50.53	3.8	3.3
2	689.48	179	48.06	3.9	3
3	689.48	180	46.98	3.8	2.9
4	689.48	176	51.11	3.9	3.3
5	689.48	176	51.11	3.9	3.3
Avg	689.48	177.2	49.56	3.86	3.16

Table A-3: Sabot # 3 test data

Rep #	Pressure (kPa)	Velocity (m/s)	Kinetic energy p (J)	Mass Sabot (g)	Mass Projectile (g)
1	689.48	177	56.39	3.7	3.6
2	689.48	178	55.45	3.7	3.5
3	689.48	182	53.00	3.8	3.2
4	689.48	176	57.31	3.6	3.7
5	689.48	179	56.07	3.8	3.5
Avg	689.48	178.4	55.64	3.72	3.5

Table A-4: Sabot # 4 test data

Rep #	Pressure (kPa)	Velocity (m/s)	Kinetic energy p (J)	Mass Sabot (g)	Mass Projectile (g)
1	689.48	187	57.70	2.6	3.3
2	689.48	186	58.81	2.6	3.4
3	689.48	185	53.05	2.5	3.1
4	689.48	186	57.08	2.4	3.3
5	689.48	185	59.89	2.6	3.5
Avg	689.48	185.8	57.31	2.54	3.32

Table A-5: Sabot # 5 test data

Rep #	Pressure (kPa)	Velocity (m/s)	Kinetic energy p (J)	Mass Sabot (g)	Mass Projectile (g)
1	689.48	184	52.48	2.6	3.1
2	689.48	182	54.66	2.6	3.3
3	689.48	186	58.81	2.6	3.4
4	689.48	187	55.95	2.7	3.2
5	689.48	182	53.00	2.6	3.2
Avg	689.48	184.2	54.99	2.62	3.24

Table A-6: Gas gun calibration data

Velocity (m/s) @ P=103.42kPa	Velocity (m/s) @ P=206.84kPa	Velocity (m/s) @ P=310.26kPa	Velocity (m/s) @ P=413.69kPa
85	123	148	165
85	122	148	163
85	123	148	161
85	124	149	165
85	123	149	163

Table A-7: Gas gun calibration data

Velocity (m/s) @ P= 517.11kPa	Velocity (m/s) @ P = 620.53kPa	Velocity (m/s) @ P=723.95kPa	Velocity (m/s) @ P=827.37kPa
178	183	188	189
177	180	190	187
177	185	190	189
177	183	187	188
177	179	190	190

Table A-8: Composite density data

Material	Volume 1 (ml)	Volume 2 (ml)	Mass (g)	Density (g/ml)
Aramid Epoxy	11.9	13.2	1.6	1.23
Aramid Epoxy	13.2	14.4	1.5	1.25
Aramid Epoxy	12.0	13.3	1.6	1.23
E-glass epoxy	13.2	14.6	2	1.43
E-glass epoxy	13.5	14.8	2	1.54
E-glass epoxy	13.9	15.3	2.1	1.50
Basalt epoxy	14.5	15.6	1.7	1.55
Basalt epoxy	13.6	15.3	2.8	1.65
Basalt epoxy	14.5	15.9	2.2	1.57
E-glass Elium	11.8	13.5	2.2	1.29
E-glass Elium	12.9	14.5	2.1	1.31
E-glass Elium	12.4	13.8	2	1.43
Aramid Elium	14.2	16.1	2.2	1.16
Aramid Elium	15.2	17.3	2.4	1.14
Aramid Elium	13.2	15.2	2.3	1.15
Basalt Elium	12.9	14.7	2.7	1.50
Basalt Elium	12.6	14.5	2.7	1.42
Basalt Elium	13.4	15.2	2.8	1.56

Table A-9: Burn-off test data

Material	Crucible Weight (g)	Specimen weight (g)	Total weight before (g)	Total weight after (g)
E-glass epoxy	355.3	1.8	357.3	356.3
E-glass epoxy	355.3	2.5	357.9	356.5
E-glass epoxy	355.3	1.3	356.6	356
E-glass Elium	355.3	8.3	363.6	359.6
E-glass Elium	355.3	1.8	357.1	356.3
E-glass Elium	355.3	1.9	357.2	356.2
Basalt epoxy	355.3	2.7	358	356.8
Basalt epoxy	355.3	2.7	358	356.7
Basalt epoxy	355.3	2.7	358	356.8
Basalt Elium	355.3	1.7	357	356.2
Basalt Elium	355.3	1.8	357.1	356.4
Basalt Elium	355.3	1.7	257	256.3
Aramid Epoxy	355.3	2.2	357.5	356.4
Aramid Epoxy	355.3	2.3	357.6	356.4
Aramid Epoxy	355.3	2.4	357.7	356.5
Aramid Elium	355.3	1.6	356.9	356.3
Aramid Elium	355.3	1.6	356.9	356.3
Aramid Elium	355.3	1.4	356.7	356.1

Table A-10: Fiber weight data

Material	Fiber weight (g)	resin weight (g)	Fiber weight%	Resin weight%
E-glass epoxy	0.80	1.00	44.4	55.6
E-glass epoxy	1.10	1.40	44.0	56.0
E-glass epoxy	0.70	0.60	53.8	46.2
E-glass Elium	4.30	4.00	51.8	48.2
E-glass Elium	1.00	0.80	55.6	44.4
E-glass Elium	0.90	1.00	47.4	52.6
Basalt epoxy	1.50	1.20	55.6	44.4
Basalt epoxy	1.40	1.30	51.9	48.1
Basalt epoxy	1.50	1.20	55.6	44.4
Basalt Elium	0.90	0.80	52.9	47.1
Basalt Elium	1.10	0.70	61.1	38.9
Basalt Elium	1.00	0.70	58.8	41.2
Aramid epoxy	1.10	1.10	50.0	50.0
Aramid epoxy	1.10	1.20	47.8	52.2
Aramid epoxy	1.20	1.20	50.0	50.0
Aramid Elium	1.00	0.60	62.5	37.5
Aramid Elium	1.00	0.60	62.5	37.5
Aramid Elium	0.80	0.60	57.1	42.9

Table A-11: Fiber volume data

Material	Volume Fiber (ml)	Volume Resin (ml)	total volume (ml)	Fiber volume fraction	Resin volume fraction
E-glass epoxy	0.33	0.85	1.23	0.27	0.69
E-glass epoxy	0.45	1.19	1.72	0.26	0.69
E-glass epoxy	0.29	0.51	0.83	0.34	0.61
E-glass Elium	1.76	3.96	6.16	0.29	0.64
E-glass Elium	0.41	0.79	1.29	0.32	0.61
E-glass Elium	0.37	0.99	1.46	0.25	0.68
Basalt epoxy	0.56	1.02	1.68	0.33	0.60
Basalt epoxy	0.52	1.10	1.73	0.30	0.64
Basalt epoxy	0.56	1.02	1.68	0.33	0.60
Basalt Elium	0.33	0.79	1.19	0.28	0.66
Basalt Elium	0.41	0.69	1.17	0.35	0.59
Basalt Elium	0.37	0.69	1.13	0.33	0.62
Aramid Epoxy	0.77	0.93	1.78	0.43	0.52
Aramid Epoxy	0.77	1.02	1.86	0.41	0.55
Aramid Epoxy	0.84	1.02	1.94	0.43	0.52
Aramid Elium	0.70	0.59	1.38	0.51	0.43
Aramid Elium	0.70	0.59	1.38	0.51	0.43
Aramid Elium	0.56	0.59	1.23	0.45	0.48